Wilkinson Microwave Anisotropy Probe (*WMAP*): Three–Year Explanatory Supplement[1]

The *WMAP* Science Working Group

March 16, 2006

[1]Version 2.0

Preface

This document is a concise description of the delivered data sets for the first 3 years of operation of the Wilkinson Microwave Anisotropy Probe (*WMAP*). It is intended as an overview of the delivered sky temperature and polarization maps and other data sets and as a description of the specific quantities contained in the *WMAP* time-ordered data. This document also describes the basic architecture and *modus operandi* of the instrument and spacecraft. Detailed descriptions of the spacecraft, instrument and data reduction methods have been described in publications that are referenced throughout this document and in particular at the beginning of Chapter 1.

This document is the cumulative effort of the following people: C. Barnes, R. Bean, C. L. Bennett, O. Doré, M. R. Greason, M. Halpern, R. S. Hill, G. Hinshaw, N. Jarosik, A. Kogut, E. Komatsu, D. Landsman, M. Limon, S. S. Meyer, M. R. Nolta, N. Odegard, L. Page, H. V. Peiris, D. N. Spergel, G. S. Tucker, L. Verde, J. L. Weiland, E. Wollack, E. L. Wright.

The high quality graphics in this document were created by: B. Griswold and S. Bensusen.

Last revised: March 16, 2006

This document is to be referenced as:
Wilkinson Microwave Anisotropy Probe (WMAP): Three–Year Explanatory Supplement,
editor M. Limon, et al (Greenbelt, MD: NASA/GSFC)

Available in electronic form at `http://lambda.gsfc.nasa.gov`

Previous version of this document was referred to as:
Wilkinson Microwave Anisotropy Probe (WMAP): Explanatory Supplement, editor M. Limon, et al (Greenbelt, MD: NASA/GSFC)

Contents

List of Figures

List of Tables

Chapter 1

Mission Explanatory Supplement

The *WMAP* (Wilkinson Microwave Anisotropy Probe) mission is designed to determine the geometry, content, and evolution of the universe via a 13 arcminute FWHM resolution full sky map of the temperature anisotropy of the cosmic microwave background radiation. The choice of orbit, sky-scanning strategy and instrument/spacecraft design were driven by the goals of uncorrelated pixel noise, minimal systematic errors, multifrequency observations, and accurate calibration. The skymap data products derived from the *WMAP* observations have 45 times the sensitivity and 33 time the angular resolution of the COBE DMR mission.

An overall description of the *WMAP* mission can be found in Bennett et al. [2003a]. Details of the instrument design are described in Jarosik et al. [2003b], Page et al. [2003b], and Barnes et al. [2002]. The basic results from the first year of WMAP observations are described in Bennett et al. [2003b]; the extended results from the first three years of operation are described in Jarosik et al. [2006], Hinshaw et al. [2006], Page et al. [2006] and Spergel et al. [2006].

   Jarosik et al. [2003a] describes the in flight performance of the *WMAP* radiometers. Characteristics of the telescope beam profiles and limits on systematic effects are provided in Page et al. [2003a] and Barnes et al. [2003]. A summary of non-cosmological signals observed is presented in Bennett et al. [2003c]. Hinshaw et al. [2003a] provides details on the data analysis pipeline and uses the results of the previous four papers.

   The methods for obtaining cosmological parameters are described in Verde et al. [2003]. Limits on non-Gaussian fluctuations are provided in Komatsu et al. [2003]. The angular power spectrum and basic cosmological parameters resulting from *WMAP* are presented in Hinshaw et al. [2003b] and Spergel et al. [2003]. The observed TE polarization signal is described in Kogut et al. [2003]. The implications of the above results for inflation is described in Peiris et al. [2003]. Finally a guide to understanding how cosmological parameters affect the the observed power spectra is provided in Page et al. [2003c].
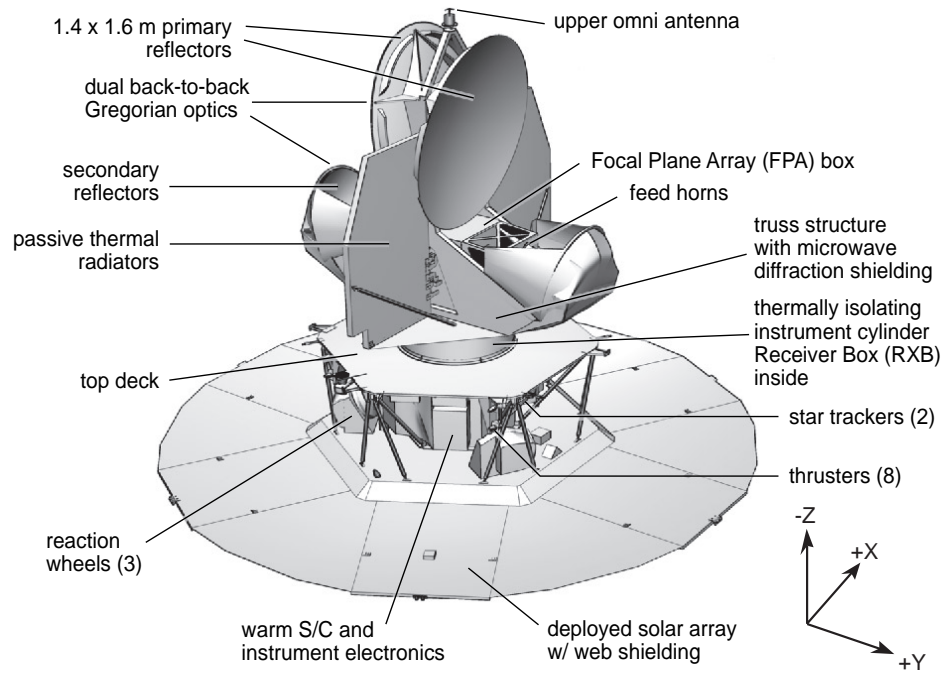
Figure 1.1: Spacecraft Overview. View of the spacecraft in the deployed configuration with major components labeled. The primary and secondary reflectors as well as the two thermal radiators are clearly visible in the upper portion of the image. The cold and warm section of the radiometers are housed in the FPA and RXB respectively and are locate in the core of the spacecraft under the primary reflectors. All the support electronics (AEU, DEU, PDU, MAC, LMAC), gyros, star-trackers, and reactions wheels are mounted on the hexagonal hub at the base of the spacecraft. While at L2, the optics, instrument and support electronics are constantly in the shade of the solar array and never exposed to solar radiation.

1.1 The Observatory

The design of the *WMAP* observatory[1], the choice of its orbit and its operational mode has been driven by the mission's science requirements of producing full sky maps of the cosmic microwave background radiation of unprecedented accuracy. Therefore the overall mission's design philosophy has been to minimize and control systematic errors even at the expense of sensitivity, simplicity and cost. This choice has a profound effect not only in the design of the instrument but on the spacecraft as well. In particular, to minimize temperature variations in the optics and the radiometers that could lead to systematic effects in the measured signals the thermal control is entirely passive. The heat generated by the instrument is radiatively dissipated by two large radiators mounted in the upper part of the spacecraft (see Figure 1.1) while all the support systems (battery, analog and digital electronics, etc.) are mounted around an open hexagonal hub in the lower part of the spacecraft and dissipate their excess heat through individual radiating surfaces which are part of their enclosures.

1.2 The Instrument

The *WMAP* instrument is basically made by two separate but highly interdependent components:

- **The Optics** focus the incoming radiation in the focal plane.

- **The Radiometers** amplify and convert the microwave signal into a measurable voltage.

In the following section we briefly describe the basic details of each of this components, we will also briefly describe the spacecraft's thermal design.

1.2.1 The Optics

The *WMAP* optical system consists of two back-to-back shaped offset Gregorian telescopes (see Figure 1.1). This is a highly symmetrical and compact optical design allows efficient placement of the feeds and radiometers while at the same time meeting all the science requirements. A summary of the optical system basic parameters is given in Table 1.1. The *WMAP*'s optical system design and characterization is described in detail in Page et al. [2003b].

Two mirror-symmetric arrays of corrugated feeds couple the radiation from *WMAP*'s two telescopes to the inputs of the differential receivers. Corrugated feeds were chosen because of their low emissivity, symmetric beam pattern, and low sidelobes. A summary of the feed basic parameters is given in Table 1.2. The *WMAP*'s feeds design, manufacturing methods, and characterizations are described in details in Barnes et al. [2003].

---

[1]The combination of the spacecraft and the instrument are referred to as the observatory throughout this document.

Band	K	Ka	Q	V	W	
Optical System			Gregorian			[-]
Primary Dimensions			1.4×1.6			[m]
Secondary Dimensions			0.8×0.8			[m]
Focal length			90			[cm]
Beam Size	0.88	0.66	0.51	0.35	0.22	deg
Max Edge Taper	-13	-20	-21	-21	-16/-20	[dB]
Forward Beam Efficiency	0.960	0.986	0.986	0.996	0.996/0.999	[-]

Table 1.1: *WMAP* Optical System Parameters. The beam patterns are not Gaussian, and thus are not simply specified. The size given here is the square-root of the beam solid angle. The value reported for the edge taper is the maximum for the center of the band. As the feeds are not illuminating the reflectors symmetrically, most of the edge has a substantially smaller taper. The beam efficiency is the integral of the beam in the area around 2° from the minimum divided by 4π; a value of 0.960 means that 4% of solid angle is scattered into the sidelobes.

Band	K	Ka	Q	V	W
Waveguide (WR)	42	28	22	15	10
ν(GHz)	19.5–25	28–37	35–46	53–69	82–106
ν_{gv}(GHz)	22	25.9	32.5	49.1	90.1
Length (mm)	536.4	542.1	567.6	569.6	603.3
Throat $\oslash$ (mm)	12.50	8.34	6.68	4.41	2.97
Aperture $\oslash$ (mm)	109.37	89.92	89.88	59.89	39.92
Mass (g)	1010	650	615	325	214
N_{gv}	116	169	217	329	533
N_s	1	1	3	4	5
θ_{fwhm} (deg)	10.1–7.7	8.9-6.7	7.8-6.0	8.8-7.4	9.7-8.3
Gain (dBi)	24.9–28.1	26.1–29.1	27.3–30.8	26.0–28.8	25.0–27.2

Table 1.2: *WMAP* Feed Specifications. The waveguide bands listed are for the rectangular commercial standard designations used in the radiometer, ν_{gv} is the hybrid frequency, N_{gv} is the total number of corrugations, and N_s is the number of sections (1 meaning made in one piece). The antenna beam width and the gain values range from the lower to the higher ends of the band.

1.2.2 The Radiometers

The 20 differential radiometers that make up the *WMAP* instrument cover 5 frequency bands and share the same design: they are pseudo-correlation differential radiometers with High Electron Mobility Transistor (HEMT) amplifiers passively cooled to ∼90 K. A summary of the *WMAP* radiometers design parameters and a schematic of an individual radiometer are given in Table 1.3 and Figure 1.2 respectively. The *WMAP* radiometers are described in detail in Jarosik et al. [2003b].

WMAP Band Designation	K	Ka	Q	V	W
Radiometers Specifications					
Frequency Range (GHz)	$20-25$	$28-36$	$35-46$	$53-69$	$82-106$
$\Delta\nu_{eff}$ (GHz)	4	5	8	13	19
Number of Radiometers	2	2	4	4	8
Sensitivity (mK sec$^{1/2}$)	0.65	0.78	0.92	1.13	1.48
T_{sys}(K)	29	39	59	92	145
HEMTs Specifications					
Noise temperature @300K (K)	∼100	∼115	∼150	∼260	∼370
Noise temperature @85K (K)	30±2	33±3	48±5	64±7	96±7
Gain @300K (dB)	33	32	31	31	32
Gain @85K (dB)	34	34	34	35	35
Gain flatness (dB)	±1.5	±1.0	±1.5	±2.5	±3.0

Table 1.3: *WMAP* Radiometer and HEMT Amplifiers Specifications. The sensitivity is per radiometer. Sensitivity and T_{sys} values are given in Rayleigh-Jeans temperature.
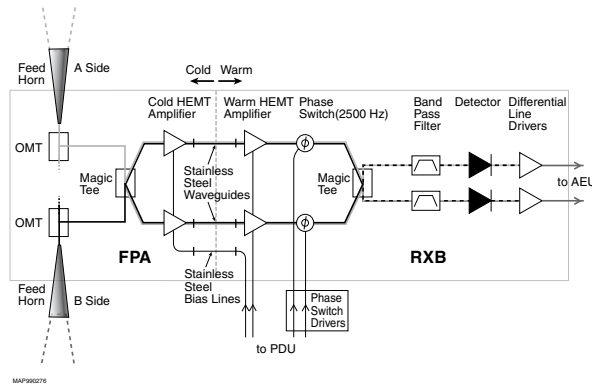
Figure 1.2: Layout of an Individual *WMAP* Radiometer. Components on the cold (left) side of the stainless steel waveguides are housed in the FPA where they passively cooled to ∼ 90 K through thermal links to the radiator panels. The components in the RXB achieve a balance temperature of ∼ 290 K.

1.2.3 The HEMT Amplifiers

The amplifier build for the WMAP satellite was carried out by the National Radio Astronomy Observatory Central Development Laboratory (NRAO/CDL) in Charlottesville, Virginia. See:

```
http://www.nrao.edu/engineering/amplifiers.shtml
```

Specific details of the amplifier design which were driven by the mission and the instruments flight environment can be found in Bennett et al. [2003a], Jarosik et al. [2003b]. Technical details regarding the design, development, and measured performance of this family of low noise 0.1 micron InP HEMT amplifiers can be found in: Nguyen et al. [1992], Pospieszalski [1989], Pospieszalski et al. [1993, 1995, 1997], Wollack [1995], Pospieszalski et al. [1994], Wollack and Pospieszalski [1998], Pospieszalski et al. [2000]

1.2.3.1 WMAP Amplifier Build, Qualification and Testing

Here, we briefly outline the manufacture, qualification, and test flow used to produce high reliability millimeter wave amplifiers in the quantities required for the flight instrument. The NASA Technical Workmanship and MIL standards were used in specification of the fabrication and in process inspection criteria. A summary of the development sequence and applicable references used for the mission are given in Table 1.4. The amplifier designs were qualified for thermal stress/shock, vibration, gain/bias stability, RF/ionizing radiation exposure, and extended life. Thermal and vibration test criteria for the final assemblies were derived from the General Environmental Verification Specification (GEVS). The phase, gain, noise, and stability as a function bias at the extremes of the flight environment were verified prior to and after amplifier level vibration and thermal cycling for each flight unit.

The NASA/GSFC provided quality assurance support for the component selection and the flight build. The use of commercial components with augmented testing was employed where suitable military grade product lines could not be identified. Each component type was procured as a single lot and subjected to additional testing during their manufacture to monitor their suitability for the intended end use. This arrangement enabled components with known performance heritage in existing NRAO cryogenic amplifier designs to be qualified and used if appropriate. Prior to onsite acceptance by NRAO, the components were visually inspected, samples were tested for bondability and electrical/mechanical tolerances were verified. Vendors willing to manufacture several key components required for the MIC (Microwave Integrated Circuit) amplifier design could not be identified. To meet these design needs, custom components were processed, delivered as wafers, and the final dicing steps were performed at NRAO. Samples of these parts were subsequently inspected by the NASA/GSFC materials branch prior to use. See Table 1.5 for a summary of the electrical components and vendors used for the amplifier build.

1.2.3.2 Ionizing Radiation Testing

An amplifier was radiation tested as an assembly at the levels anticipated over the mission [Bennett et al., 2003a] while under the nominal flight bias. A cobalt 60 source was used to produce total ionizing doses of 0, 2, 4, 8, 16, and 32 krad at incremental rates of 1.90, 1.90, 1.61, 2.04, and 6.50 krad/min, respectively. The anticipated total dose over the course of the *WMAP* mission is 2.3 krad-Si. The noise, gain, gain stability, and voltage/current bias points for each device in the amplifier were tested prior to and after exposure at a fixed temperature. Within the calibration errors, the amplifier response was unchanged. No measurable change in the amplifier electrical bias performance was observed over the course of the three week irradiation test duration. No change in amplifier noise temperature or gain was observed after exposure. (Comment: The unit was visually inspected before exposure and after the 32 krad-Si total dose. An essentially cosmetic darkening of the clear epoxy (GC Electronics, P/N 10-114) used to bond the LEDs to the exterior of the amplifier assembly cover was noted. The volume of this material used to stake wires internal to the amplifier body is effectively shielded by $\sim$ 5mm of brass was unaffected). The influence of ionizing radiation on the noise spectrum of the red LEDs used to illuminate the amplifier channel were also tested and found to be independent of the exposure.

1.2.3.3 Amplifier Life Testing

Life testing was preformed on an engineering model amplifier in parallel with the construction of the *WMAP* observatory. A double temperature regulated enclosure was instrumented to monitor the amplifier temperature and each stage of a precision power supply which generated the gate and drain voltage and currents. To minimize the influence of diurnal changes in the laboratory ambient temperature the entire fixture was mounted on a heat exchanger coil which circulated coolant regulated to $\sim$1K. The amplifier was mounted on the interior temperature stage which had a regulation error $\lesssim$ 20 mK. The computer, data acquisition, and HEMT bias boards were run off an uninterruptible power supply. Data taken the brief period of time where thermal regulation exceeds this window on the interior stage were flagged and removed during analysis. For the duration of the test, the input and output of the amplifier were terminated in waveguide loads and the LEDs were illuminated. Pre- and post-test noise, gain, and stability were consistent within the experimental calibration error limit (*i.e.*, $dT_n \simeq 3K, dG \simeq 0.08dB$). A summary of the bias data is presented in Figure 1.3.

The instrument housing keeping data for the first three years of the mission were scrutinized for potential aging effects in the 80 amplifiers used in flight. To carry out this analysis, the drain current monitor data for each channel was corrected for the change in the instrument temperature which experienced as the satellites distance from the sun changes. The pre-L2 flight data, which data contains amplifier burn-in response (*e.g.*, see Figure 1.3 and Jarosik et al. [2003b]) and initial instrument cool down response, was cut. The residuals to the resulting data set fit contain two terms which are largely degenerate: the secular increase in drain current arising from the degradation of the thermal control surfaces and the potential increase in device current due to device aging. To delve further we use the temperature

sensitivity for derived from the thermally driven orbital variations for each channel to remove an estimate of the influence of the secular increase in observatory temperature with time. We find that the response is consistent with the ground life test data and are unable to detect amplifier aging with the present data set. Based upon these observations and the inferred change in spacecrafts effective emissivity we estimate that > 10 years of instrument operation will elapse before aging of the active components will produce a measurable impact on the radiometer performance. At the time of the release of this document (2006), all amplifier channels are operating within nominal parameter ranges.

1.2.3.4 Safe Operating Bias and Power Levels

In a conventional room temperature high frequency amplifier the bias power is typically regulated from a higher level down to the desired safe operating point close to the devices. In operation this provides noise immunity and added protection unintentional external threats such as electrostatic and internal discharge. The thermal power dissipation associated with this approach on the cold stage can be unacceptably high in applications where the device is cooled to reduce the Johnson noise and increase gain. In such cryogenic applications the bias lines for the devices are passively filtered internal to the amplifier housing. In this configuration the harness, power supply, and amplifier must be considered from a system perspective to achieve the desired noise margin on the bias, stability, and protection from external threats. In addition, this places higher demands upon the required harness integrity and power supply sequencing required to safely operate the active devices without damage.

A fundamental tradeoff exists between breakdown voltage and speed for a given semiconductor material – roughly speaking – the carrier speed in a given material is a constant, to make faster transistor, the distance the electrons travel is minimized which ultimately reduces the breakdown voltage [Hadaway et al., 1995]. In the case of the *WMAP* 0.1 micron InP devices the maximum safe operating voltage to ~ 2 volts across the amplifier bias input terminals (*i.e.*, referenced to the device the drain-source voltage less than 1.5V is recommended [Nguyen et al., 1992]). The nominal instrument operating bias of $V_{ds} \sim 1.5$ volts and $-0.2 < V_{gs} < 0$ volts only leaves a modest margin against device stress due to bias transients. To deal with this issue the power distribution unit regulated outputs are limited by voltage clamps, the power on sequence does not allow an overshoot of the target bias, and the high frequency transients are filtered by a passive network at the amplifier housing. The immunity of this configuration against anticipated RF power, ESD, and IESD were verified against anticipated flight threat levels. From our laboratory testing of the engineering models we derived the following RF exposure limits for the amplifier inputs: 1) Green Limit: $< $ -5dBm (e.g., safe RF device exposure regime for power / voltage-stress), 2) Yellow Limit: $< $ 0dBm (e.g., onset of increased but recoverable gate leakage behavior due to the device burn-in), 3) Red Limit: $< $ 10dBm (maximum tested exposure CW limit at 300K, no permanent influence upon noise; temporary gate voltage shift). These operational limits were used throughout the missions I&T (Integration and Test) and Launch phases. The testing methods and comments found in Lilie [1989] and Chen [2000] may be of potential value in establishing such operational guidelines.
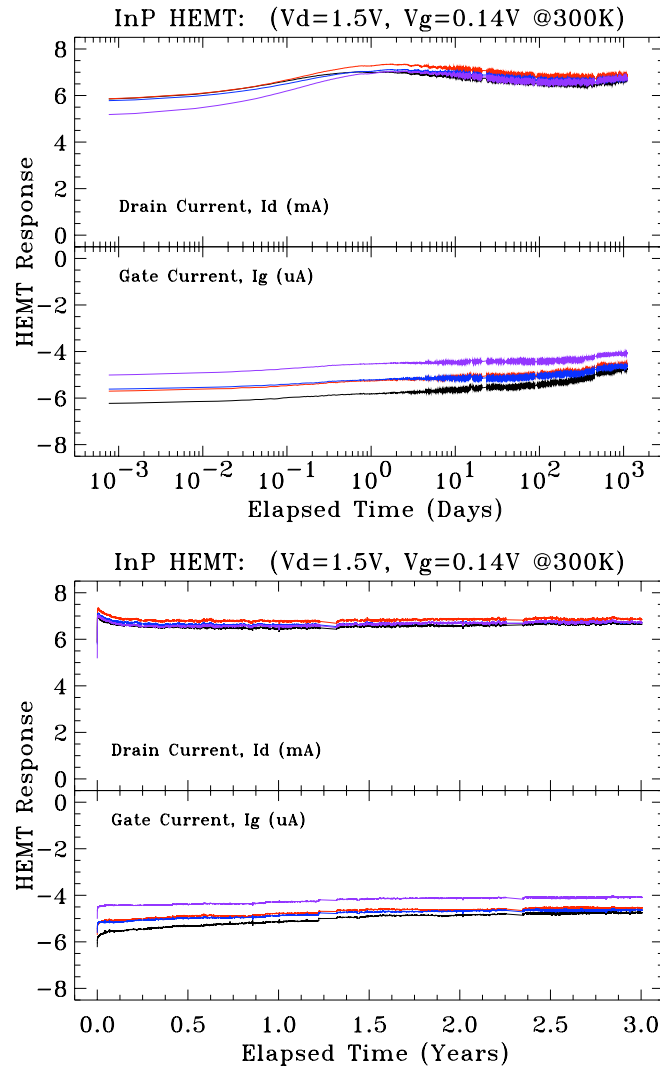
Figure 1.3: HEMT Life Test Bias Data (4-stage Q-Band Amplifier). The bias data from the amplifiers display an initial transient upon power on which repeatable and dependent upon the device thermal, illumination, RF power levels, and bias history. The timescale of this power-on or burn-in effect is device dependent and correlated with the gate leakage measured during initial screening of the wafer. A logarithmic axis is chosen in the top figure to emphasize this characteristic. In the bottom figure this influence is seen to die to a negligible level in several months. This characteristic behavior is typical of the observed response for the flight devices. From an instrument perspective this introduces a slow gain drift which is removed from the system during the calibration of the flight data.

Topic	Activity Description	Comments
Mil-Specification:	General Workmanship and Compatibility:	
	• Electroplating	(a), Bondable and Bright Gold
	• Wire Bonding	(b), Modify for RF Bond Strain Relief
	• Electrical Component Incoming Inspection	(b)
	• Wave-guide Flange Type and Configuration	(c), Modify Pinning Detail
	• Electrostatic Discharge & Charging (ESD/IESD)	(d-g)
	• Electromagnetic Interference (EMI/EMC)	(h,f)
NASA Technical Workmanship Standards:	General Workmanship: • Adhesive Bonds • Hand Soldering • Assembly Cleaning	NASA Handbooks (NHB)
NRAO/WMAP: Specific	Storage / Shipping / Humidity: Test Equipment Calibration: Material Selection / Qualification:	
	• Cryogenic Thermal Performance/Cycle/Shock	Amplifier Assembly
	• Out-Gassing	Selected Materials
	• Ionizing Radiation	(g-j) LEDs, Powered Amplifier
	• ESD / IESD	(d-g) Amplifier/Harness/Power Supply
	• Bias / Stability	Engineering Units/Flight Assembly
	• Life Test	Engineering Units
	• Complex Gain	Flight Units; Warm/Cryogenic
	• Gain Stability	Engineering Units; Warm/Cryogenic
	• Noise	Flight Units; Warm/Cryogenic
	• Vibration	(j) Flight Units; Un-Powered
	• Thermal Cycling	Flight Units / Coupons
	• Wire Bond Pull Strength	Process Coupons
	• Adhesive Cure	Process Coupons
	• Adhesive Peel Strength	Process Coupons
	• Ionic Contamination	Process Coupons
	Amplifier Fabrication / Test Sequence:	
	• Mechanical Tolerance	Inspection and Test per NRAO
	• Electrical Tolerance	Inspection and Test per NRAO
	• Plating Quality / Thickness	Inspection and Test per NRAO
	• Component (Wire) Bondibility	Inspection and Test per NRAO
	• Cleanliness / Ionic Contamination	Inspection and Test per NRAO
	NASA/GSFC In Process Inspection Point	
	• Acceptance Testing/Debug	RF Trend Data
	• Gain/Phase	300K / 80K Ambient Temperature
	• Noise	300K / 80K Ambient Temperature
	• Device Bias/Stability	300K / 80K Ambient Temperature
	• Vibration	(j) RF Trend Data before/after Test
	• Final Electrical Characterization	RF Trend Data
	NASA/GSFC Final Inspection Point	Pre-Cap Inspection / Data Review
	• Delivery for integration into receiver assemblies	RF Trend Data
	• Monitor and record amplifier bias and radiometer gain trend data throughout I&T	DC and Radiometer Trend Data

Table 1.4: WMAP Amplifier: Fabrication, Integration and Test Flow

a) MIL-G-45204C, Gold Plating, Electrodeposited.
b) MIL-STD-883E, Method 2010.10, Visual Inspection; Method 2011.7, Destructive Bond Strength; Method 2023.5, Non- Destructive Bond Pull.
c) MIL-F-3922, Waveguide Flange Specification.
d) MIL-STD-462, Transient EMC (pulse is $\sim$ 10ms wide while an ESD pulse is on the order of 10-to-100ns).
e) MIL-STD-1541A, Transient ESD Source.
f) MIL-STD-883, Method 3015, V-Zap ESD Test.
g) NASA Technical Handbook, "Avoiding Problems Caused by Spacecraft on-Orbit Internal Charging Effects", NASA-HDBK-4002, February 17, 1999.
h) NASA Technical Standards for Space Flight and Mission Critical Ground Support Hardware, see http://www.hq.nasa,gov/office/codeq/qdoc.pdf
i) J.L., Barth, et al., "MAP Radiation Analysis," X-900-97-006, August, 1997, Table 7.
j) J.S. Milne, General Environmental Verification Specification for STS and EVL Payloads, Subsystems, and Components, 1996, NASA GSFC, System Reliability & Safety Office, Greenbelt, Maryland.

Component Envelope X×Y×Z (inches)	Part Designation	Part Vendor
Solder-to-Wire Bond Transition 0.110 × 0.040 × 0.010	Au/Cu/Cr on Alumina (NRAO Custom Design)	American Technical Ceramics, Corporation, Thin Films Products, Jacksonville, FL 32216.
Capacitor, 680 pF 0.055 × 0.055 × 0.055	CDR11BP681AJNS (700A681JCA50X)	American Technical Ceramics, Corporation, Huntington, Station, NY 11746-2102.
Resistor Divider Network 0.034 × 0.034 × 0.010	MSMT125ST-55000J-GB	Mini-Systems, Inc, Thin Films Division, Attleboro, MA 02703-0028
Resistor, 10 ohm 0.016 × 0.020 × 0.010	MSMW122AT10R00J-GB	Mini-Systems, Inc, Thin Films Division, Attleboro, MA 02703-0028
Resistor, 10 ohm 0.013 × 0.032 × 0.013	H0302AP100JG (Alternate Component)	State of the Art, Inc., State College, PA 16803-1797.
Capacitor, 16 pF 0.055 × 0.055 × 0.055	CDR11BP160AJNS (700A160JCA150X)	American Technical Ceramics, Corporation, Huntington, Station, NY 11746-2102.
Resistor, 50 ohm 0.016 × 0.020 × 0.010	MSMW122AT50R00J-GB	Mini-Systems, Inc, Thin Films Division, Attleboro, MA 02703-0028.
Resistor, 50 ohms 0.013 × 0.032 × 0.013	H0302AP500JG (Alternate Component)	State of the Art, Inc., State College, PA 16803-1797.
Termination Resistor, 50 ohm 0.007 × 0.033 × 0.005	Quartz, NiCr 25 ohm/sq. (NRAO Custom Design)	Filtran Microcircuits, Inc., Ottawa, Ontario, K1H8P5.
RF Stabilization Network 0.008 × 0.0125 × 0.005	Quartz, NiCr 25 ohm/sq. (NRAO Custom Design)	Filtran Microcircuits, Inc., Ottawa, Ontario, K1H8P5.
Capacitor, 0.8 pF 0.025 × 0.025 × 0.008	D25CG0R8B1PC	Dielectric Labs, Cazenovia, NY 13035.
Capacitor, 0.2 pF 0.015 × 0.015 × 0.006	D15CF0R2P5PC	Dielectric Labs, Cazenovia, NY 13035.
Cuflon Substrate XXX × 0.028 × 0.003	CF-A-3-5-6-G3 (NRAO Custom Design)	Crane/Polyflon, New Rochelle, NY 10801.
InP HEMT, 0.1 μm Gate 0.010 × 0.013 × 0.004	Wafer Number I448A/S514-026	Hughes Research Laboratory, Malibu, CA 90625.
Coupling Capacitor XXX × 0.0065 × 0.003	Metalized Quartz (NRAO Custom Design)	NRAO Central Development Laboratory, Charlottesville, VA 22903.
Red LED	521-9186 (RL-50/MV-50)	Dialight Corporation, Corporation, Manasquan, NJ 08736.
Bias Connector, Micro-D	M83513/01-BN	ITT/Cannon, Santa Ana, CA 92705-6500.
LED Connectors	GM2, -Round (Male) GF2, -Round (Female)	Microtech, Boothwyn, PA 19061-2199.

Table 1.5: *WMAP* Amplifier Components Summary.

1.3 The Journey

This section summarizes the events and the environment encountered by the observatory from days immediately preceding launch to the moment of the lunar swing-by that provides the gravity assist to reach its final orbital position around L2.

1.3.1 Time Line

The *WMAP* observatory was powered on and tested for the last time at GSFC on April 6, 2001 before being shipped to Kennedy Space Center (KSC) on April 18 where it arrived two

days later. In the approximately two months following its arrival at KSC, the observatory underwent further testing, integration with the launch vehicle 3rd stage and finally integration with the rest of the launch vehicle. The launch vehicle was a Boeing Delta II 7425. This was the 286th Delta launch. A summary of these events are included in the log in Appendix B which also covers the rest of the mission to the end of the first year of science observations.

1.3.2 Launch

On June 30, 2001 at 19:29 GMT the GSFC control team gave its approval to proceed with the terminal count-down. Approximately 10 minutes later the observatory was switched to internal power and at 19:46:46 GMT it lifted off from launch pad 17B at the Eastern Range Space Launch Complex – the first step in a journey that took it three times around the Earth (phasing loops) and close to the Moon (fly-by) before it reached its intended observational position around L2.

Five minutes after launch, the Delta II first-stage engine cut off and the fairing jettisoned, exposing the observatory for the first time to the full space environment. Although the launch vehicle was tracked by radar station and its telemetry was received by the Boeing launch team, there was no contact with the observatory itself during launch and ascent. At approximately 21:00 GMT the signal from of *WMAP*'s omni-directional was picked up by NASA's TDRS-W satellite and relayed to the ground, confirming that the payload was in good health and that all parameters were nominal. The *WMAP* payload was successfully inserted in a ~ 185 km elliptical parking orbit with a $\sim 28.7°$ inclination.

1.3.3 Deployment and Instrument Power On

From the moment the observatory was switched to internal power, 5 minutes before launch, until deployment of the solar array panels, the observatory relies on power provided by the battery. At 21:03 GMT an on-board procedure triggered the deployment of the solar array. Immediately after this event the spacecraft oriented itself along the Sun-line maximizing the electrical power being generated by the array and, at the same time, protecting the instrument from the solar radiation.

At 21:43 GMT the *WMAP* instrument was powered in flight for the first time: housekeeping data was monitored as the instrument cooled and the flight burn-in phase was completed as scheduled. All science signals were within nominal limits during the cool down period. HEMT drain currents and RF radiometer total power were similar to the modeled response based upon the thermal environment and the radiometric flux presented to the instrument. The RXB temperature peaked at ~ 293 K before cooling as anticipated due to the instrument power on time, thermal loads, and cooling profile. No anomalies were noted in the instrument electronics system (AEU/DEU and PDU) performance.

A platinum resistance thermometer (PRT) on top of the thermal reflector system radiator (DTAMXTOPRADT) failed on 2001:185:1100 GMT. From the flight telemetry we conclude that the sensor failed open and remains in this state. This failure was not completely unexpected, a similar sensor at the same location had failed during ground testing. Two days
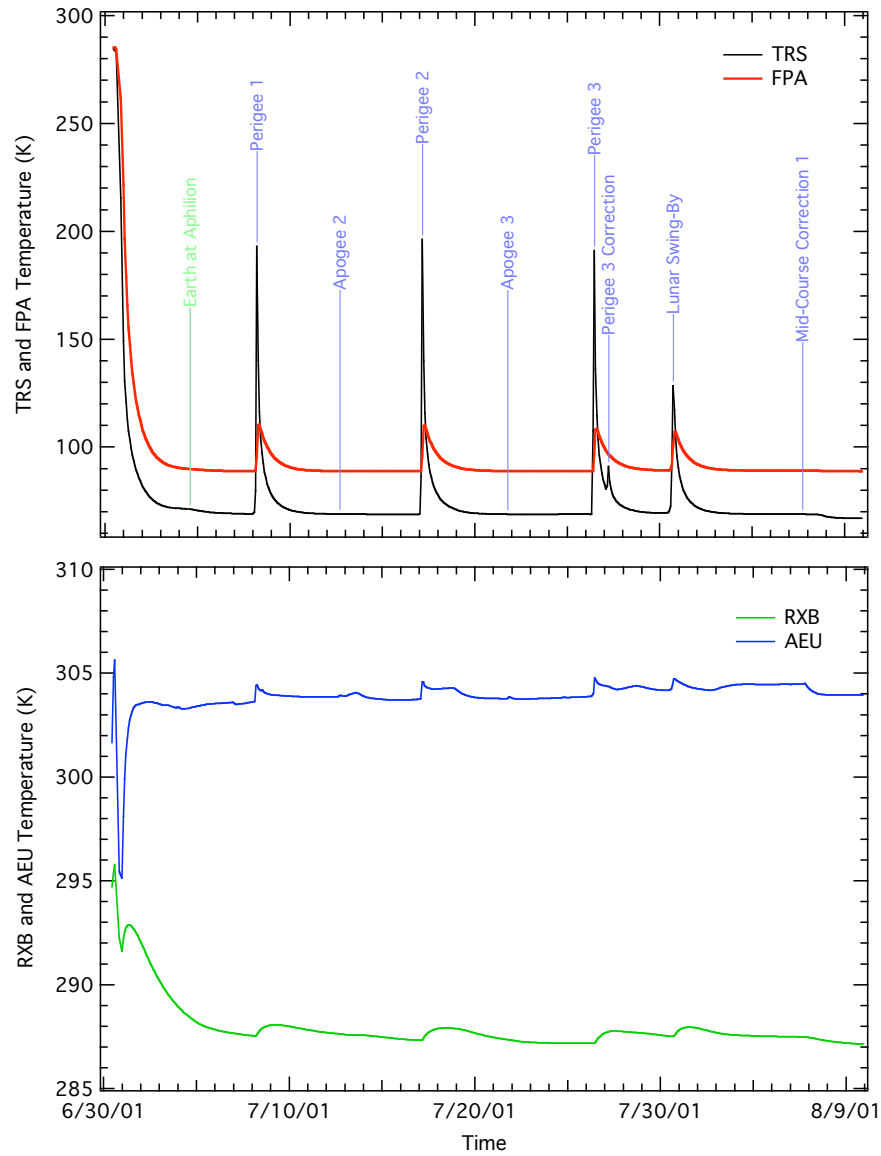
Figure 1.4: Cool-down Thermal Profile. Thermal profile of major instrument subsystems (TRS, FPA, RXB and AEU) from the launch to the beginning of the observations used for the first year maps.

after deployment on July 2, 2001 at 19:18 GMT the spacecraft entered observing mode for the first time.

1.3.4 Observatory Checkout

From June 30, 2001, when *WMAP* was launched, to August 17, 2001 the *WMAP* spacecraft and instrument underwent a period of formal checkout. During this period the spacecraft was contacted through the DSN multiple times each day and all subsystem were tested thoroughly. The end of the in-flight checkout marked the beginning of normal mission operations; during this time the spacecraft is constantly in observing mode with one DSN contact per day. The spacecraft exits observing mode only for the planned station keeping maneuvers (see section 1.3.10) or if an unexpected event (see Table 1.9) puts it in "Safehold". Details of the spacecraft in-flight checkout are presented in Jackson [2002].

1.3.5 Phasing Loops

Three orbital phasing loops and a lunar gravity assist were employed to perform the transfer to the mission's operational orbit – a Lissajous orbit about the Sun-Earth L2 Lagrange point, ~ 1.5 million km from Earth in the anti-Sun direction. To fine tune the spacecraft trajectory in preparation for the Lunar Fly-by, 7 burns were performed while at Earth's perigee (4) and apogee (3).

Thruster calibration maneuvers were performed at apogees. This allowed calibration of the propulsion system using the thruster configurations for the phasing loop and station keeping burns.

A summary of the phasing loops maneuvers as well as all the other maneuvers performed during the first year of the *WMAP* observatory's operations are given in Table 1.6. The first perigee burn (P1) was the first of a series of incremental adjustments of the satellite's orbital energy and phasing for the final lunar assist. The second perigee burn (P2) provided a slight correction in preparations for the critical final perigee burns. The velocity boost provided by the final perigee (P3) and final correction (P3c) burns tuned the orbit for a lunar encounter at the desired time and location to achieve the desired eclipse free trajectory (i.e. an orbit that does not cross Earth-shadow's cone). The temperatures of the primary reflectors exhibited significant transients during the perigee passes (see Figure 1.4) as they were exposed to both Earth IR inputs and edge-on solar inputs to the upper portion of their +X sides. This was an anticipated aspect of the mission design.

The phasing loops were also used to measure the far side-lobe response of the *WMAP* optical system. See Barnes et al. [2003] for details. In particular during the first orbital phasing loop (July 2-8, 2001), while the Moon was close enough to be a significantly bright thermal source, the spacecraft was operated in a scanning pattern very similar to the flight observing mode with the Moon sweeping through the optical system far side-lobes.

1.3.6 Earth IR and Outgassing

The materials and processes used in the construction of the *WMAP* Observatory result in a small mass loss due to outgassing. Outgassing from and re-deposition of materials on space-craft surfaces are anticipated in flight due to the loss of volatile materials and the pre-flight exposure to the ambient environment. Outgassing products emitted and re-encountered by spacecraft have a finite capture probability which increases upon cooling. Pre-flight contamination estimates did not indicate a concern for critical passively-cooled elements and optical sensors. In-flight performance of these subsystems are consistent with these estimates. In flight, outgassing by-products resulted in a small but detectable perturbation on the system's total angular momentum during perigee maneuvers [Starin et al., 2002]. This observation may be of potential interest to the mission design of spacecraft with large cold surfaces.

Prior to each perigee maneuver, *WMAP* was in its nominal science observing mode. The first command to prepare for a burn maneuver placed the system into Inertial Mode. Once in this configuration for the perigee pass, the spacecraft and its solar array panels were oriented approximately 45-to-50 degrees from the Sun-line and the instrument was directed toward the nadir. This placed the thrusters in the proper orientation for the burn. These conditions also result in an attitude profile which allows the Sun to briefly heat portions of the instrument and the Earth albedo to illuminate the anti-solar side of the array before perigee. At the first perigee, a torque of 0.004 Nm and a peak system momentum of 2 Nms were noted before the ASC returned to nominal state. (Note: The maximum allowed wheel torque and

Event	yyyy:ddd:hhmm GMT	ΔV (m/s)	Burn (s)	Altitude (km)
Apogee 1	2001:185:1322	1.921	106	299,478 (E)
Perigee 1	2001:189:0433	20.194	1274	3,098 (E)
Apogee 2 (+Z Cal)	2001:193:1611	0.254	41	347,891 (E)
Perigee 2	2001:198:0336	2.514	177	2,955 (E)
Apogee 3 (-Z Cal)	2001:202:1854	0.296	40	356,012 (E)
Perigee 3	2001:207:1029	7.410	546	4,741 (E)
Perigee 3 Correction	2001:208:0430	0.308	24	158,306 (E)
Lunar Swing-By	2001:211:1637	N/A	N/A	5,279 (M)
Mid-Course Correction 1	2001:218:1637	0.103	18	755,736 (E)
Mid-Course Correction 2	2001:257:1551	0.042	6	1,402,107 (E)
Station Keeping 1	2002:016:1650	0.428	72	(L2)
Station Keeping 2	2002:128:1603	0.348	49	(L2)
Station Keeping 3	2002:211:1638	0.460	66	(L2)
Station Keeping 4	2002:309:1921	0.564	96	(L2)
Station Keeping 5	2003:071:1350	0.321	50	(L2)
Station Keeping 6	2003:316:1511	0.251	42	(L2)
Station Keeping 7	2004:069:1524	0.663	112	(L2)

Table 1.6: *WMAP* Maneuver Summary. The altitude in the last column is measured either respect to the surface of the Earth (E) or Moon (M).

momentum are 0.215 Nm and 10 Nms respectively. If these values are exceeded then the on-board software invokes "Safehold" mode. The wheels can store a total momentum of ±75 Nms. The event did not pose a performance problem for the ACS at any time.)

To understand this small perturbation on the ACS response, we recall that once the solar arrays are deployed the heavily insulated backside, which forms a solar shield for the instrument, rapidly cools to space. By design, this protects the *WMAP* telescopes from millimeter wave emission from the Sun and reduces the instrument's thermal load to facilitate passive cooling. The solar shield fills approximately one-third of the spacecraft central truss field-of-view. As a result, these cooled surfaces serve as a collection point for outgassing by-products from the central hub electronics, blanketing, and vent paths from the warm portions of the instrument. Based upon the pre-launch configuration, we estimate a mass of ~ 0.8 kg settles on the back of the solar shield in flight. The dominant outgassing component, water, has sufficient energy to be liberated in high vacuum when warmed above 130 K.

Thermal sensors indicate that the Earth infrared exposure was sufficient to sublimate water on the back of the solar shield during the perigee maneuvers. Due to shadowing of Earth IR by the instrument and central hub, the release of the material on the back of the solar array panel was delayed in time. The resultant imbalance in the sublimation rate across the array is consistent with the observed torque magnitude and profile. This basic hypothesis is supported by telemetry from the coarse sun sensors (CCS) and subsequent analysis of *WMAP*'s trajectory. The mass of the sublimate material for each perigee event and ~ 9 day outgassing time constant derived from the telemetry are compatible with the anticipated range of parameters for the *WMAP* observatory. The time between perigee maneuvers and subsequent heating events enabled $\sim 97\%$ of the outgassing products to be dumped from the solar shield before proceeding to L2.

1.3.7 Lunar Fly-by

Although the propulsion system was passive during the lunar swing-by, the encounter has a large influence on the satellite's final trajectory. On July 30, 2001 at 16:37 the lunar swing-by occurred as planned.

1.3.8 Mid-course Correction

To correct the growth of errors from the nominal trajectory to the L2 Lissajous orbit, two mid-course correction (MCC1 and MCC2) burns were planned and executed prior to the first Jupiter beam calibration season. This approach allowed minimal propellant usage and minimized the potential disruption during main beam mapping using Jupiter. The thermal stability of the observatory was sufficiently stable to begin collection of science data on 2001:222 (08/10/2001).

1.3.9   Observing Mode

The spacecraft has six operational modes (see Bennett et al. [2003a] for details) but it spends more than 99% of the time in observing mode. While in observing mode, the spacecraft spins around its vertical (Z) axis every 129.3 s while the Z axis precess around the around the Sun-line every 1 hour described by cone with an half-angle of 22.5°. This compound motion is achieved varying the speeds of the 3 reaction wheels mounted symmetrically around the spacecraft's lower deck (see Figure 1.1). Excess momentum is unloaded during the station keeping maneuvers.

1.3.10   Station Keeping

Three station keeping (SK1, SK2, and SK3) burns were performed to maintain the desired orbit. During these maneuvers the satellite is de-spun to operate in Delta-V mode. Station keeping maneuvers are designed to minimize thermal disturbance and duration. The science data is suitably flagged in the archive to indicate these activities. A list of the station keeping maneuvers is included in Table 1.6.

1.3.11   Pointing

The *WMAP* observatory orientation is controlled by a redundant attitude control system (ACS) which integrates the signals from multiple sensors through a Kalman filter and acts upon a set of reaction wheels and thrusters to maintain the desired spacecraft operational mode. The attitude control system sensors component suite includes:

- Course Sun Sensor (CCS)

- Digital Sun Sensor (DSS)

- 2 Two-Axis Rate Assemblies (TARAs) or Gyroscopes

- 2 Autonomous Star Trackers (ASTs)

Three reaction wheels provide attitude control and an eight thruster (2 roll, 2 pitch, 2 yaw, and 2 backups) propulsion system provides the orbit adjustment capabilities needed to achieve and maintain the correct L2 trajectory. The eight thrusters are also used for attitude control during the orbit maneuvers and for unloading any system momentum buildup on the spacecraft.

   WMAP's ability to reconstruct a full map of the sky from a series of differential measurements depends greatly upon the observatory capability of maintaining a stable highly, inter-linked observing pattern. The motion of the *WMAP* observatory is specified in terms of 3-1-3 Euler angles and rotations specified in *WMAP*'s rotating sun reference (RSR) frame. Because the Z axis of the RSR frame is defined as the vector from *WMAP* to the Sun, the three Euler angles are defined as follows: ϕ, the precession angle about the Sun-line; θ, the angle between the spacecraft Z axis and the Sun-line; and ψ, the spin angle about the spacecraft Z axis. The performance requirements for observing mode are specified in terms of the

ϕ and ψ rates and the θ angle. Table 1.7 shows the observing mode requirements and the in-flight measured performance.

Euler States	Requirements	Pre-Calibration	Post-Calibration
ϕ precession rate (deg/s)	$-0.1 \pm 6.3\%$	$-0.1 \pm 9\%$	$-0.1 \pm 3.6\%$
θ (deg)	22.5 ± 0.25	22.5 ± 0.064	22.5 ± 0.0234
ψ spin rate (deg/s)	$2.784 \pm 5\%$	$2.784 \pm 0.32\%$	$2.784 \pm 0.13\%$

Table 1.7: Observing Mode Performance. The pre-calibration data where measured in flight but using the default calibration coefficients loaded in the ACS before launch. The post-calibration coefficients were uploaded on August 9, 2001, at the end of the in-flight checkout.

1.3.11.1   Pointing Correction

Variations in the telescope pointing reconstruction at the level of ~ 0.5 minute of arc between the various Jupiter observational seasons were noted. By investigating the quaternions derived from the A and B star trackers, this systematic variation was traced to a thermally driven change in the tracker mounting geometry. Tracker mount sensitivities of $\sim 8 \text{arcsec/K}$ correlated with the physical temperature of the solar array are observed. Corrections based upon a simple spacecraft thermal model (see section 1.4.4) are applied to the data remove this residual effect as a smooth function of the orbital phase.

The origin of this effect can be traced to the geometry of the spacecraft hex hub structure used for mounting the trackers [Bennett et al., 2003a, Figure 2]. As the observatory proceeds along its orbit, the lower deck temperature is slowly modulated by $\sim \pm 3K$ due to changes in the sun-to-spacecraft separation distance (see section 1.4). Meanwhile, the passively cooled anti-solar portion of the observatory remains at essentially constant temperature. Due to thermal expansion of the spacecraft structure, the warm end of the hex hub walls rotate toward the $-z$ axis by an angle of order:

$$\begin{aligned} \delta\theta &= R_{hex}\alpha_{Al}\Delta T/H_{hex} \\ &\approx (0.4m)(0.22 \times 10^{-4}/K)(6K)/0.6m \sim 8.8 \times 10^{-5} rad \end{aligned}$$

If uncorrected, this induces an apparent change in tracker elevation of order $\delta\theta_{tracker} \sim 2\delta\theta_{wall} \sim 1.8 \times 10^{-4}$ radians. The pointing error observed in practice, $\sim 1.5 \times 10^{-4}$ radians, is consistent with the results of a thermal-mechanical Finite Element Model (FEM) model of the observatory's flight configuration.

1.4   The Thermal Environment

While a platform at L2 is certainly a much better place than Earth orbit for conducting CMB observations, it is still slightly affected by some solar induced disturbances. In this section

we describe such disturbances and the effects that they have on the instrument stability.

Thermal data from the *WMAP* observatory not only provides a means of monitoring the health and safety of the various on-board systems, but enables one to search for and understand potential instrumental systematic effects. Detailed knowledge of the thermal performance of the observatory in flight is important in assessing the quality of the end data products.

In practice, *WMAP* maintains thermal equilibrium by balancing the absorbed solar radiation input and on-board electrical power dissipation with passive radiative cooling to space. The temperature of the entire spacecraft is extremely uniform due to the vehicle's orbital geometry, constant spin/precession rates and stable power draw. The dominant mechanism that drives changes in the system's temperature is the variation of spacecraft-to-sun separation as a function of orbital position; however, operationally induced changes in spacecraft power dissipation, aging or contamination of the thermal control coatings (e.g., insulating blankets, emissive coatings, reflective surfaces, etc), and solar flare events can also induce measurable thermal effects.

WMAP's thermal performance is monitored by a set of platinum resistance thermometers and thermistors (PRTs) which are installed at key locations throughout the system. A representative summary of the instrument's thermal history for the *WMAP* data is presented in Figures 1.7 - 1.9 and Figure 1.13.
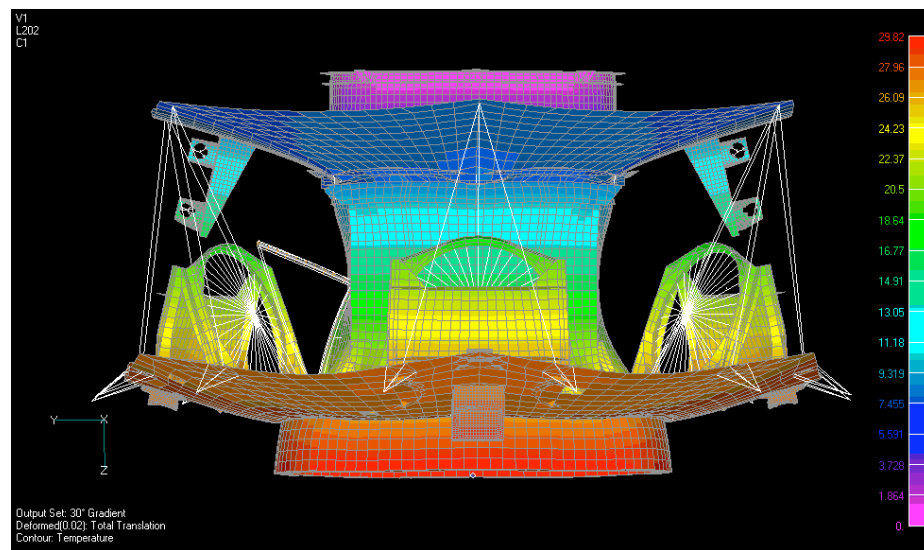
Figure 1.5: *WMAP* Thermal-Mechanical Distortion Finite Element Model (30 K Thermal gradient along spacecraft's z axis. Distortions are overly exaggerated for visualization purposes.
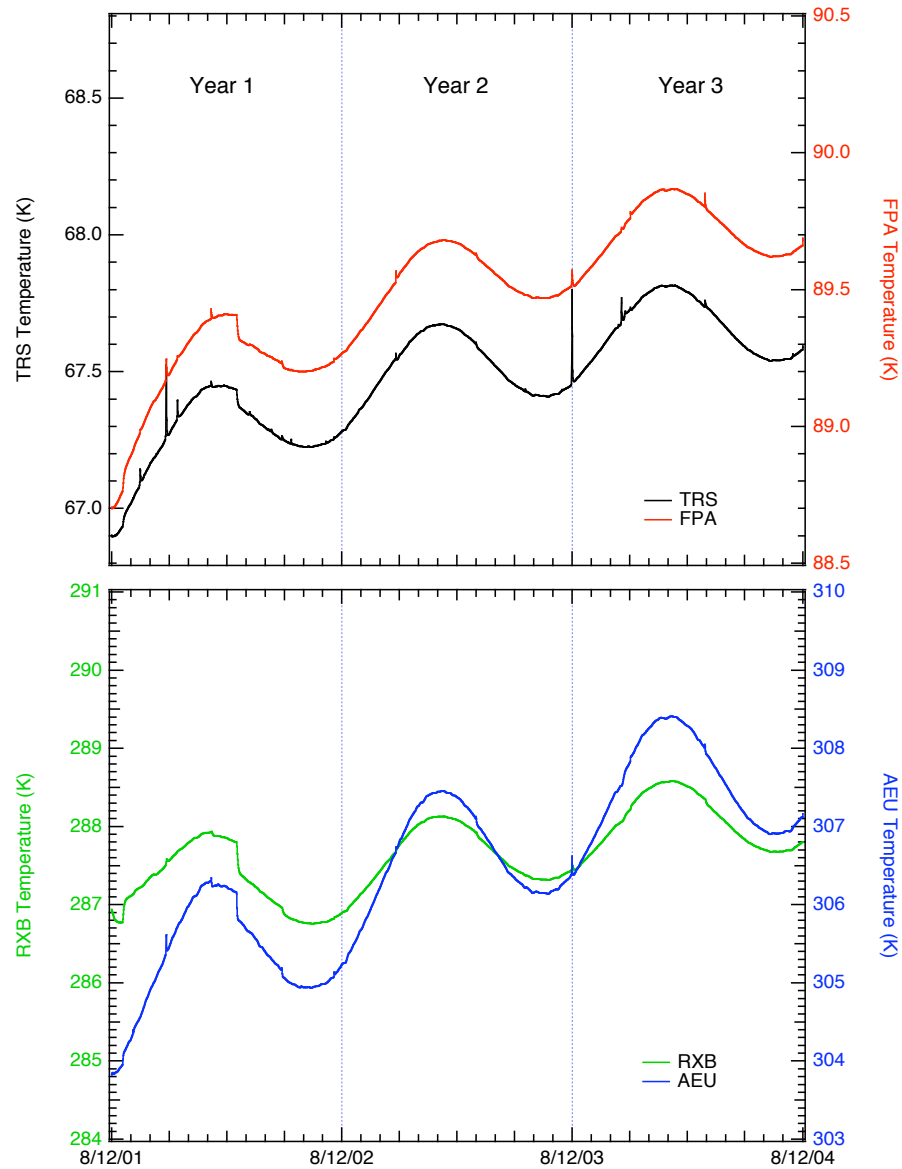
Figure 1.6: Three Years Thermal Profile. The measured thermal profile for the cumulative three years of operation covers 2001:222 (08/10/2001) to 2004:222 (08/10/2004). Expanded plots and details are shown in Figures 1.7, 1.8 and 1.9.
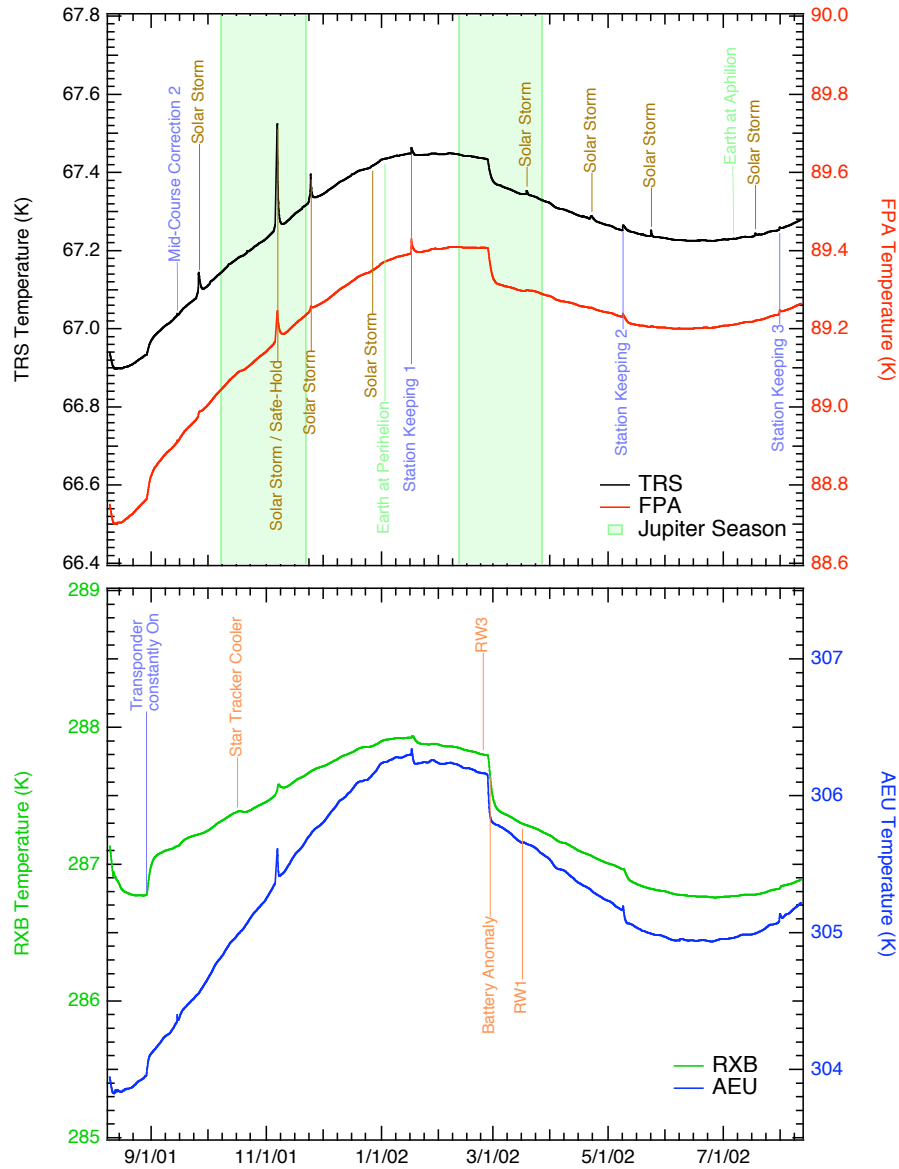
Figure 1.7: First Year Thermal Profile. The measured thermal profile for the first year of operation covers 2001:222 (08/10/2001) to 2002:222 (08/10/2002). Transient events are noted. Modulation from the eccentricity of Sun-Earth L2 orbit is clearly visible. RW1 and RW3 indicate times when there were thermal perturbations due to small changes in reaction wheel drag. See Appendix B for additional details.
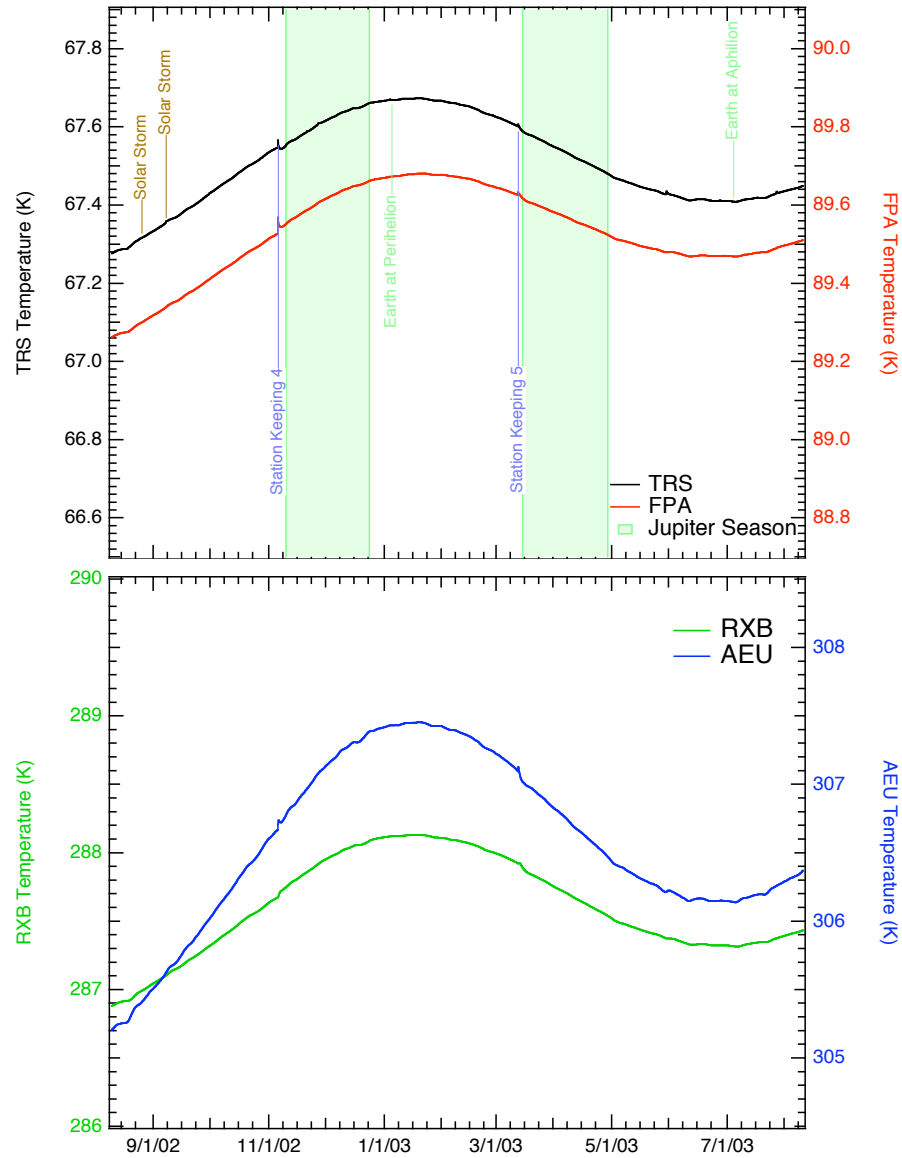
Figure 1.8: Second Year Thermal Profile. The measured thermal profile for the second year of operation covers 2002:222 (08/10/2002) to 2003:222 (08/10/2003). Transient events are noted. Modulation from the eccentricity of Sun-Earth L2 orbit is clearly visible. See Appendix B for additional details.
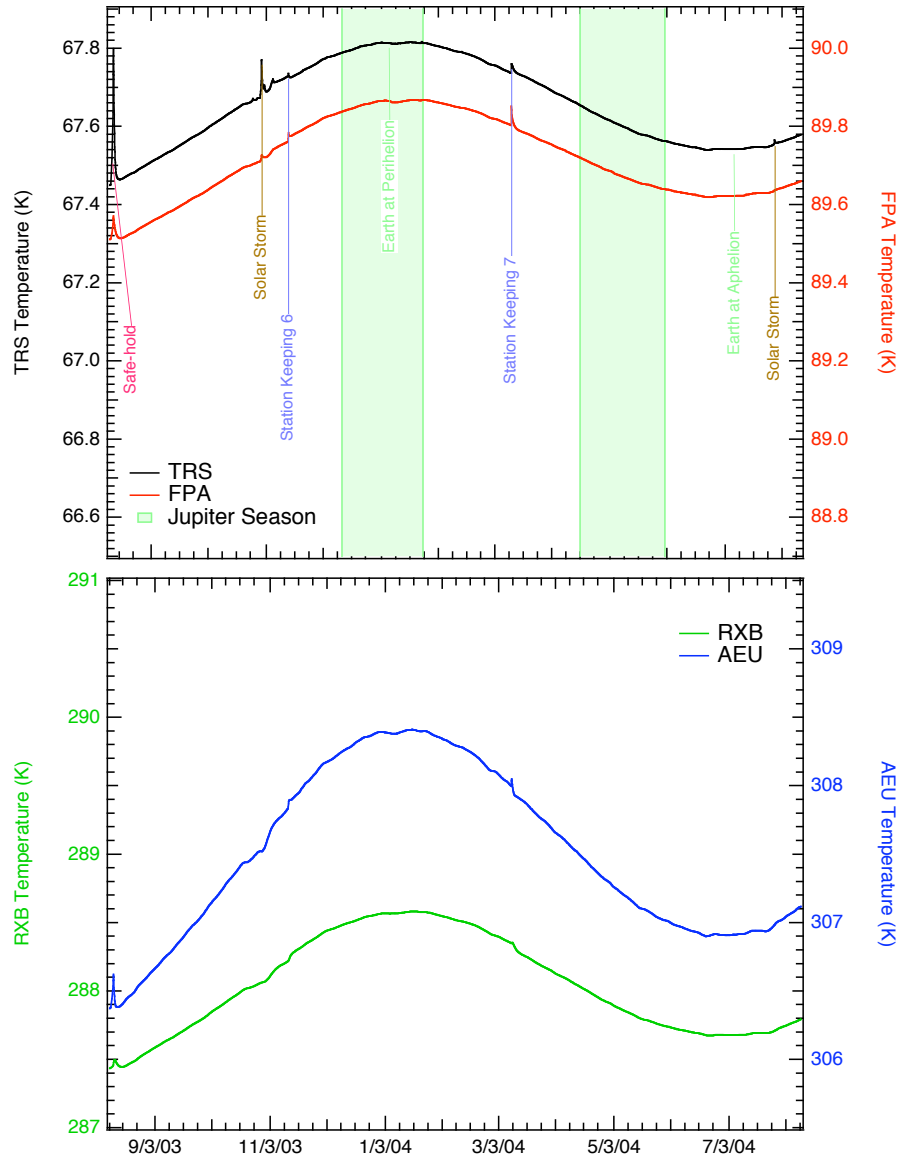
Figure 1.9: Third Year Thermal Profile. The measured thermal profile for the third year of operation covers 2003:222 (08/10/2003) to 2004:222 (08/10/2004). Transient events are noted. Modulation from the eccentricity of Sun-Earth L2 orbit is clearly visible. See Appendix B for additional details.
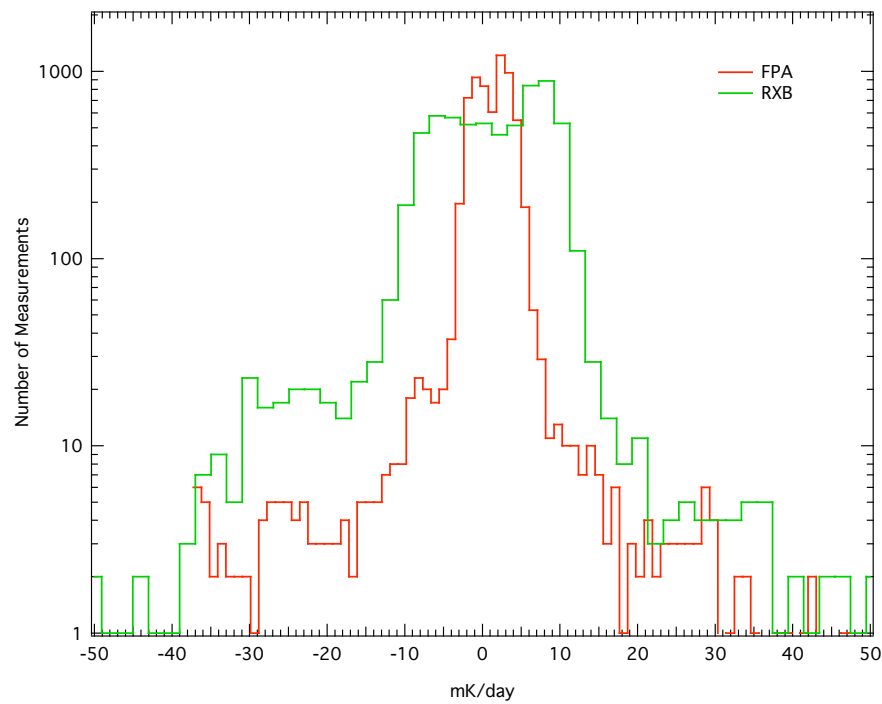
Figure 1.10: Instrument Temperature Rate Histograms. Histograms of the FPA and RXB temperature rates during the first year of science data. The widths of the distributions are 3.9 ± 0.2 mK/day and 11.2 ± 0.6 mK/day for FPA and RXB respectively.

1.4.1 Temperature Monitor Architecture

The *WMAP* instrument temperature monitor system is designed to provide high sensitivity thermometry with sensitivity to temperature drifts and resolution of better than 0.25 mK over a temperature range from 40 K to 340 K. Absolute calibration is of secondary importance with a requirement of ± 1 K accuracy. The primary purpose of the temperature monitor system is to permit the removal of any possible instrument or optics temperature driven offset drifts in the radiometers.

The system uses calibrated Rosemount[2] Platinum Resistance Thermometers (PRTs) energized with a 100 μA rms sine-wave current at 195 Hz. The current is driven on a shielded twisted pair of wires of up to 10 m length. A second twisted pair within the same shield carries the voltage on the PRT back to a high-impedance, gain 100 differential receiver. Both the drive current and sense voltage are analog multiplexed with 30 PRTs and 2 calibration resistors per readout card and two cards for a total of 60 PRT circuits. *WMAP* used 57 PRT channels.
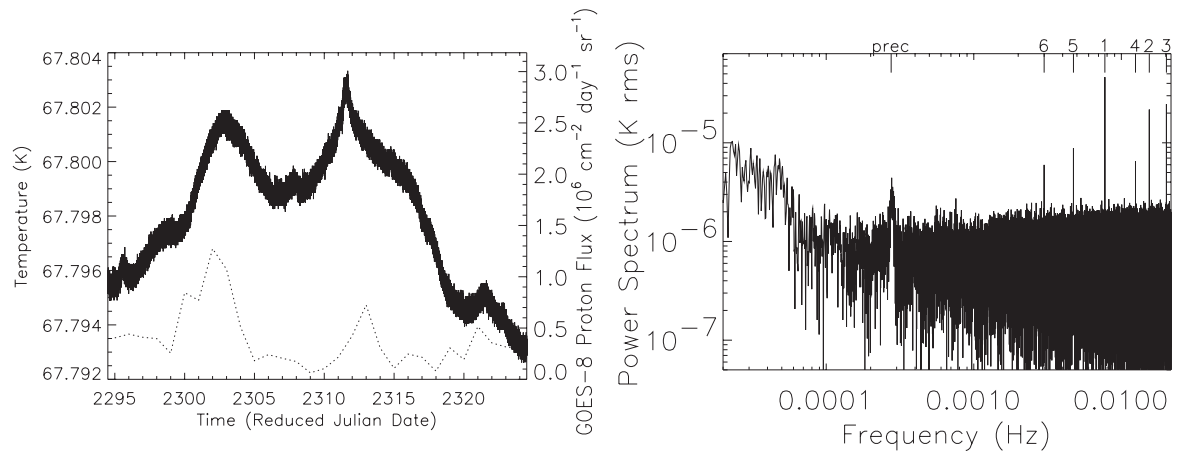
Figure 1.11: PRT Noise Power Spectrum. The left plot is the temperature of the top of the B-side primary mirror for a period of 30 days starting January 20, 2002. The temperature drift is driven by a combination of the changing distance to the sun and solar proton wind. The dotted line is the total solar proton flux as measured by the GOES-8 satellite scaled to the right axis. The right plot is the power spectrum of the temperature over the same period. The low frequency excess is due to the drifts seen on the left. The intrinsic thermometer drift is small relative to the thermal drifts in the system. Special frequencies are marked at the top with labels: "prec" is the spacecraft precession frequency and the numbers indicate the spin frequency harmonic. These are folded back by the Fourier transform. A 45 μK RMS signal is seen at the spin harmonic and is the largest spin synchronous temperature signal seen on the spacecraft. The equivalent measurement noise of the thermometer system is about 1 mK$\sqrt{s}$.

---

[2]Rosemount Aerospace, Inc., "Rosemount Model 118MF Platinum Resistance Temperature Sensor," 1989, Eagan, MN, technical specification.

The PRT sensitivity is approximately $2\Omega/K$, constant over the range 40 to 360 K. The 100 μA excitation gives voltage signal of about $200\mu V_{RMS}/K$. This signal is differenced with a reference sine wave derived from a reference resistor also in the 100 μA current loop. The reference voltage amplitude is set with an 8 bit multiplying Digital to Analog Converter (DAC) which nulls the signal to within ± 4 K. The 8 nulling bits per PRT are stored in the DEU and set a PRT "window". The windows overlap by 40%. The differenced signal is AC coupled, amplified and analog synchronously demodulated. The demodulated voltage is ripple filtered and integrated for 25 195 Hz cycles with a 16 bit synchronous charge-balance V/F ADC. The analog current and voltage sense multiplexers switch between PRTs after the sample integration is complete. Each PRT sample is a therefore a 24 bit number including the 8 bits of window information. The gain is set so that the temperature resolution is 125 μK/ADC unit. Each PRT is read once each 23 seconds (i.e., ~ 4 measurements per spin rotation) but not synchronously with the spin.

Assigning a resistance to the digital word for each thermometer sample requires the calibration of the ADC with the window DAC. Because the window DAC has differential non-linearity, the window sizes are not all identical. This leaves jumps in the calculated resistance when switching from one window to another. Because the purpose of the thermometry is largely to monitor temperature variations, these jumps are not important since no window transitions are expected once the temperatures stabilize during the data taking part of the mission. Because the windows overlap by 40%, a transition to the next window starts near the center of the new window minimizing window transitions. The correct window is found either with a binary search at startup, by command or after a saturated ADC samples two times in a row. The binary search is controlled by the DEU. During normal operations, a window transition is initiated when a PRT reading is within 10% of the edge of the current window.

1.4.2 Temperature Monitor Performances

The sensitivity and stability of the temperature monitors is shown in Figure 1.11. Shown is a section of time where the solar input was not changing quickly because the observatory was at the minimum distance from sun and with no large solar flares to drive a thermal disturbance. The sensor shown is mounted to the top of the B-side primary mirror and shows the most thermal variation of any of the sensors. The power spectrum shows low-frequency power from the slow thermal drift of the changing distance to the sun and variations due to solar activity. There is also a ~ 45 μK RMS signal at the spin period of the spacecraft. The equivalent noise power spectral density is ~ 1 mK$\sqrt{s}$ for each of the thermometers.

Temperature calibration of the sensors is derived from the Rosemont calibration curves. Uncorrected offsets in the post-demodulation electronics and differential non-linearity in the window DAC result in an absolute temperature error of ± 1 K. The accuracy of temperature variations is derived from reference to precision resistors measured each multiplexing cycle.

Several of the thermal sensors in the FPA assembly exhibit variations which exceed that anticipated from an ideal PRT channel by a factor of several in flight on a time scale of hours. An example of interest is provided by DFW32FPATEET. See Figure 1.12 for power spectrum.

In addition to the long-term overall thermal drifts, short-term variations of order 1 mK can be seen in the time order data on this sensor. One observes that this signature is reproduced with smaller amplitude in PRT channels DFW3AOMTT and DFW3BOMTT. This signature is consistent with the presence of a random variation in the physical temperature near this location. From the instrument's thermal parameters, one estimates that this requires a variation in power dissipation $\sim 100\mu W$ in the vicinity of the W3A magic tee.
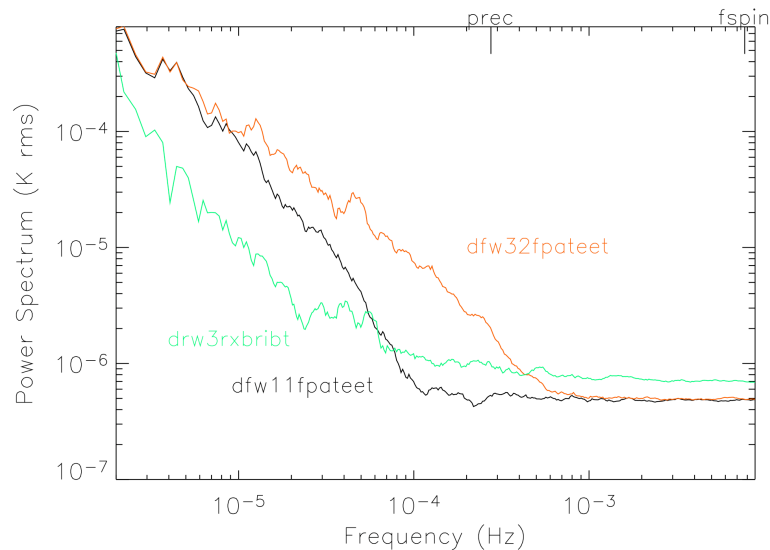
Figure 1.12: FPA and RXB Temperature Power Spectra. PRTs DFW32FPATEET and DFW11FPATEET are mounted on the cold hybrid tees of W32 and W11 radiometers respectively. DRW3RXBRIBT is mounted on an aluminum rib that supports the W3 DA inside the RXB. DFW32FPATEET shows sign of excess thermal variations as described in the text. These power spectra essentially define the envelope of the RXB and FPA temperature stability.

Data from the radiometer outputs and monitors were searched for signals correlated with the variance in DFW32FPATEET temperature sensor. We note that the resolution of the HEMT drain current monitor is sufficient to eliminate the possibility of a bias instability as the primary source of the fluctuations. This effect was not detected in the science data or instrument gain. In addition, the spacecraft housekeeping data were investigated for correlation with on-board activity and the observed effect. The non-detection of a source at the levels investigated suggests that the most likely candidate is a variation in one of the LED bias circuit channels. (note: The LEDs are used to illuminate the HEMT amplifier channel and are operated near saturation.) The fractional variations in the radiometer's total

power monitor, $dT_{sys}/T_{sys} \sim 6 \times 10^{-4}$, dominate over the influence of thermal variations, $dT_{amb}/T_{amb} \sim 1 \times 10^{-5}$. This has a negligible influence on the instrument gain calibration model [Jarosik et al., 2003a]. The presence of this noise source at this level has negligible impact upon the quality of the science data.

1.4.3 Sun Driven Yearly Temperature Changes

By design, the spacecraft has a large thermal gradient from its sunlit to dark-side. Temperatures for sensors range from ~ 330 K for objects directly illuminated by the sun to ~ 60 K for elements passively cooled to space. The variation in the satellite's distance from the sun as it progresses around its orbit at L2 changes the observatory's average temperature. To estimate the magnitude of this effect we consider the ratio of the solar flux intercepted at the maximum and minimum distance from the sun in the orbit. For a radiatively cooled object in an orbit with numerical eccentricity ε, one finds a relative change in the temperature on the sunlit side of order $dT/T_{amb} \sim \varepsilon \ll 1$. To a good approximation, for the *WMAP* orbit, the eccentricity is equal to that of the Earth, $\varepsilon = 0.017$, yielding an estimated orbital change with temperature of order ~ 5 K for sensors well coupled to objects receiving direct illumination.

Over the course of the first year of observations, for directly illuminated objects, the component of the thermal signature correlated with the satellite-to-solar distance was ~ 4 K. For objects shaded from the sun, the thermal isolation provided for in the design reduces the overall magnitude of this effect. For example, a typical electronics box mounted on the shaded side of the spacecraft hub experienced a temperature correlated with solar distance with amplitude of ~ 1 K. Over the same period of time the thermal reflector system's temperature, which is shaded from direct solar input and well thermally tied to the radiator panels, was noted to change by less than ~ 0.2 K. This is consistent with the performance anticipated from a detailed analysis of the thermal design.

1.4.4 Aging of Thermal Control Surfaces

In flight, exposure of the thermal control surfaces to ultraviolet radiation, charged particles, and surface contamination are anticipated to increase solar absorptance while leaving the infrared emittance essentially unchanged [Triolo et al., 1977, Gilmore and Bello, 1994]. Published data on the degradation of materials in flight are essentially limited to the more tenuous GEO and LEO environments; however, qualitatively similar trends are anticipated for *WMAP*. Contamination by outgassing of volatile condensible materials, which are subsequently darkened by UV exposure, are anticipated to cause an initial modest increase in the effective aging rate for the first few months to year of the mission. As the outgassing rate tapers off, a slow and monotonic degradation of the coating performance is expected. Such a trend is consistent with the observed thermal performance of the *WMAP* observatory over the first year as presented in Figure 1.13 after taking into account contributions arising from the modest changes in the spacecraft's internal power dissipation.

A simple model of the long term temperature profile of the spacecraft can be written as the product of two term: a sinusoidal one accounting for the change in temperature due to the
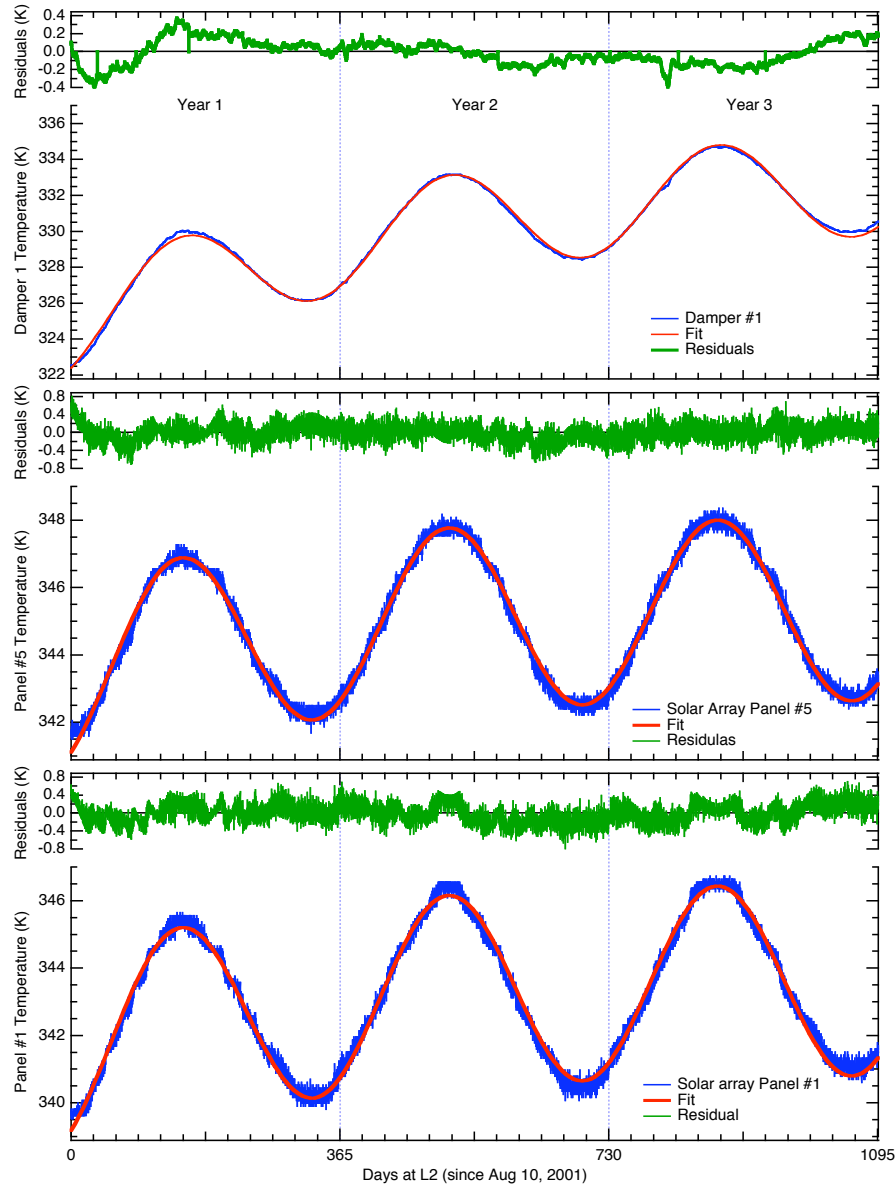
Figure 1.13: Solar Array Temperature Profile. The Damper sensor is mounted on the hinge's damper of solar array panel 1 while the two panel sensors are mounted directly on solar panel 1 and 2. These two sensors are thermistors and are not part of the instrument's temperature monitoring system described in section 1.4.1, the excess noise in the solar array sensors is due to the spacecraft temperature readout. Both datasets have been edited to remove spikes induced by the maneuvers and other singular events. Fits to the model described in the text are also displayed.

L2 motion around the Sun and an exponential one accounting for the change in absorptance due to the degradation of the spacecraft's surfaces. This can be written as

$$T(t) = T_\circ \left(1 + \frac{\delta a}{4 a_\circ} \left(1 - e^{-t/\tau} \right) \right) \left(1 + \frac{\delta R}{2 R_\circ} \sin(\omega t + \phi) \right),$$

where $T_\circ$ is the initial equilibrium temperature of the spacecraft, $a_\circ$ the initial absorptance, δa the change in absorptance over a time large compared to the surface degradation time constant τ, δR is the departure from a circular orbit of radius $R_\circ$ and we assume that $\delta a/a_\circ$ and $\delta R/R_\circ$ are small compared to unity. Setting ω equal to 2π over 1 year and fitting for all the other parameters we obtain:

Parameter	Damper 1 year	Damper 3 years	Panel #1 3 years	Panel #5 3 years	
$T_\circ$	324.5	324.7	341.5	343.3	[K]
$\delta R/R_\circ$	-0.017	-0.017	-0.017	-0.016	[-]
$\delta a/a_\circ$	0.10	0.11	0.026	0.024	[-]
τ	410	507	294	271	[days]
ϕ	2.16	2.16	2.19	2.18	[rad]

The value of $\delta R/R_\circ$ is in good agreement with Earth's orbit eccentricity (0.0167) and a 10% change in absorptance is also consistent with previous observations of surface degradation [Gilmore and Bello, 1994].

More accurate determination of the effective aging rates for the thermal control surfaces will be possible as the length of the observational data record is increased. In particular, the observed degeneracy between the time constant for the degradation in the coating performance and an increase in the solar absorptance has been reduced with three years of operations.

1.4.5 Operationally Induced Disturbances

Control over the spacecraft's solar absorptance, radiative cooling, and dissipated power density are used to maintain a stable operational temperature for the various components. During nominal operation, changes in the power dissipation in the various electronics boxes have, by design, a negligible impact on the instrument performance. As a rule, as described in Bennett et al. [2003a], passive thermal control is employed for normal observing mode. Survival heaters, which are nominally "off", are engaged by mechanical thermostats in case of an emergency and the star tracker Peltier coolers which have an internal set point will actively adjust.

Slight changes in *WMAP*'s power dissipation were encountered in maintaining the system. A summary of the instrument's thermal performance is presented in Figures 1.7 - 1.9. Several operationally induced disturbances of potential interest from the events log (Appendix B) are indicated. The dominant thermal disturbances in this time frame result from the decision to leave the transponder on and a partial short of a battery cell which subsequently resulted a

change in the power system's nominal voltage. During station keeping maneuvers it is necessary to change in *WMAP*/Sun-line angle. Secondary thermal perturbation sources which occur during these periods include pre-heating the thrusters to operate with approximately optimal and known efficiency, changes in reaction wheel dissipation after momentum unload, and autonomous changes in the power system solar array configuration. Maneuvers and other operationally induced thermal events which may induce noise in the calibration, are flagged. See Table 1.8.

1.4.6 Radiometric Baselines Discontinuities

During the first year of observations 21 sudden step-like changes in the radiometers outputs were observed. These events have been identified as small changes in the properties of several microwave components resulting from the sudden release of internal stress and are presumably thermally driven. The observed step-like shifts in output are not correlated with changes in HEMT bias. These small steps in radiometer output can be categorized and their point of origin in the system understood by the symmetry of the observed response:

- Waveguide Creep Mode: Differential-mode change in radiometric output (i.e., science signals move with equal and opposite magnitude) induced by slight change in waveguide loss or reflectively prior to input magic-tee. Signature mimics a small but sudden change in noise temperature.

- Phase Switch Mode: Common-mode step in science output of both radiometer diode readout channels (i.e., science signals move with equal and common magnitude). Can induce second order common mode RF bias. Motion of phase matched waveguide sections could produce similar signatures; however, given the mounting geometry, one anticipates that this would produce relatively slow changes in response rather than producing a sudden step.

- Filter Mode: Step in RF bias of a single diode channel. Signature is consistent with small change total power (i.e., shift in detector diode responsively or band-pass filter bandwidth) after second magic tee.

A typical event is of order ~ 1 mK in amplitude and ones knowledge of the transition time is limited by the data sample rate. In practice, these small events do not cause a discernible change in the DA gain or noise properties. Given the calibration time scale for the system, ~ 1 hour of data on either side of the event is removed, each cut is additionally padded by 1.2 hours on each side by the baseline fitting routine [Hinshaw et al., 2003a]. A data loss of $\sim 0.1\%$ is incurred in processing these events. In flight, steps have been observed in radiometer channels W12, W11, Q12 Q11, K11, Ka11 in decreasing order of frequency of event occurrence. Of the 21 events, 2 affected more than one radiometer channel. The most probable cause of coupling between nearly coincident events is due to the mechanical layout of the radiometer mounting structures. From the band-to-band and channel-to-channel consistency of the maps we conclude that all channels have similar statistical properties after removal of the baseline steps in processing [Hinshaw et al., 2003a].

Cut From	To	DA Flag	Notes
yyyy:ddd:hhmm	yyyy:ddd:hhmm		
2001:223:1800	2001:223:2130	[0,0,1,0,0,0,0,0,0,0]	Q1 dT glitch
2001:230:1600	2001:230:2010	[0,0,0,0,0,0,1,0,0,0]	W12 dT glitch
2001:245:1930	2001:246:0110	[0,0,1,0,0,0,0,0,0,0]	Two close Q1 dT glitches
2001:249:0600	2001:249:1010	[0,0,0,0,0,0,1,0,0,0]	Small W12 dT glitch
2001:257:1500	2001:258:0900	[1,1,1,1,1,1,1,1,1,1]	Mid-Course correction #2
2001:282:1700	2001:282:2030	[0,0,0,0,0,0,1,0,0,0]	Small W12 dT glitch
2001:309:1630	2001:311:0000	[1,1,1,1,1,1,1,1,1,1]	Solar Storm Induced Safe-hold
2001:316:2300	2001:317:0300	[0,0,1,0,0,0,0,0,0,0]	Small Q12 dT glitch
2002:013:0810	2002:013:1130	[0,0,0,0,0,0,1,0,0,0]	W12 dT glitch
2002:016:1500	2002:016:2330	[1,1,1,1,1,1,1,1,1,1]	Station Keeping #1 (SK1)
2002:053:0500	2002:053:1000	[0,0,0,0,0,0,1,0,0,0]	W12 dT glitch
2002:053:1700	2002:053:2030	[0,0,0,0,0,0,1,0,0,0]	W12 dT glitch
2002:057:0200	2002:057:1022	[1,1,1,1,1,1,1,1,1,1]	Change to VT0
2002:066:2000	2002:067:0000	[0,0,0,0,0,0,1,0,0,0]	W12 dT glitch
2002:068:2230	2002:069:0200	[0,0,0,0,0,0,1,0,0,0]	W12 dT glitch
2002:082:2000	2002:082:2300	[0,0,0,0,0,0,1,0,0,0]	W12 dT glitch
2002:085:0100	2002:085:0400	[0,1,0,0,0,0,0,0,0,0]	Ka123 RF bias glitch
2002:092:1140	2002:092:1530	[0,0,0,0,0,0,1,0,0,0]	W12 dT glitch
2002:097:1005	2002:097:1410	[0,1,0,0,0,0,0,0,0,0]	Ka114 dT and RF bias glitch
2002:100:0600	2002:100:0930	[0,0,0,0,0,0,1,0,0,0]	W12 dT glitch
2002:100:2210	2002:101:0200	[0,0,0,0,0,0,1,0,0,0]	W12 dT glitch
2002:123:0200	2002:123:0530	[0,0,0,0,0,0,1,0,0,0]	W12 dT glitch
2002:128:1400	2002:129:0000	[1,1,1,1,1,1,1,1,1,1]	Station Keeping #2 (SK2)
2002:211:1456	2002:212:0100	[1,1,1,1,1,1,1,1,1,1]	Station Keeping #3 (SK3)
2002:269:0202	2002:269:0426	[1,0,0,0,0,0,0,0,0,0]	K11 dT and RF bias glitch
2002:273:0822	2002:273:1046	[0,1,0,0,0,0,0,0,0,0]	Ka11 dT and RF bias glitch
2002:309:1805	2002:310:0405	[1,1,1,1,1,1,1,1,1,1]	Station Keeping #4 (SK4)
2002:314:0720	2002:314:1040	[0,0,0,0,0,0,1,0,0,0]	W12 dT glitch (marginal)
2002:321:0450	2002:321:0812	[0,0,0,0,0,0,1,0,0,0]	W12 dT glitch (marginal)
2003:071:1235	2003:071:2315	[1,1,1,1,1,1,1,1,1,1]	Station Keeping #5 (SK5)
2003:081:0130	2003:081:0600	[0,0,1,0,0,0,0,0,0,0]	Q12 dT glitch
2003:085:0945	2003:085:1400	[0,0,1,0,0,0,0,0,0,0]	Q12 dT glitch
2003:145:0644	2003:145:0940	[1,1,1,1,1,1,1,1,1,1]	Recorder overflow
2003:156:0848	2003:156:1412	[0,0,0,0,0,0,1,0,0,0]	W12 dT step, plus assoc W11
2003:222:1530	2003:225:0112	[1,1,1,1,1,1,1,1,1,1]	MV reset induced SafeHold
2003:301:2245	2003:302:0420	[1,1,1,1,1,1,1,1,1,1]	Solar activity induced switch to ASTB
2003:316:1335	2003:317:0000	[1,1,1,1,1,1,1,1,1,1]	Station Keeping #6 (SK6)
2004:069:1400	2004:070:0100	[1,1,1,1,1,1,1,1,1,1]	Station Keeping #7 (SK7)
2004:178:1639	2004:178:1903	[0,0,0,0,0,0,1,0,0,0]	W12 dT glitch

Table 1.8: Data Cut Summary. Each line consists of a start time, a stop time and ten element array indicating which DAs are affected, ([1,0,0,0,0,0,0,0,0,0] = K, [0,1,0,0,0,0,0,0,0,0] = Ka, etc.). Each cut is additionally padded by 1.2 hours on each side by the baseline fitting routine. Additional cuts are made for Jupiter, Saturn, Mars, Uranus and Neptune if the planet lies within 1.5° radius of a DA's line-of-sight on either the A or the B side.

1.5 The Radiation Environment

1.5.1 Plasma Environment

The Earth's auroral tail is collimated by the solar wind and has a nominal radius of $\sim 20 R_E$ at L2. Variations in the solar wind velocity and direction drive fluctuations of the auroral tail from its average position by up to a few tail radii in extent. In an idealized picture, the magnetospheric lobes are relatively small and the magnetosheath has higher density than the lobes but less than the solar wind. Streaming plasma in this region will see essentially open magnetic field lines and it is easier to exhaust out the end than confine the plasma in this region.

To place this in perspective for *WMAP*, we recall the Earth's angular extent as viewed from $\sim 240 R_E$ at the L2 halo orbit is in the range of $1° < \theta < 10°$. Based upon these inputs we estimate the major and minor axis of the *WMAP* orbit to be $\sim 4 R_E$ and $\sim 40 R_E$ respectively. Thus, at L2, the spacecraft will experience the auroral tail, lobes, magnetosheath, and solar wind plasma. In principle, the halo orbit places the satellite inside the magnetosheath for extended periods of time; however, in reality, rotation of Earth's magnetic field and solar wind drive large perturbations from the simple static picture. The surface and internal charge control design described in Bennett et al. [2003a] are compatible with these anticipated environmental conditions.

1.5.2 Spacecraft Charge Control

If the accumulation of charge in an electromagnetic structure exceeds the dissipation rate, a discharge occurs when the critical field strength of the configuration is exceeded. In the space environment, such events can be initiated by sudden changes in electromagnetic field, plasma density, or mechanical stress. The resultant rapid release of electromagnetic energy can induce spurious electrical responses or result in damage to components. In this context, faults in spacecraft performance can result from several basic mechanisms [Frederickson, 1996a,b, Adamo and Matarrese, 1983, Leung et al., 1986, Mizera, 1983].

- Coupling to circuitry increases noise and corrupts desired signal.

- Field strength exceeds dielectric strength and induces mechanical failure.

- Localized heating induces stress which exceeds material strength.

Such discharges can be conducted along wires or ground planes, radiated through free space to a structure that acts as a pick-up antenna, or be directly injected into a circuit. For these reasons, the control of surface and internal charge by proper coating selection, return impedance level, and shielding against electromagnetic and ionizing radiation must be considered for reliable spacecraft operation.

In the case of the *WMAP* observatory, all susceptible circuits are enclosed by an equivalent stopping power of 0.16 cm of aluminum. Grounded lead and copper foils were used to locally

augment the available shielding where required in the system. For particularly sensitive subsystems, the signal lines in the harness were filtered or clamped with diode limiters to improve overall immunity. Addition charge control mitigation approaches are outlined in Bennett et al. [2003a].

For the charging environment experienced in the phasing loop portion of the mission *WMAP*, surface discharges can potentially induce electrical transients in the system. Such considerations are of particular interest for elements of the system with a low damage threshold to electrostatic discharge. Charge control objectives were achieved while simultaneously satisfying the thermal design goals by using appropriate dissipative surfaces ($< 10^9 \Omega/\square$) in electrical contact with the spacecraft ground. Materials employed included dissipative paints, indium-tin-oxide films, carbon loaded polymers, thin SiOx coatings on metallic substrates, and conductive tapes. The use of low loss dielectrics exposed to the ambient space plasma in un-illuminated regions is limited to unavoidable patches with area $< 10^{-3}$ of the total surface area. In regions of the spacecraft where photoemission is present, larger dielectric regions can be and are employed. Radiated electromagnetic threats are broadband in nature [Leung and Plamp, 1982] and band-limited by the input waveguide cutoff or input circuitry.

1.5.3 Solar Flares: Charged Particle Heating

Particle heating by the solar wind can produce a small time variable thermal load on the spacecraft (see for example, Jimenez [1988], Vampola et al. [1989]). This effect is a concern when the power deposited by the incident charged particle flux approaches the cooling power available to the system. In practice, this is predominantly a concern for surfaces cooled to low temperatures. Since the *WMAP*'s optics have relatively large thermal mass and operate at a physical temperature around 70 K this is a negligible but measurable effect. In fact, by correlating the GOES-8 proton monitor (`http://sec.noaa.gov/today.html`) with the precision thermal sensors data from the *WMAP* instrument package, we note that such an effect is observable on the TRS and outer bulk heads of the FPA.

As an illustrative example we consider the heating of the *WMAP* primary reflector that occurred during September 26, 2001 solar proton event. This is an example of a severe solar storm with the > 10 MeV proton flux reaching 10^5 times nominal levels. During the event, a thermal change with amplitude $dT \sim 0.06$ K correlated with the event was observed in the primary reflector sensors. From the thermal properties of the TRS in its flight configuration, a change in power loading on the reflector of ~ 6 mW was inferred. One notes for an effective thickness, $dt > 0.5$ mm of aluminum, essentially all incident particles with an energy < 10 MeV, dissipate their energy in the composite structure.

In effect, this portion of the system acts as a bolometric particle detector: the primary reflector serves as an absorber for low energy particles from the solar wind, the PRT is a thermal sensor element, and passive cooling to the sky serves as weak link to the thermal reservoir. A calibration of this bolometric response can be derived from the observed change in temperature which resulted from the removal of RF power to the Z omni antenna (see Appendix B *WMAP* Events Log, 2001:219). The cable which runs through the cavity formed by the back-to-back reflectors on the TRS provides a known ohmic load for calibration. The
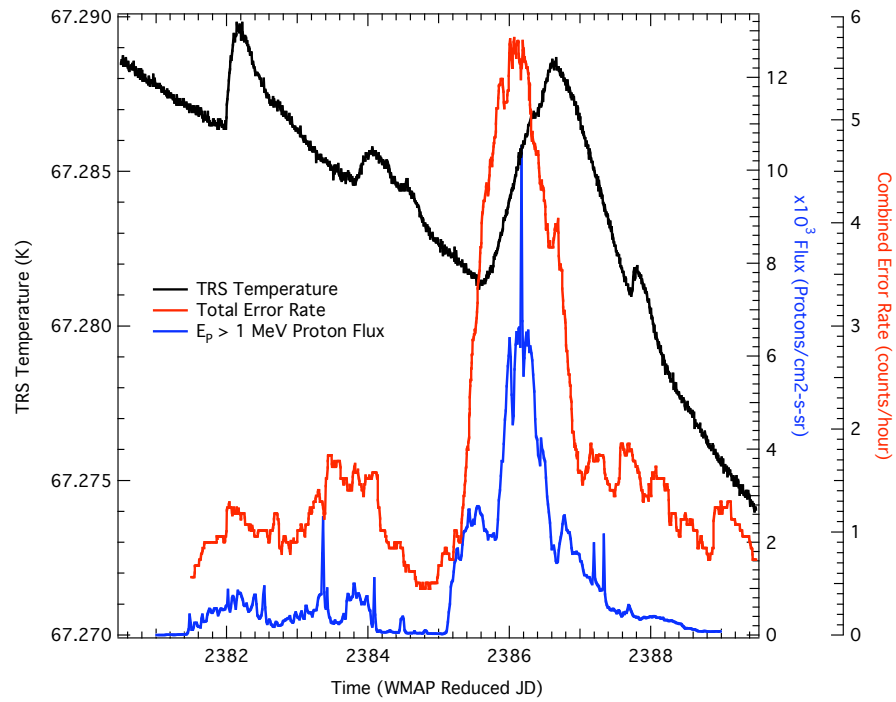
Figure 1.14: Solar Flare Effects on the Observatory. This plot shows the effects of a solar flare (April 17, 2002) on the TRS temperature and on the combined (on-board computer and data recorder) single-bit error rate. The proton data are from the GOES-8 satellite.

observed thermal response is consistent with the power deposition by the incident particle flux. We conclude that the instrument's observed thermal behavior is consistent with the absorption of an enhanced number of low energy particles encountered during the solar proton event. Given the mm-wave emissivity of the reflector surfaces [Page et al., 2003b], magnitude, and timescale of the thermal response, the resultant differential microwave emission is insufficient to influence the science data.

Event Date	$E_p \geq 1$MeV p/cm^2 sr day	$E_p \geq 10$MeV p/cm^2 sr day	$E_p \geq 100$MeV p/cm^2 sr day	Reflectors ΔT(mK)
09/26/01	1.40E+09	2.70E+08	1.80E+06	60
11/06/01	2.40E+09	6.20E+08	3.60E+06	–
11/24/01	2.30E+09	3.80E+08	2.00E+05	70
12/27/01	6.80E+07	2.40E+07	6.20E+05	3
03/18/02	2.90E+08	1.90E+06	3.50E+03	12
04/22/02	3.30E+08	1.30E+08	1.20E+06	10
05/23/02	2.60E+08	6.80E+06	2.80E+03	16
07/17/02	2.50E+08	6.40E+06	4.20E+03	8
08/25/02	7.00E+07	6.80E+06	2.10E+04	0
09/07/02	1.00E+08	2.10E+06	3.20E+03	5
10/29/03	3.00E+09	7.70E+08	5.20E+06	95
07/27/04	2.70E+08	9.50E+06	2.10E+03	12
09/14/04	4.60E+08	8.50E+06	2.70E+03	8

Table 1.9: Solar Storms. Major storms encountered by the observatory from launch to the end of the first year data release. The proton data are from the GOES-8 and GOES-11 satellites. The spacecraft went into safe-hold mode during the November 6, 2001 solar storm.

Chapter 2

Data Products

Each section of this chapter contains the description of a particular delivered data product and contain at least the following information:

- Description of the data

- Data format

- Quick summary of the methodology use to obtain the data set

- References to papers describing the more technical details.

The time-ordered data are described in Chapter 3. More information on how to read both maps and time-ordered data are contained in Chapter 4 and in Appendix C. All the data can be downloaded at:

`http://lambda.gsfc.nasa.gov/`

2.1 Derived CMB Products

2.1.1 Combined TT Power Spectra

Units	μK^2
Format	ASCII
# of Files	2

The 3-year TT power spectrum is produced by combining the Maximum Likelihood estimated spectrum from $l = 2 - 10$ with the pseudo-C_l based cross-power spectra for $l > 10$. The pseudo-C_l estimate uses only V- and W-band data, with a uniform pixel weight applied for $l \leqslant 500$ and N_{obs} weights for $l > 500$. A total of 153 individual cross-power spectra are formed from the three individual years of data and six V- and W-band differencing assemblies.

The complete (unbinned) TT power spectrum data are provided as an ASCII table containing the following columns:

- the multipole moment l

- the power spectrum in units of μK^2

- the corresponding diagonal elements of the covariance matrix

- the portion of the diagonal element of the covariance matrix attributed to measurement errors

- the portion of the diagonal element of the covariance matrix attributed to cosmic variance, assuming the best-fit ΛCDM model described in Spergel et al. [2006].

The diagonal elements provide an estimate of the error, but should not be used as exact error bars. The complete Fisher matrix should be used for that purpose.

A binned version of the power spectrum is also available, in a separate file whose format and content are similar to those described above for the unbinned data. The choice of l bins is the same as that used in e.g., Figure 16 of Hinshaw et al. [2006].

More details can be found in:

> G. Hinshaw, M. R Nolta, C. L. Bennett, R. Bean, O. Doré, M. R. Greason, M. Halpern, R. S. Hill, N. Jarosik, A. Kogut, E. Komatsu, M. Limon, N. Odegard, S. S. Meyer, L. Page, H. V. Peiris, D. N. Spergel, G. S. Tucker, L. Verde, J. L. Weiland, E. Wollack, and E. L. Wright. Three-Year Wilkinson Microwave Anisotropy Probe (WMAP) Observations: Temperature Results. *ApJ, submitted*, 2006

> D. N. Spergel, R. Bean, O. Doré, M. R. Nolta, C. L. Bennett, G. Hinshaw, N. Jarosik, E. Komatsu, L. Page, H. V. Peiris, L. Verde, C. Barnes, M. Halpern, R. S. Hill, A. Kogut, M. Limon, S. S. Meyer, N. Odegard, G. S. Tucker, J. L. Weiland, E. Wollack, and E. L. Wright. Three-Year Wilkinson Microwave Anisotropy Probe (WMAP) Observations: Cosmological Parameters. *ApJ, submitted*, 2006

2.1.2 TE Power Spectra

Units	$\mu\mathrm{K}^2$
Format	ASCII
# of Files	2

The TE power spectrum is computed using a pseudo-C_l estimator for the region outside the P06 mask in P and outside the Kp2 mask in T. The foreground-cleaned V band with uniform weighting is used for T. The combined foreground-cleaned Q and V bands are used for P. Polarization weighting uses the full N_{inv} weighting for $l \leqslant 16$ and N_{obs} weighting for $l > 16$.

The TE power spectrum data are provided as a table containing the following three columns:

- the multipole moment l

- the power spectrum in units of $\mu\mathrm{K}^2$

- the corresponding diagonal elements of the covariance matrix

The diagonal elements provide an estimate of the error, but should not be used as exact error bars. The complete Fisher matrix should be used for that purpose.

A binned version of the power spectrum is also available, in a separate file whose format and content are similar to those described above for the unbinned data. The choice of l bins is the same as that used in e.g., Figure 22 of Hinshaw et al. [2006].

More details can be found in:

G. Hinshaw, M. R Nolta, C. L. Bennett, R. Bean, O. Doré, M. R. Greason, M. Halpern, R. S. Hill, N. Jarosik, A. Kogut, E. Komatsu, M. Limon, N. Odegard, S. S. Meyer, L. Page, H. V. Peiris, D. N. Spergel, G. S. Tucker, L. Verde, J. L. Weiland, E. Wollack, and E. L. Wright. Three-Year Wilkinson Microwave Anisotropy Probe (WMAP) Observations: Temperature Results. *ApJ, submitted*, 2006

2.1.3   Cosmological Parameter Table

Analysis of the *WMAP* data involved the computation of cosmological parameters assuming a variety of models and including a variety of datasets in addition to the *WMAP* datasets. The various model/dataset combinations that were tested are displayed in Table 2.1. In the equivalent table available on the `LAMBDA` web site the combinations that were analyzed have links in the corresponding cells to individual display pages that show the cosmological parameters computed using that combination of model and dataset. A printable version of each list of parameters is made available as a Postscript file through a link to its corresponding individual model-data combination display page; these Postscript files list the error information associated with each parameter.

Model	wmap	2df	bao	boom+ acbar	cbi+ vs	hst	sdss	sn astier	sn gold	wl	all
lcdm	✓	✓	✓	✓	✓	✓	✓	✓	✓	✓	✓
lcdm+kcutlin	✓										
lcdm+kcutlog	✓										
lcdm+mnu	✓	✓					✓				✓
lcdm+mnu+nrel		✓					✓				✓
lcdm+nrel		✓					✓				✓
lcdm+ns=1	✓										
lcdm+run	✓	✓		✓	✓		✓			✓	✓
lcdm+run+tens	✓	✓		✓	✓		✓			✓	✓
lcdm+tau=0	✓										
lcdm+tens	✓	✓		✓	✓		✓			✓	✓
lcdm+xe1step	✓										
ocdm	✓	✓	✓			✓	✓	✓	✓		
ocdm+omegac=0	✓										
ocdm+omegal=0	✓										
ocdm+w											✓
pkrec	✓										
wcdm+mnu											✓
wcdm+nopert	✓	✓					✓	✓	✓		✓
wcdm+pert	✓	✓					✓	✓	✓		✓

Table 2.1: Combinations model/dataset for which the cosmological parameters have been evaluated. The various models and data sets are briefly described in Table 2.2 and Table 2.3 respectively.

Model	Description
lcdm	ΛCDM
lcdm+kcutlin	ΛCDM + primordial spectrum with sharp cutoff and linear prior
lcdm+kcutlog	ΛCDM + primordial spectrum with sharp cutoff and log prior
lcdm+mnu	ΛCDM + massive neutrinos
lcdm+mnu+nrel	ΛCDM + massive neutrinos + number of relativistic species
lcdm+nrel	ΛCDM + number of relativistic species
lcdm+ns=1	ΛCDM + scale invariant fluctuations ($n_s = 1$)
lcdm+run	ΛCDM + running scalar spectral index
lcdm+run+tens	ΛCDM + running spectral index + Tensor Modes
lcdm+tau=0	ΛCDM + no reionization ($\tau = 0$)
lcdm+tens	ΛCDM + Tensor Modes
lcdm+xe1step	ΛCDM + step reionization
ocdm	Open CDM
ocdm+omegac=0	Open CDM + No Dark Matter ($\Omega_c = 0$, $\Omega_\Lambda \neq 0$)
ocdm+omegal=0	Open CDM + No Cosmological Constant ($\Omega_c \neq 0$, $\Omega_\Lambda = 0$)
ocdm+w	Open CDM + w, ($w = constant$)
pkrec	primordial spectrum freely varying in 15 bins in k space
wcdm+mnu	wCDM + massive neutrinos, ($w = constant$)
wcdm+nopert	wCDM + no perturbtaions, ($w = constant$)
wcdm+pert	wCDM + perturbations, ($w = constant$)

Table 2.2: Description of the cosmological models listed in Table: 2.1

Data Set	Description
wmap	WMAP 3 year data set
2df	2dF Galaxy Redshift Survey [Cole et al., 2005]
bao	Baryonic Acoustic Oscillations [Eisenstein et al., 2005]
boom+acbar	BOOMERanG + ACBAR [Montroy et al., 2005],[Kuo et al., 2004]
cbi+vsa	CBI + VSA [Readhead et al., 2004],[Dickinson et al., 2004]
hst	Hubble Space Telescope Key Project [Freedman et al., 2001]
sdss	Sloan Digital Sky Survey, [Tegmark et al., 2004], [Eisenstein et al., 2005]
sn astier	Supernova Legacy Survey (SNLS) [Astier et al., 2005]
sn gold	Supernova "Gold Sample"[Riess et al., 2004]
wl	Weak Lensing [Semboloni et al., 2005, Hoekstra et al., 2005]
all	All data sets combined, excluding wl, hst and bao

Table 2.3: Description of the Data sets listed in Table: 2.1

2.1.4 Likelihood Code

Format FORTRAN 90
# of Files 1

Proper assignment of errors to points in the CMB angular power spectra requires the use of a Fisher matrix. Since some components that go into making the Fisher matrix are model dependent, we provide `FORTRAN 90` code which, given an input CMB model power spectrum, will compute the likelihood of that model fit to *WMAP* data and optionally return the inverse Fisher matrix.

More details can be found in:

G. Hinshaw, D. N. Spergel, L. Verde, R. S. Hill, S. S. Meyer, C. Barnes, C. L. Bennett, M. Halpern, N. Jarosik, A. Kogut, E. Komatsu, M. Limon, L. Page, G. S. Tucker, J. L. Weiland, E. Wollack, and E. L. Wright. First-Year Wilkinson Microwave Anisotropy Probe (WMAP) Observations: The Angular Power Spectrum. *ApJS*, 148:135–159, September 2003b

L. Verde, H. V. Peiris, D. N. Spergel, M. R. Nolta, C. L. Bennett, M. Halpern, G. Hinshaw, N. Jarosik, A. Kogut, M. Limon, S. S. Meyer, L. Page, G. S. Tucker, E. Wollack, and E. L. Wright. First-Year Wilkinson Microwave Anisotropy Probe (WMAP) Observations: Parameter Estimation Methodology. *ApJS*, 148:195–211, 2003

2.2 Full Resolution Coadded 3 Year Sky Maps

2.2.1 I, Q, U Maps (Individual DAs)

Coord System	Galactic
Projection Type	HEALPix Nested
Res/N_{side}	9/512
N_{pix}	3145728
Resolution	$0.23° - 0.93°$ (frequency dependent)
Units	mK (Thermodynamic)
Format	FITS
# of Files	10

Iterative algorithms are used to create skymaps from the calibrated differential time-ordered *WMAP* data for each of the ten differencing assemblies. Each pixel in a map represents a sky temperature for the bandpass appropriate to the differencing assembly. The CMB dipole has been removed and the zero point of each map has been set using a Galactic $csc(|b|)$ model (see Bennett et al. [2003c]).

The data provided in each map consist of four fields for each pixel:

- Intensity temperature, in mK

- Q Polarization temperature, in mK

- U Polarization temperature, in mK

- Effective number of observations, N_{obs}

Pixel noise can be evaluated from N_{obs} via $\sigma = \sigma_\circ / \sqrt{N_{obs}}$, where $\sigma_\circ$ for each differencing assembly is listed in the following table:

DA	$\sigma_\circ^I$ [mK]	$\sigma_\circ^{QU}$ [mK]	DA	$\sigma_\circ^I$ [mK]	$\sigma_\circ^{QU}$ [mK]
K1	1.4391	1.4551	V2	2.9458	2.9696
Ka1	1.4391	1.4831	W1	5.8833	5.9179
Q1	2.2449	2.2693	W2	6.5324	6.5707
Q2	2.1347	2.1563	W3	6.8849	6.9246
V1	3.3040	3.3305	W4	6.7441	6.7803

More details can be found in:

> N. Jarosik, C. Barnes, M. R. Greason, R. S. Hill, M. R. Nolta, N. Odegard, J. L. Weiland, R. Bean, C. L. Bennett, O. Dore, M. Halpern, G. Hinshaw, A. Kogut, E. Komatsu, M. Limon, S. S. Meyer, L. Page, D. N. Spergel, G. S. Tucker, E. Wollack, and E. L. Wright. Three-Year Wilkinson Microwave Anisotropy Probe (WMAP) Observations: Beam Profiles, Data Processing, Radiometer Characterization and Systematic Error Limits. *ApJ, submitted*, 2006

2.2.2 I-Only Maps (Individual DAs)

Coord System	Galactic
Projection Type	HEALPix Nested
Res/N$_{side}$	9/512
N$_{pix}$	3145728
Resolution	$0.23° − 0.93°$ (frequency dependent)
Units	mK (Thermodynamic)
Format	FITS
# of Files	10

Iterative algorithms are used to create skymaps from the calibrated differential time-ordered *WMAP* data for each of the ten differencing assemblies. Each pixel in a map represents a sky temperature for the bandpass appropriate to the differencing assembly. The CMB dipole has been removed and the zero point of each map has been set using a Galactic csc($|b|$) model (see Bennett et al. [2003c]).

The data provided in each map consist of two fields for each pixel:

- Thermodynamic temperature, in mK

- Effective number of observations, N_{obs}

Pixel noise can be evaluated from N_{obs} via $\sigma = \sigma_\circ/\sqrt{N_{obs}}$, where $\sigma_\circ$ for each differencing assembly is listed in the following table:

DA	$\sigma_\circ^I$ [mK]	DA	$\sigma_\circ^I$ [mK]
K1	1.4391	V2	2.9458
Ka1	1.4391	W1	5.8833
Q1	2.2449	W2	6.5324
Q2	2.1347	W3	6.8849
V1	3.3040	W4	6.7441

More details can be found in:

> N. Jarosik, C. Barnes, M. R. Greason, R. S. Hill, M. R. Nolta, N. Odegard, J. L. Weiland, R. Bean, C. L. Bennett, O. Dore, M. Halpern, G. Hinshaw, A. Kogut, E. Komatsu, M. Limon, S. S. Meyer, L. Page, D. N. Spergel, G. S. Tucker, E. Wollack, and E. L. Wright. Three-Year Wilkinson Microwave Anisotropy Probe (WMAP) Observations: Beam Profiles, Data Processing, Radiometer Characterization and Systematic Error Limits. *ApJ, submitted*, 2006

> E. L. Wright, G. Hinshaw, and C. L. Bennett. Producing Megapixel Cosmic Microwave Background from Differential Radiometer Data. *ApJ*, 458:L53, February 1996

2.2.3   I, Q, U Maps (Per Frequency)

Coord System	Galactic
Projection Type	HEALPix Nested
Res/N$_{side}$	9/512
N$_{pix}$	3145728
Resolution	$0.23° - 0.93°$ (frequency dependent)
Units	mK (Thermodynamic)
Format	FITS
# of Files	5

Five maps, one for each of the five frequency bandpasses observed by *WMAP*. These frequency maps are derived from the individual differencing assembly maps.

For each pixel in a frequency map, noise weighting is used to compute the average temperature from the individual differencing assembly map values. Since there is only one differencing assembly for the K and Ka bandpasses, the K and Ka frequency maps are identical to the K1 and Ka1 differencing assembly maps. The Q map is the noise-weighted result from combining Q1 and Q2, V is derived from V1 and V2, and W is made from W1, W2, W3 and W4.

The data provided in each frequency map consist of four fields for each pixel:

- Thermodynamic temperature, in mK

- Q Polarization temperature, in mK

- U Polarization temperature, in mK

- Effective number of observations, N_{obs}

Pixel noise can be evaluated from N_{obs} via $\sigma = \sigma_\circ/\sqrt{N_{obs}}$, where $\sigma_\circ$ (in mK) for each frequency is listed in the following table:

DA	$\sigma_\circ^I$ [mK]	$\sigma_\circ^{QU}$ [mK]
K	1.4391	1.4551
Ka	1.4638	1.4831
Q	2.1898	2.2128
V	3.1249	3.1501
W	6.5112	6.5484

The values of $\sigma_\circ$ are calculated averaging together the values of the individual DAs

2.2.4 I-Only Maps (Per Frequency)

Coord System	Galactic
Projection Type	HEALPix Nested
Res/N$_{side}$	9/512
N$_{pix}$	3145728
Resolution	$0.23° - 0.93°$ (frequency dependent)
Units	mK (Thermodynamic)
Format	FITS
# of Files	5

Five maps, one for each of the five frequency bandpasses observed by *WMAP*. These frequency maps are derived from the individual differencing assembly maps.

For each pixel in a frequency map, noise weighting is used to compute the average temperature from the individual differencing assembly map values. Since there is only one differencing assembly for the K and Ka bandpasses, the K and Ka frequency maps are identical to the K1 and Ka1 differencing assembly maps. The Q map is the noise-weighted result from combining Q1 and Q2, V is derived from V1 and V2, and W is made from W1, W2, W3 and W4.

The data provided in each frequency map consist of two fields for each pixel:

- Thermodynamic temperature, in mK

- Effective number of observations, N_{obs}

Pixel noise can be evaluated from N_{obs} via $\sigma = \sigma_\circ / \sqrt{N_{obs}}$, where $\sigma_\circ$ (in mK) for each frequency is listed in the following table:

DA	$\sigma_\circ$ [mK]
K	1.4391
Ka	1.4638
Q	2.1898
V	3.1249
W	6.5112

2.2.5   Foreground-Reduced I, Q, U Maps (Individual DAs)

Coord System	Galactic
Projection Type	HEALPix Nested
Res/N$_{side}$	9/512
N$_{pix}$	3145728
Resolution	$0.23° - 0.93°$ (frequency dependent)
Units	mK (Thermodynamic)
Format	FITS
# of Files	8

The foreground reduced skymaps were produced by removing a foreground model from the "unreduced" maps using the Foreground Template Model discussed in Hinshaw et al. [2006], Page et al. [2006]. Briefly, synchrotron, free-free, and dust emission templates were modeled and then subtracted from the single year "unreduced" maps. The goal was to produce a set of maps with the foreground removed while retaining *WMAP*'s noise characteristics.

Because the K and Ka maps were used to produce the foreground models, only Q, V, and W band foreground reduced maps are available.

As with the "unreduced" maps, full three year maps were produced by performing a weighted, pixel-by-pixel, mean of the three single year maps; the N_{Obs} measurement was used to weight this mean. The N_{Obs} measurements were added together to produce the final, three year, N_{Obs} measurement.

The same foreground template model was used to produce foreground reduced high resolution (res 10) V and W maps.

The data provided in each frequency map consist of four fields for each pixel:

- Thermodynamic temperature, in mK

- Q Polarization temperature, in mK

- U Polarization temperature, in mK

- Effective number of observations, N_{obs}

2.2.6   Foreground-Reduced I, Q, U Maps (Per Frequency)

Coord System	Galactic
Projection Type	HEALPix Nested
Res/N$_{side}$	9/512
N$_{pix}$	3145728
Resolution	$0.23° - 0.93°$ (frequency dependent)
Units	mK (Thermodynamic)
Format	FITS
# of Files	3

The foreground reduced skymaps were produced by removing a foreground model from the "unreduced" maps using the Foreground Template Model discussed in Hinshaw et al. [2006], Page et al. [2006]. Briefly, synchrotron, free-free, and dust emission templates were modeled and then subtracted from the single year "unreduced" maps. The goal was to produce a set of maps with the foreground removed while retaining *WMAP*'s noise characteristics.

Because the K and Ka maps were used to produce the foreground models, only Q, V, and W band foreground reduced maps are available.

As with the "unreduced" maps, full three year maps were produced by performing a weighted, pixel-by-pixel, mean of the three single year maps; the N_{Obs} measurement was used to weight this mean. The N_{Obs} measurements were added together to produce the final, three year, N_{Obs} measurement.

The same foreground template model was used to produce foreground reduced high resolution (res 10) V and W maps.

The data provided in each frequency map consist of four fields for each pixel:

- Thermodynamic temperature, in mK

- Q Polarization temperature, in mK

- U Polarization temperature, in mK

- Effective number of observations, N_{obs}

2.2.7 Smoothed I Maps (Per Frequency)

Coord System	Galactic
Projection Type	HEALPix Nested
Res/N$_{side}$	9/512
N$_{pix}$	3145728
Resolution	1°
Units	mK (Thermodynamic)
Format	FITS
# of Files	5

These maps result from smoothing the I Maps (per frequency) to a common resolution of 1 degree. Smoothing is performed in Fourier space by transforming the map to a_{lm}'s, up to the Nyquist frequency of the map, applying a window function determined by the smoothing kernel, then transforming back to pixel space. The smoothing window function is computed from the ratio of the desired output 1 degree FWHM Gaussian window function and the beam window function appropriate to each *WMAP* frequency bandpass.

Note that the instrument noise and sky signal are correlated between neighboring pixels in these maps. These maps are not intended for use in CMB studies, but rather for cases such as foreground analysis where a common resolution among maps is useful.

Pixel temperatures are provided in thermodynamic units, in mK. Because of the difficulty in associating a noise with each pixel, the effective number of observations (N_{obs}) has been set to 1.0 for all pixels.

2.3 Full Resolution Individual Year Sky Maps

2.3.1 I, Q, U Maps (Individual DAs)

Coord System	Galactic
Projection Type	HEALPix Nested
Res/N$_{side}$	9/512
N$_{pix}$	3145728
Resolution	$0.23° - 0.93°$ (frequency dependent)
Units	mK (Thermodynamic)
Format	FITS
# of Files	10

Iterative algorithms are used to create skymaps from the calibrated differential time-ordered *WMAP* data for each of the ten differencing assemblies. Each pixel in a map represents a sky temperature for the bandpass appropriate to the differencing assembly. The CMB dipole has been removed and the zero point of each map has been set using a Galactic csc($|b|$) model (see Bennett et al. [2003c]).

The data provided in each map consist of two fields for each pixel:

- Thermodynamic temperature, in mK

- Effective number of observations, N_{obs}

Pixel noise can be evaluated from N_{obs} via $\sigma = \sigma_\circ / \sqrt{N_{obs}}$, where $\sigma_\circ$ for each differencing assembly is listed in the following table:

DA	$\sigma_\circ$ [mK]	DA	$\sigma_\circ$ [mK]
K1	1.42366	V2	2.93683
Ka1	1.44883	W1	5.85196
Q1	2.26677	W2	6.53276
Q2	2.15567	W3	6.88032
V1	3.28789	W4	6.72537

More details can be found in:

G. Hinshaw, C. Barnes, C. L. Bennett, M. R. Greason, M. Halpern, R. S. Hill, N. Jarosik, A. Kogut, M. Limon, S. S. Meyer, N. Odegard, L. Page, D. N. Spergel, G. S. Tucker, J. L. Weiland, E. Wollack, and E. L. Wright. First-Year Wilkinson Microwave Anisotropy Probe (WMAP) Observations: Data Processing Methods and Systematic Error Limits. *ApJS*, 148:63–95, September 2003a

E. L. Wright, G. Hinshaw, and C. L. Bennett. Producing Megapixel Cosmic Microwave Background from Differential Radiometer Data. *ApJ*, 458:L53, February 1996

2.3.2   I-Only Maps (Individual DAs)

Coord System	Galactic
Projection Type	HEALPix Nested
Res/N$_{side}$	9/512
N$_{pix}$	3145728
Resolution	$0.23° - 0.93°$ (frequency dependent)
Units	mK (Thermodynamic)
Format	FITS
# of Files	10

Iterative algorithms are used to create skymaps from the calibrated differential time-ordered *WMAP* data for each of the ten differencing assemblies. Each pixel in a map represents a sky temperature for the bandpass appropriate to the differencing assembly. The CMB dipole has been removed and the zero point of each map has been set using a Galactic csc($|b|$) model (see Bennett et al. [2003c]).

Single year Stokes I maps are HEALPix Res 10 (Nside 1024) for the V and W differencing assemblies are supplied to support high-l TT analysis.

The data provided in each map consist of two fields for each pixel:

- Thermodynamic temperature, in mK

- Effective number of observations, N_{obs}

Pixel noise can be evaluated from N_{obs} via $\sigma = \sigma_\circ / \sqrt{N_{obs}}$, where $\sigma_\circ$ for each differencing assembly is listed in the following table:

DA	$\sigma_\circ$ [mK]	DA	$\sigma_\circ$ [mK]
K1	1.42366	V2	2.93683
Ka1	1.44883	W1	5.85196
Q1	2.26677	W2	6.53276
Q2	2.15567	W3	6.88032
V1	3.28789	W4	6.72537

More details can be found in:

> G. Hinshaw, C. Barnes, C. L. Bennett, M. R. Greason, M. Halpern, R. S. Hill, N. Jarosik, A. Kogut, M. Limon, S. S. Meyer, N. Odegard, L. Page, D. N. Spergel, G. S. Tucker, J. L. Weiland, E. Wollack, and E. L. Wright. First-Year Wilkinson Microwave Anisotropy Probe (WMAP) Observations: Data Processing Methods and Systematic Error Limits. *ApJS*, 148:63–95, September 2003a

> E. L. Wright, G. Hinshaw, and C. L. Bennett. Producing Megapixel Cosmic Microwave Background from Differential Radiometer Data. *ApJ*, 458:L53, February 1996

2.3.3 Foreground Reduced I, Q, U Maps (Individual DAs)

Coord System	Galactic
Projection Type	HEALPix Nested
Res/N$_{side}$	9/512
N$_{pix}$	3145728
Resolution	$0.23° - 0.93°$ (frequency dependent)
Units	mK (Thermodynamic)
Format	FITS
# of Files	5

The foreground reduced skymaps were produced by removing a foreground model from the "unreduced" maps using the Foreground Template Model discussed in Hinshaw et al. [2006], Page et al. [2006]. Briefly, synchrotron, free-free, and dust emission templates were modeled and then subtracted from the single year "unreduced" maps. The goal was to produce a set of maps with the foreground removed while retaining *WMAP*'s noise characteristics.

Because the K and Ka maps were used to produce the foreground models, only Q, V, and W band foreground reduced maps are available.

As with the "unreduced" maps, full three year maps were produced by performing a weighted, pixel-by-pixel, mean of the three single year maps; the N_{Obs} measurement was used to weight this mean. The N_{Obs} measurements were added together to produce the final, three year, N_{Obs} measurement.

The same foreground template model was used to produce foreground reduced high resolution (res 10) V and W maps.

The data provided in each frequency map consist of four fields for each pixel:

- Thermodynamic temperature, in mK

- Q Polarization temperature, in mK

- U Polarization temperature, in mK

- Effective number of observations, N_{obs}

2.3.4 High Resolution I-Only Maps (Individual DAs)

Coord System	Galactic
Projection Type	HEALPix Nested
Res/N$_{side}$	10/1024
N$_{pix}$	12582912
Resolution	$0.23° - 0.93°$ (frequency dependent)
Units	mK (Thermodynamic)
Format	FITS
# of Files	18

Iterative algorithms are used to create skymaps from the calibrated differential time-ordered *WMAP* data for each of the ten differencing assemblies. Each pixel in a map represents a sky temperature for the bandpass appropriate to the differencing assembly. The CMB dipole has been removed and the zero point of each map has been set using a Galactic $\csc(|b|)$ model (see Bennett et al. [2003c]).

The data provided in each map consist of two fields for each pixel:

- Thermodynamic temperature, in mK

- Effective number of observations, N_{obs}

Pixel noise can be evaluated from N_{obs} via $\sigma = \sigma_\circ/\sqrt{N_{obs}}$, where $\sigma_\circ$ for each differencing assembly is listed in the following table:

DA	$\sigma_\circ$ [mK]	DA	$\sigma_\circ$ [mK]
K1	1.42366	V2	2.93683
Ka1	1.44883	W1	5.85196
Q1	2.26677	W2	6.53276
Q2	2.15567	W3	6.88032
V1	3.28789	W4	6.72537

More details can be found in:

G. Hinshaw, M. R Nolta, C. L. Bennett, R. Bean, O. Doré, M. R. Greason, M. Halpern, R. S. Hill, N. Jarosik, A. Kogut, E. Komatsu, M. Limon, N. Odegard, S. S. Meyer, L. Page, H. V. Peiris, D. N. Spergel, G. S. Tucker, L. Verde, J. L. Weiland, E. Wollack, and E. L. Wright. Three-Year Wilkinson Microwave Anisotropy Probe (WMAP) Observations: Temperature Results. *ApJ, submitted*, 2006

2.3.5 Foreground-Reduced High Resolution I-Only Maps (Individual DAs)

Coord System	Galactic
Projection Type	HEALPix Nested
Res/N$_{side}$	10/1024
N$_{pix}$	12582912
Resolution	$0.23° - 0.93°$ (frequency dependent)
Units	mK (Thermodynamic)
Format	FITS
# of Files	18

The foreground reduced skymaps were produced by removing a foreground model from the "unreduced" maps using the Foreground Template Model discussed in Hinshaw et al. [2006], Page et al. [2006]. Briefly, synchrotron, free-free, and dust emission templates were modeled and then subtracted from the single year "unreduced" maps. The goal was to produce a set of maps with the foreground removed while retaining *WMAP*'s noise characteristics.

Because the K and Ka maps were used to produce the foreground models, only Q, V, and W band foreground reduced maps are available.

As with the "unreduced" maps, full three year maps were produced by performing a weighted, pixel-by-pixel, mean of the three single year maps; the N_{Obs} measurement was used to weight this mean. The N_{Obs} measurements were added together to produce the final, three year, N_{Obs} measurement.

The same foreground template model was used to produce foreground reduced high resolution (res 10) V and W maps.

The data provided in each frequency map consist of four fields for each pixel:

- Thermodynamic temperature, in mK

- Q Polarization temperature, in mK

- U Polarization temperature, in mK

- Effective number of observations, N_{obs}

More details can be found in:

G. Hinshaw, M. R Nolta, C. L. Bennett, R. Bean, O. Doré, M. R. Greason, M. Halpern, R. S. Hill, N. Jarosik, A. Kogut, E. Komatsu, M. Limon, N. Odegard, S. S. Meyer, L. Page, H. V. Peiris, D. N. Spergel, G. S. Tucker, L. Verde, J. L. Weiland, E. Wollack, and E. L. Wright. Three-Year Wilkinson Microwave Anisotropy Probe (WMAP) Observations: Temperature Results. *ApJ, submitted*, 2006

2.4   Reduced Resolution Sky Maps

2.4.1   I, Q, U, S Single Year Coadded Maps(Individual DAs)

Coord System	Galactic
Projection Type	HEALPix Nested
Res/N$_{side}$	4/16
N$_{pix}$	3072
Resolution	$0.23° - 0.93°$ (frequency dependent)
Units	mK (Thermodynamic)
Format	FITS
# of Files	30

Maps for each differencing assembly were created for each single year of data, resulting in three maps for each of the ten D/A's. Weighted averages where performed to combine the single year maps into three year maps; these were then combined through another set of weighted averages to produce three year maps for each frequency band.

A new signal component was computed in the map-making process. This so-called spurious signal, or S, component consists of the apparent signal generated by differences in the two radiometers that comprise a differencing assembly; it is discussed in detail in Jarosik et al. [2006].

The maps for each differencing assembly were produced by degrading the normal resolution (res9) maps to res 4, using the processing mask to block out the Galactic plane; this was done to keep the noise characteristics of these pixels intact. The original map was then degraded to res 4 without masking; this second res 4 map was used to fill in the blocked pixels in the first map.

The data provided in each map consist of two fields for each pixel:

- Thermodynamic temperature, in mK

- Q Polarization temperature, in mK

- U Polarization temperature, in mK

- S Bandpass mismatch component,

- Effective number of observations, N_{obs}

2.4.2 I, Q, U, S Single Year Maps Inverse Covariance Matrices (Individual DAs)

Coord System	Galactic
Projection Type	HEALPix Nested
Res/N$_{side}$	4/16
N$_{pix}$	3072
Resolution	$0.23° - 0.93°$ (frequency dependent)
Units	mK (Thermodynamic)
Format	FITS
# of Files	30

Due to a combination of 1/f noise and observing strategy, the noise in the *WMAP* sky maps is correlated from pixel to pixel. This results in certain low-l modes on the sky being less well measured than others. This effect can be completely ignored for temperature analysis since the low-l signal-to-noise ratio is so high, and the effect is not important at high-l. However, it is very important for polarization analysis because the signal-to-noise ratio is so much lower.

The full pixel-to-pixel weight (inverse covariance, aka Ninv) matrix has been evaluated at low pixel resolution (res4, $N_{side} = 16$, $N_{pix} = 3072$). Usage of the inverse covariance matrices is described in Jarosik et al. [2006] and Page et al. [2006].

2.4.3 I, Q, U, S Three Year Coadded Maps (Per Frequency)

Coord System	Galactic
Projection Type	HEALPix Nested
Res/N$_{side}$	4/16
N$_{pix}$	3072
Resolution	$0.23° - 0.93°$ (frequency dependent)
Units	mK (Thermodynamic)
Format	FITS
# of Files	5

Maps for each differencing assembly were created for each single year of data, resulting in three maps for each of the ten D/A's. Weighted averages where performed to combine the single year maps into three year maps; these were then combined through another set of weighted averages to produce three year maps for each frequency band.

A new signal component was computed in the map-making process. This so-called spurious signal, or S, component consists of the apparent signal generated by differences in the two radiometers that comprise a differencing assembly; it is discussed in detail in Jarosik et al. [2006].

The maps for each differencing assembly were produced by degrading the normal resolution (res9) maps to res 4, using the processing mask to block out the Galactic plane; this was done to keep the noise characteristics of these pixels intact. The original map was then degraded to res 4 without masking; this second res 4 map was used to fill in the blocked pixels in the first map.

The data provided in each map consist of two fields for each pixel:

- Thermodynamic temperature, in mK

- Q Polarization temperature, in mK

- U Polarization temperature, in mK

- S Bandpass mismatch component,

- Effective number of observations, N_{obs}

2.4.4 I, Q, U, S Three Year Coadded Maps Inverse Covariance Matrices (Per Frequency)

Coord System	Galactic
Projection Type	HEALPix Nested
Res/N$_{side}$	4/16
N$_{pix}$	3072
Resolution	$0.23° - 0.93°$ (frequency dependent)
Units	mK (Thermodynamic)
Format	FITS
# of Files	5

Due to a combination of 1/f noise and observing strategy, the noise in the *WMAP* sky maps is correlated from pixel to pixel. This results in certain low-l modes on the sky being less well measured than others. This effect can be completely ignored for temperature analysis since the low-l signal-to-noise ratio is so high, and the effect is not important at high-l. However, it is very important for polarization analysis because the signal-to-noise ratio is so much lower.

The full pixel-to-pixel weight (inverse covariance, aka Ninv) matrix has been evaluated at low pixel resolution (res4, $N_{side} = 16$, $N_{pix} = 3072$). Usage of the inverse covariance matrices is described in Jarosik et al. [2006] and Page et al. [2006].

2.4.5 Q, U Foreground Reduced Three Year Maps (Q, V Bands Only)

Coord System	Galactic
Projection Type	HEALPix Nested
Res/N$_{side}$	4/16
N$_{pix}$	3072
Resolution	$0.23° - 0.93°$ (frequency dependent)
Units	mK (Thermodynamic)
Format	FITS
# of Files	3

These low resolution maps were created by degrading the foreground reduced res 9 single year individual D/A polarization maps to res 4 using the QQ, QU, and UU covariance matrices, omitting pixel-to-pixel covariance.

The inverse covariance matrices were corrected using the standard polarization mask to ignore covariance with pixels within the cut. These matrices were also corrected for the effects of compression and foreground cleaning by increasing the noise per observation by a few percent; the noise per observation has been applied to the matrices.

The data provided in each map consist of two fields for each pixel:

- Thermodynamic temperature, in mK

- Q Polarization temperature, in mK

- U Polarization temperature, in mK

- Effective number of observations, N_{obs}

2.4.6 Q, U Foreground Reduced Three Year Maps Inverse Covariance Matrices (Q, V Bands Only)

Coord System	Galactic
Projection Type	HEALPix Nested
Res/N$_{side}$	4/16
N$_{pix}$	3072
Resolution	$0.23° - 0.93°$ (frequency dependent)
Units	mK (Thermodynamic)
Format	FITS
# of Files	3

Due to a combination of 1/f noise and observing strategy, the noise in the *WMAP* sky maps is correlated from pixel to pixel. This results in certain low-l modes on the sky being less well measured than others. This effect can be completely ignored for temperature analysis since the low-l signal-to-noise ratio is so high, and the effect is not important at high-l. However, it is very important for polarization analysis because the signal-to-noise ratio is so much lower.

The full pixel-to-pixel weight (inverse covariance, aka N_{inv}) matrix has been evaluated at low pixel resolution (res4, $N_{side} = 16$, $N_{pix} = 3072$). Usage of the inverse covariance matrices is described in Jarosik et al. [2006] and Page et al. [2006].

2.5 Derived Foreground Products

2.5.1 Internal Linear Combination (ILC) Map

Coord System	Galactic
Projection Type	HEALPix Nested
Res/N$_{side}$	9/512
N$_{pix}$	3145728
Resolution	1°
Units	mK (Thermodynamic)
Format	FITS
# of Files	1

The Internal Linear Combination (ILC) map is formed from a weighted linear combination of 5 Smoothed I Maps in which the weights are chosen to maintain the CMB anisotropy signal while minimizing the Galactic foreground contribution. The weights are determined by minimizing the variance of the measured temperatures with the additional constraint that sum of the weights is equal to 1. To account for the spatial variation of the spectral indices of the various foreground components across the sky and in particular in the Galactic plane, the sky is divided into 12 regions: 11 regions within the inner Galactic plane and 1 covering the outer Galactic plane and high Galactic latitudes. The weights are calculated for each of the 12 regions and a full-sky ILC map is generated using the obtained coefficients after smoothing the region boundardies with a 1.5 degree kernel. As a final step, a 'bias' correction' based on Monte Carlo simulations is applied to to the ILC map.

On angular scales greater than ~ 10 degrees, we believe that the three-year ILC map provides a reliable estimate of the CMB signal, with negligible instrument noise, over the full sky. However, we caution that on smaller scales there is a significant structure in the bias correction map that is still uncertain. More details can be found in:

> G. Hinshaw, M. R Nolta, C. L. Bennett, R. Bean, O. Doré, M. R. Greason, M. Halpern, R. S. Hill, N. Jarosik, A. Kogut, E. Komatsu, M. Limon, N. Odegard, S. S. Meyer, L. Page, H. V. Peiris, D. N. Spergel, G. S. Tucker, L. Verde, J. L. Weiland, E. Wollack, and E. L. Wright. Three-Year Wilkinson Microwave Anisotropy Probe (WMAP) Observations: Temperature Results. *ApJ, submitted*, 2006

2.5.2 Point Source Catalog

Format   ASCII
# of Files 1

This is a catalog of 323 point sources detected in the *WMAP* sky maps independently from any previous surveys. The sources listed in the catalog were detected as $\geqslant 5\sigma$ peaks in *WMAP* maps that have been weighted by the square root of the number of observations and optimally filtered for point source detection. The position of each source is obtained by fitting a Gaussian profile plus a baseline to each detected peak. Of the 323 detected sources, 317 have one or more possible 5 GHz counterparts. Of the 6 sources with no 5 GHz identification, some are close to the detection threshold and may be spurious. The catalog lists the following parameters for each source:

Column	Parameter
1 – 2	Right Ascension and Declination (2000)
3 – 4	Galactic Longitude and Latitude
5 – 9	*WMAP* Flux (Jy)
10 – 14	Flux Error (Jy)
15	Catalog
16	Coordinate-based Identifier
17	*WMAP* DR1 Identification Number
18	Spectral Index
19	Spectral Index Error

More details can be found in:

G. Hinshaw, M. R Nolta, C. L. Bennett, R. Bean, O. Doré, M. R. Greason, M. Halpern, R. S. Hill, N. Jarosik, A. Kogut, E. Komatsu, M. Limon, N. Odegard, S. S. Meyer, L. Page, H. V. Peiris, D. N. Spergel, G. S. Tucker, L. Verde, J. L. Weiland, E. Wollack, and E. L. Wright. Three-Year Wilkinson Microwave Anisotropy Probe (WMAP) Observations: Temperature Results. *ApJ, submitted*, 2006

2.5.3 Foregrounds Derived from Maximum Entropy Method

This description applies to any of the three foregrounds recovered using the Maximum Entropy Method: synchrotron, free-free and dust.

Coord System	Galactic
Projection Type	HEALPix Nested
Res/N$_{side}$	8/256
N$_{pix}$	786432
Resolution	$1°$
Units	mK (Antenna)
Format	FITS
# of Files	5

The Maximum Entropy Method (MEM) is used to derive all-sky maps of the synchrotron, free-free and dust foregrounds at each of the 5 *WMAP* frequencies. Using the smoothed I maps minus the ILC map as input, representations of each of the foregrounds are fit to each pixel independently. The synchrotron spectrum is allowed to vary for each pixel, while the free-free and dust spectral indices are assumed to be constant over the sky. The MEM technique fits for the separate components by maximizing an entropy functional using the listed templates as priors:

Component	Prior
Synchrotron	408 GHz Haslam Map
Free-Free	Hα Map
Dust	FDS Map

The three model foregrounds are provided in separate files for each of the five *WMAP* frequencies. Note that the model temperatures are in mK, antenna temperature, rather than in thermodynamic units.

More details can be found in:

G. Hinshaw, M. R Nolta, C. L. Bennett, R. Bean, O. Doré, M. R. Greason, M. Halpern, R. S. Hill, N. Jarosik, A. Kogut, E. Komatsu, M. Limon, N. Odegard, S. S. Meyer, L. Page, H. V. Peiris, D. N. Spergel, G. S. Tucker, L. Verde, J. L. Weiland, E. Wollack, and E. L. Wright. Three-Year Wilkinson Microwave Anisotropy Probe (WMAP) Observations: Temperature Results. *ApJ, submitted*, 2006

2.5.4   Foregrounds Templates

Coord System	Galactic
Projection Type	HEALPix Nested
Res/N$_{side}$	9/512 or 4/16
N$_{pix}$	786432 or 3072
Resolution	$1°$
Units	mK (Antenna)
Format	FITS
# of Files	3

For most cosmological analyses one must retain the well-defined noise characteristics of the *WMAP* frequency band maps. To achieve this, low-noise model templates for each foreground emission component (dust, free-free, and synchrotron) were created and fit to the maps at each frequency band; these fits were then subtracted from the skymaps. Regions that could not be reliably cleaned were masked, and thereby essentially discarded from later analysis.

The dust emission templates were created from "Model 8" from the Finkbeiner et al. [1999] (FDS 1999) analysis of IRAS and COBE data. The FDS 94GHz map was used as the dust emission template for Stokes I/temperature analysis and can be found on LAMBDA. A separate dust template was developed for Q and U polarization analysis, combining information from the FDS intensity map and starlight polarization maps. This latter template is stored in a standard HEALpix FITS map file with the Q and U templates stored in the Q_POLARISATION and U_POLARISATION columns of the first binary table extension; the TEMPERATURE and N_OBS columns of this extention are set to zero and one, respectively.

The free-free emission template was developed from the full-sky Hα map compiled by Finkbeiner [2003] with a correction for dust extinction [Bennett et al., 2003a].

The synchrotron template used for temperature analysis was computed from the difference of the *WMAP* K and Ka Stokes I maps in thermodynamic units, using the maps smoothed to $1°$ resolution. The procedure for creating the template is described in detail in Hinshaw et al. [2006]. K band data was used for the polarized synchrotron emission template as described by citetpage/etal:prep.

N. Jarosik, C. Barnes, M. R. Greason, R. S. Hill, M. R. Nolta, N. Odegard, J. L. Weiland, R. Bean, C. L. Bennett, O. Dore, M. Halpern, G. Hinshaw, A. Kogut, E. Komatsu, M. Limon, S. S. Meyer, L. Page, D. N. Spergel, G. S. Tucker, E. Wollack, and E. L. Wright. Three-Year Wilkinson Microwave Anisotropy Probe (WMAP) Observations: Beam Profiles, Data Processing, Radiometer Characterization and Systematic Error Limits. *ApJ, submitted*, 2006

G. Hinshaw, M. R Nolta, C. L. Bennett, R. Bean, O. Doré, M. R. Greason, M. Halpern, R. S. Hill, N. Jarosik, A. Kogut, E. Komatsu, M. Limon, N. Odegard, S. S. Meyer, L. Page, H. V. Peiris, D. N. Spergel, G. S. Tucker, L. Verde, J. L. Weiland, E. Wollack, and E. L. Wright. Three-Year Wilkinson Microwave

Anisotropy Probe (WMAP) Observations: Temperature Results. *ApJ, submitted*, 2006

L. Page, G. Hinshaw, E. Komatsu, M. R. Nolta, D. N. Spergel, C. L. Bennett, C. Barnes, R. Bean, O. Doré, M. Halpern, R. S. Hill, N. Jarosik, A. Kogut, M. Limon, S. S. Meyer, N. Odegard, H. V. Peiris, G. S. Tucker, L. Verde, J. L. Weiland, E. Wollack, and E. L. Wright. Three-Year Wilkinson Microwave Anisotropy Probe (WMAP) Observations: Polarization Analysis. *ApJ, submitted*, 2006

D. N. Spergel, R. Bean, O. Doré, M. R. Nolta, C. L. Bennett, G. Hinshaw, N. Jarosik, E. Komatsu, L. Page, H. V. Peiris, L. Verde, C. Barnes, M. Halpern, R. S. Hill, A. Kogut, M. Limon, S. S. Meyer, N. Odegard, G. S. Tucker, J. L. Weiland, E. Wollack, and E. L. Wright. Three-Year Wilkinson Microwave Anisotropy Probe (WMAP) Observations: Cosmological Parameters. *ApJ, submitted*, 2006

C. L. Bennett, M. Bay, M. Halpern, G. Hinshaw, C. Jackson, N. Jarosik, A. Kogut, M. Limon, S. S. Meyer, L. Page, D. N. Spergel, G. S. Tucker, D. T. Wilkinson, E. Wollack, and E. L. Wright. The Microwave Anisotropy Probe Mission. *ApJ*, 583:1–23, January 2003a

D. P. Finkbeiner. H-alpha Map. *ApJS*, 2003. accepted (astro-ph/0301558)

D. P. Finkbeiner, M. Davis, and D. J. Schlegel. Extrapolation of Galactic Dust Emission at 100 microns to CMBR Frequencies Using FIRAS. *ApJ*, 524:867, 1999

2.6 Ancillary Data

2.6.1 Masks

Coord System	Galactic
Projection Type	HEALPix Nested
Res/N$_{side}$	9/512
N$_{pix}$	3145728
Resolution	N/A
Units	N/A
Format	FITS
# of Files	3

A number of *WMAP* data analysis applications have been aided by the use of pixel intensity masks which exclude "bright" portions of the sky from use. These masks were used in the generation of maps and CMB angular power spectra. The 3 masks provided allow for the selective exclusion of portions of the sky at different flux levels. The masks are based on the K-band map and include a 0.6 degree radius exclusion area around known point sources.

Mask	% of pix cut	Description
Kp0 Intensity	23.5	Exclusion mask used for data analysis
Kp2 Intensity	15.3	Exclusion mask used for data analysis
Processing	5.7	Exclusion mask used in mapmaking
Source Only	2.4	Non-Galactic sources in the Processing mask
Polarization	26.5	Exclusion mask used in polarization analysis
Polarization Source Only	0.2	Non-Galactic sources in the Polarization mask

Mask values for each map pixel are provided in the N_{obs} field of the data file (the 'Temperature' field is set to zero for all pixels and not used). A mask value of zero means that the pixel is excluded; a value of 1 means that the pixel is accepted.

More details can be found in:

> L. Page, G. Hinshaw, E. Komatsu, M. R. Nolta, D. N. Spergel, C. L. Bennett, C. Barnes, R. Bean, O. Doré, M. Halpern, R. S. Hill, N. Jarosik, A. Kogut, M. Limon, S. S. Meyer, N. Odegard, H. V. Peiris, G. S. Tucker, L. Verde, J. L. Weiland, E. Wollack, and E. L. Wright. Three-Year Wilkinson Microwave Anisotropy Probe (WMAP) Observations: Polarization Analysis. *ApJ, submitted*, 2006

> G. Hinshaw, M. R Nolta, C. L. Bennett, R. Bean, O. Doré, M. R. Greason, M. Halpern, R. S. Hill, N. Jarosik, A. Kogut, E. Komatsu, M. Limon, N. Odegard, S. S. Meyer, L. Page, H. V. Peiris, D. N. Spergel, G. S. Tucker, L. Verde, J. L. Weiland, E. Wollack, and E. L. Wright. Three-Year Wilkinson Microwave Anisotropy Probe (WMAP) Observations: Temperature Results. *ApJ, submitted*, 2006

2.6.2   Beam Transfer Functions

Units   see text
Format   ASCII
# of Files   10

Beam transfer functions are computed from the Legendre transform of the Hermite polynomial fit to the hybrid radial beam profile. The window function applicable to power spectra is the square of the beam transfer function.

Window functions are presented as ASCII tables, with the first column being multipole moment ℓ and the second column the transfer function (amplitude) normalized to 1.0 at $\ell = 1$.

More details can be found in:

> N. Jarosik, C. Barnes, M. R. Greason, R. S. Hill, M. R. Nolta, N. Odegard, J. L. Weiland, R. Bean, C. L. Bennett, O. Dore, M. Halpern, G. Hinshaw, A. Kogut, E. Komatsu, M. Limon, S. S. Meyer, L. Page, D. N. Spergel, G. S. Tucker, E. Wollack, and E. L. Wright. Three-Year Wilkinson Microwave Anisotropy Probe (WMAP) Observations: Beam Profiles, Data Processing, Radiometer Characterization and Systematic Error Limits. *ApJ, submitted*, 2006

> G. Hinshaw, M. R Nolta, C. L. Bennett, R. Bean, O. Doré, M. R. Greason, M. Halpern, R. S. Hill, N. Jarosik, A. Kogut, E. Komatsu, M. Limon, N. Odegard, S. S. Meyer, L. Page, H. V. Peiris, D. N. Spergel, G. S. Tucker, L. Verde, J. L. Weiland, E. Wollack, and E. L. Wright. Three-Year Wilkinson Microwave Anisotropy Probe (WMAP) Observations: Temperature Results. *ApJ, submitted*, 2006

2.6.3 Beam Maps

Coord System	Focal Plane
Projection Type	Rectilinear, pixelized at $2.4'(0.04°)$
Resolution	$0.23° - 0.93°$ (frequency dependent)
Units	mK (Thermodynamic)
Format	FITS
# of Files	10

The main and near-sidelobe response of each of the 20 WMAP antenna feeds has been mapped in-flight using observations of Jupiter. The 3-year release is comprised of 6 Jupiter observing seasons: Oct/Nov 2001, Feb/Mar 2002, Nov/Dec 2002, Mar/Apr 2003, Dec 2003/Jan 2004, and Apr/May 2004. As a prelude to beam analysis, an archive of calibrated time-ordered observations is constructed, consisting of Jupiter passages within roughly 9.0, 6.5, 5.0, 2.5 and 2.5 degrees of either the A- or B-side beam center for K, Ka, Q, V and W bands respectively. The time-ordered observations are corrected to a fiducial Jupiter distance of 5.2 AU, background subtracted and corrected for aberration. To constrain low signal-to-noise beam pedestals, a hybrid TOD archive is then constructed in which model predictions [Jarosik et al., 2006] are substituted for data at the 17,17,18,19 and 20 dBi levels of K,Ka,Q,V and W respectively. This hybrid beam archive serves as the basis for beam map and window function analysis.

For purposes of constructing beam maps, the data in the hybrid beam TOD archive are assigned to 2.4 arcminute bins on a coordinate grid centered on either the A or B-side focal plane axis. The beam response for each feed is computed from the average temperature in each bin. No correction has been made for the side-A vs. side-B input transmission imbalance.

Beam maps are provided in 10 FITS image format files, one file for each differencing assembly. Each file contains:

- Beam map for the A side, in mK (antenna temperature)

- Statistical errors of each bin of the A and B sides beam maps, in mK (antenna temperature). The statistical error are based on the number of observations in each bin.

- Beam map for the B side, in mK (antenna temperature)

- Statistical errors of each bin of the A and B sides beam maps, in mK (antenna temperature)

The beam coordinates form an equal area rectangular coordinate system centered on the optic axis of the spacecraft. They are related to coordinates θ (elevation from optic axis) and ϕ (azimuth about optic axis) as follows:

$$X_{beam} = 2\sin(\theta/2)\cos(\phi)$$

$$Y_{beam} = 2\sin(\theta/2)\sin(\phi).$$

More details can be found in:

N. Jarosik, C. Barnes, M. R. Greason, R. S. Hill, M. R. Nolta, N. Odegard, J. L. Weiland, R. Bean, C. L. Bennett, O. Dore, M. Halpern, G. Hinshaw, A. Kogut, E. Komatsu, M. Limon, S. S. Meyer, L. Page, D. N. Spergel, G. S. Tucker, E. Wollack, and E. L. Wright. Three-Year Wilkinson Microwave Anisotropy Probe (WMAP) Observations: Beam Profiles, Data Processing, Radiometer Characterization and Systematic Error Limits. *ApJ, submitted*, 2006

2.6.4   Beam Radial Profiles

Units   see text
Format   ASCII
# of Files   10

For each differencing assembly, a symmetrized radial beam profile is computed by fitting the ensemble of individual A- and B-side Jupiter observations with Hermite polynomials of even order.

The polynomial fits to the data are tabulated in 0.5 arcminute increments, increasing outwards from beam center (radius=0.0) to the cutoff radius chosen for the window function determination. The profiles are normalized to 1.0 at $r = 0$.

2.6.5   Far-Sidelobe Maps

Coord System	Spacecraft
Projection Type	HEALPix Nested
Res/N$_{side}$	7/128
N$_{pix}$	196608
Resolution	N/A
Units	[-]
Format	FITS
# of Files	10

Low resolution (res 7) maps of the antenna gain response over 4π steradians for each of the 10 *WMAP* detector assemblies. While *WMAP*'s optical system gain drops very rapidly when moving away from the main beam line-of-sight, the emission of the extended Galactic foreground can be 1000 times brighter than the fluctuations of the CMB and can cover very large solid angles. It is therefore extremely important to fully characterize the antenna gain response. The Far-Sidelobe Maps are based on compilations of data from the following sources:

- GSFC anechoic chamber antenna range

- Princeton outdoor antenna range

- In flight lunar data

- Physical optics code theoretical predictions

The gain pattern is presented in spacecraft coordinates, such that the X axis is parallel to the plane of the radiators, -Z is the anti-sun direction of the spin axis, and Y is perpendicular to both. The gain, $4\pi/\Omega^S$, is relative to isotropic in dimensionless units where Ω^S is the symmetrized beam solid angle. Positive values refer to A-side pickup, and negative values to B-side pickup.

These maps are in units of directive gain, g_i, where i is a pixel; these are the linear units that correspond to dBi. The normalization is such that $\sum_i(|g_i|) = 2N_{pix}$, or it would equal $2N_{pix}$ if the full antenna pattern were represented rather than being cut off at the radius chosen to define the main beam/far-sidelobe boundary.

More details can be found in:

> C. Barnes, R. S. Hill, G. Hinshaw, L. Page, C. L. Bennett, M. Halpern, N. Jarosik, A. Kogut, M. Limon, S. S. Meyer, G. S. Tucker, E. Wollack, and E. L. Wright. First-Year Wilkinson Microwave Anisotropy Probe (WMAP) Observations: Galactic Signal Contamination from Sidelobe Pickup. *ApJS*, 148:51–62, September 2003

Chapter 3

Time Ordered Data (TOD)

Three complete time-ordered data archives are supplied with the latest *WMAP* data release; two of these archives contain calibrated data while the second contains uncalibrated (or raw) data.

Archive	# of Files	Size
Calibrated	55	63.1 GB
Uncalibrated	55	94.7 GB
Filtered Calibrated	55	95.3 GB

The uncalibrated archive contains all four radiometer channels for each observation; the calibrated archives have been coadded into two radiometer channels to reduce their size. The first calibrated archive has had an hourly baseline removed as part of the calibration process; the second has had a prewhitening filter applied to the data during calibration.

WMAP's Telemetry data consists of many packet types; each packet type contains several measurements with some sort of common theme. Once on the ground and delivered to the data analysis facility, these packets are sorted and a subset are combined into records spanning 46.08 seconds; these records comprise the time-ordered data (TOD) archive. This archive is maintained in a collection of files, each spanning one day of data.

The TOD archive is distributed to the public through daily files written using the Flexible Image Transport Standard (FITS) format. Each file is broken up into a collection of five binary FITS tables:

1. Meta Data Table

2. Science Data Table

3. Analog Instrument Housekeeping Data Table

4. Digital Instrument Housekeeping Data Table

5. Line-Of-Sight Data Table

In four of the five tables, each row has a time associated with it. This time is reported in a modified reduced Julian day format. Packet times require precision to better than one tenth of a millisecond, so in order to retain sufficient precision in the numerical representation of the time, it is necessary to modify the definition of the reduced Julian day. To convert a modified reduced Julian day to a Julian day, add 2,450,000 to its value.

A discussion of each table, followed by a very brief discussion of FITS headers, follows. In these discussions, records refer to TOD records and packets refer to the telemetry packets received from *WMAP*. The science data is transmitted in two packets; these are combined into a single data structure called major science frames.

3.1 The Meta Data Table

The meta data table contains general information describing each record in the time ordered data archive for that day. Each row corresponds to one 46.08 second record; each column represents:

Name	Description
TIME	The time of the start of the record, represented as a modified reduced Julian day.
POSITION	A three element Cartesian vector supplying the position (in kilometers) of *WMAP* at the start of the record. It is measured from the Sun with the +X axis in the J2000 0hr right ascension direction and the +Z axis in the J2000 +90deg. declination direction.
VELOCITY	A three element Cartesian vector supplying the velocity (in km/sec) of *WMAP* at the start of the record, using the same coordinate system as the POSITION vector.
GEOPOS	A three element Cartesian vector supplying the position (in kilometers) of *WMAP* at the start of the record. It is measured in the same coordinate system as the POSITION vector, centered on the Earth instead of the Sun.
GEOVEL	A three element Cartesian vector supplying the velocity (in km/sec) of *WMAP* at the start of the record, using the same coordinate system as the GEOPOS vector.
QUATERN	A 4×33 array containing a four element quaternion for the start of each major science frame plus one for the preceding science frame and one for each of the two following science frames.
NSCI	The number of major science frames in the record. There will generally be thirty [the maximum number of frames allowed in a record].
NDIHK	The number of digital instrument housekeeping packets there are in the record.

3.2 The Science Data Table

The science data table contains the major science frames recorded for that day. Each frame consists of two science data telemetry packets that have been combined into a single data structure.

A single TOD record contains thirty 1.536 second major science frames. The data has been calibrated and are reported in millikelvin. Each row corresponds to one frame; each column represents:

Name	Description
TIME	The time of the start of the science frame, represented as a modified reduced Julian day.
K1	The K-band differencing assembly array.
KA1	The KA-band differencing assembly array.
Q1	The first Q-band differencing assembly array.
Q2	The second Q-band differencing assembly array.
V1	The first V-band differencing assembly array.
V2	The second V-band differencing assembly array.
W1	The first W-band differencing assembly array.
W2	The second W-band differencing assembly array.
W3	The third W-band differencing assembly array.
W4	The fourth W-band differencing assembly array.
GenFlags	A set of bit-coded quality flags describing the entire science frame [the general flags].
DAFlags	An array of ten sets of bit-coded quality flags, each describing one differencing assembly.
Error1	A two bit-coded error code transmitted by *WMAP* describing the science frame. There are two—one for each science telemetry packet.
Error2	A bit-coded error code transmitted by *WMAP* describing the science frame. There are two—one for each science telemetry packet.
FrmInd	The index within the day of the time-ordered data record containing this science frame.
SciInd	The index of the science frame within its time-ordered data record.

Each differencing assembly (DA) array consists of four channels measured N times where N depends upon the bandpass. For the first data release, however polarization data are not available and the four channels are averaged together,[1] so each differencing assembly array consists of N observations for each DA per channel per major science frame. N for each

---

[1] The IDL procedure `pckt2mnemonic` (see section 4.2) provided with the *WMAP* software package is designed to be compatible with future data releases and will accept as input any of the four channels but will always return the same average value.

bandpass is:

K	Ka	Q	V	W
12	12	15	20	30

For the three-year data release the calibrated TOD include polarization data as two separate polarization vectors. The average polarization estimate for the detectors is reported. For the uncalibrated data all four detector channels are provided. The bit-coded quality flags are set during processing. These flags are:

General Flags

Bit 0   There is a problem with the spacecraft attitude for this science frame.

Bit 1   A filler telemetry packet (science, instrument, or spacecraft) affects this science frame. A filler packet is an empty frame that replaces a missing packet.

Bit 2   The transmitter is on. Since the transmitter is now always on this flag will not be implemented.

Bit 3   *WMAP* is not in observing mode.

Bit 4   There is no science data in this frame. Not implemented.

Bit 5   The sun is visible over the sun shield. In other words, the angle between the sun and the +Z axis is greater than some angle (see programs.pars for the shield angle).

Bit 6   The Earth is visible over the sun shield. In other words, the angle between the Earth and the +Z axis is greater than some angle (see programs.pars for the shield angle).

Bit 7   The moon is visible over the sun shield. In other words, the angle between the moon and the +Z axis is greater than some angle (see programs.pars for the shield angle).

DA Specific Flags

Bit 0   This flag indicates that the data in the frame is suspect. An ASCII log file is used to flag time ranges that contain suspect data.

Bit 1   Mars is visible in the A-side beam.

Bit 2   Mars is visible in the B-side beam.

Bit 3   Jupiter is visible in the A-side beam.

Bit 4   Jupiter is visible in the B-side beam.

Bit 5   Saturn is visible in the A-side beam.

Bit 6   Saturn is visible in the B-side beam.

Bit 7   Uranus is visible in the A-side beam.

Bit 8   Uranus is visible in the B-side beam.
Bit 9   Neptune is visible in the A-side beam.
Bit 10   Neptune is visible in the B-side beam.

Finally, the bit-coded error codes in the science telemetry packets shown below are extracted from the internal *WMAP* document: "*MAP* DEU Flight Command and Telemetry Packets Definition," by Carlos Trujillo of NASA/GSFC.

Error 1

Bit 0   Unused.
Bit 1   Band Buffer Overflow. The memory location where the pointer to the next available storage location inside the Band buffer has been corrupted. In order to avoid writing science data outside the boundaries of the Band buffer, this check is performed prior to storage of the next 40 science data samples into the Band buffer. A detected overflow condition is handled by not storing science data into the Band buffer. Correction of this error is done during science data packetization (the pointer value is cleared as part of cleaning operations).
Bit 2   K Band Accumulation Buffer Overflow. The memory location where the pointer to the next available storage location for the K Band Accumulation buffer has been corrupted. In order to avoid writing science data outside the boundaries of this buffer, this check is performed prior to calculation of the next K Band accumulated result. If the overflow condition is detected, accumulation data will not be processed nor stored.
Bit 3   Ka Band Accumulation Buffer Overflow. The memory location where the pointer to the next available storage location for the Ka Band Accumulation buffer has been corrupted. In order to avoid writing science data outside the boundaries of this buffer, this check is performed prior to calculation of the next Ka Band accumulated result. If the overflow condition is detected, accumulation data will not be processed nor stored.

Bit 4   Q Band Accumulation Buffer Overflow. The memory location where the pointer to the next available storage location for the Q Band Accumulation buffer has been corrupted. In order to avoid writing science data outside the boundaries of this buffer, this check is performed prior to calculation of the next Q Band accumulated result. If the overflow condition is detected, accumulation data will not be processed nor stored.

Bit 5   V Band Accumulation Buffer Overflow. The memory location where the pointer to the next available storage location for the V Band Accumulation buffer has been corrupted. In order to avoid writing science data outside the boundaries of this buffer, this check is performed prior to calculation of the next V Band accumulated result. If the overflow condition is detected, accumulation data will not be processed nor stored.

Bit 6   W Band Accumulation Buffer Overflow. The memory location where the pointer to the next available storage location for the W Band Accumulation buffer has been corrupted. In order to avoid writing science data outside the boundaries of this buffer, this check is performed prior to calculation of the next W Band accumulated result. If the overflow condition is detected, accumulation data will not be processed nor stored.

Bit 7   Science Pointers Out of Spec - The values for all the storage and retrieval pointers for Band and Accumulation buffers are examined at the end of each Science Data Cycle. The FSW can be fooled into believing that a Science Data Cycle ended (corruption of Timing.SciDataCycles counter) and attempt an early packetization of the science data. This attempt will be accepted, but the condition is flagged. Clearing all science data cycle counters and pointers (therefore correcting any corrupted memory locations) recovers from this error.

Error 2

Bits 1–15   Non-matching channel address counter - For each science data sample collected from the AEU the actual reported address of the sample (0 through 39) is verified against the address value requested by the FSW. Any non-matching address values will void the science data sample collected and a value of 0 will be stored in the expected Band buffer location.

3.3 The Analog Instrument Housekeeping (AIHK) Data Table

The AIHK data table contains the AIHK packets recorded for that day. This data represents physical measurements [such as temperatures, voltages, and currents] of the instrument indicating its current state.

A single TOD record contains one AIHK telemetry packet consisting of two 23.04 second sweeps. Each row in the table corresponds to one sweep; each column represents:

Name	Description
TIME	The time of the start of the telemetry packet, represented as a modified reduced Julian day. This time will be reported twice in the table—once for each sweep extracted from an AIHK packet.
PDU	The Power Distribution Unit (PDU) data block of 97 elements.
AEU1	The Analog Electronics Unit (AEU) #1 data block of 57 elements.
AEU2	The Analog Electronics Unit (AEU) #2 data block of 57 elements.
AWIN1	The 16 element window range block corresponding to AEU1.
AWIN2	The 16 element window range block corresponding to AEU2.
Counters	Five status counters. There is actually only one set of these counters in the telemetry packet; each sweep has a copy in its table row.
FrmInd	The index within the day of the time-ordered data record containing this science frame.
Sweep	The sweep within the telemetry packet represented by this row (1 or 2).

The two AEU data blocks contain 32 elements that require more dynamic range than a single two byte integer can provide. For each of these elements, a one byte window element is provided in the AWIN blocks that essentially adds another byte of dynamic range to those measurements.

3.4 The Digital Instrument Housekeeping (DIHK) Data Table

The DIHK data table contains the DIHK packets recorded for that day. This data primarily represents digital status information relating to commands received and current status codes. Physical measurements regarding the digital electronics unit are also transmitted through this packet.

A single TOD record contains four 11.52 second DIHK telemetry packets. A row in the table represents one packet; each column represents:

Name	Description
TIME	The time of the start of the telemetry packet, represented as a modified reduced Julian day.
Data	The DIHK data portion of the packet consisting of 42 elements.
FrmInd	The index within the day of the time-ordered data record containing this science frame.
DihkInd	The index of the DIHK packet within its time-ordered data record.

3.5 The Line-Of-Sight (LOS) Table

The LOS table provides unit vectors describing the line-of-sight for each microwave horn in spacecraft coordinates. The position and attitude data [attitude provided through the quaternions] may be used with these unit vectors to determine the pointing of *WMAP* at any given time.

This table consists of a single row of twenty columns. Each column contains a three element unit vector describing the pointing of a single differencing assembly horn on either the A or B side of the spacecraft. The column names are:

K1A   K1B   KA1A   KA1B   Q1A   Q1B   Q2A   Q2B   V1A   V1B
V2A   V2B   W1A   W1B   W2A   W2B   W3A   W3B   W4A   W4B

3.6 Headers

Each FITS header in the file contains the conversion constant used to transform the reduced Julian day into a standard Julian day; the header keyword is TIME2JD. The primary header also contains:

- The start (keyword STIME) and end (keyword ETIME) times of the data contained by the file in a GMT text format:
  YYYYDDDhhmmss
  where YYYY is the year, DDD is the day of the year, hhmmss is the GMT hour, minute, and second of the day.

- The data release date (keyword RELEASE) in the same GMT format.

- The number of TOD records (keyword NUMREC) is stored in the file.

Chapter 4

Software

The *WMAP* IDL®[1] library is a collection of IDL® procedures to assist with reading, manipulating and displaying the *WMAP* data products. The library can be downloaded at:

http://lambda.gsfc.nasa.gov

As described in Chapter 2 all the *WMAP* maps are pixelized using the HEALPix system. The HEALPix pixelization scheme, initially developed by K. Górski, B. Wandelt, and E. Hivon, is a hierarchical equal area isolatitude pixelisation of the sphere. More information and a suite of Fortran and IDL software tools for working with HEALPix format maps is available from the HEALPix web site at:

http://www.eso.org/science/healpix/

4.1   FITS Readers

4.1.1   FITS_READ_MAP

The FITS_READ_MAP routine reads any of *WMAP* maps data product (I maps, foreground maps, etc., except for map files counting polarization data – to read polarization data products use WMAP_READ_MAP available through the software page) into a R*4 array. See individual data products for details.

```
CALLING SEQUENCE:
   FITS_READ_Map, File_Name, T, N_obs, [ Header ]

INPUTS:
   File_Name - Character name of archive map FITS file, scalar string

OUTPUTS:
   T     - R*4 array with temperature of each pixel
   N_obs - R*4 array with number of observations of each pixel
```

---

[1]IDL®is a trademark of Research System, Inc., 4990 Pearl East Circle, Boulder, CO 80301: http://www.rsinc.com

```
OPTIONAL OUTPUT:
   Header - FITS header with map information

EXAMPLE: Read the W4 difference assembly map

IDL> fits_read_map,'map_w4_imap_yr1_v1.fits',t,N_obs,h
```

4.1.2 FITS_READ_TOD

Read a WMAP time-ordered data FITS file (e.g. `map_q_imap_yr1_v1.fits`) into an IDL® structure.

```
CALLING SEQUENCE:
   FITS_READ_TOD, file, arch, [/NOHK]

INPUTS:
   file - The name of the FITS file to read.

OUTPUTS:
   arch - The TOD data structure. See the function TOD_FORMAT()
          for additional information about this structure

OPTIONAL INPUT KEYWORD:
   /NOHK - if set, then no housekeeping information is returned, and
           only the time stamp and science data are defined in the
           output structure
EXAMPLE:
   Read the time-ordered data for day 221 of year 2002 into an output
   structure named arch

   IDL>  file ='MAP_tod_20022202357_20022212357.fits'
   IDL>  FITS_READ_TOD, file, arch
```

4.2 Pckt2Mnemonic()

This is a procedure to extract data for a given mnemonic from a packet in the time-ordered data (include both digital and analog housekeeping data as well as science data)

```
CALLING SEQUENCE:
       data = Pckt2Mnemonic(Pckt, Mnemonic [, Status])
INPUTS:
   Pckt     - IDL structure giving Time-ordered data, e.g. as read by
                 FITS_READ_TOD
   Mnemonic - scalar string giving the mnemonic to extract, e.g. 'DK113'

OUTPUTS:
   Status   - A status code: 0=success, -1=error.

RETURNED:
```

```
   data      - The extracted data.

OPTIONAL INPUT KEYWORDS:
   /TIME     - If present and nonzero, the data returned as DLBARR[N,2]
               where data[*,0] gives the WMAP reduced Julian date, and
               data[*,1] gives the extracted data.   It is usually preferable
               to use the TJ output keyword to obtain the Julian dates.
   NFRAMES   - The number of major frames over which to average detector data
               or produce an rms of detector data. Only applies to science
               data mnemonics beginning with 'A' (average) or 'R' (rms).
               Default = 1 MF.
   Other keywords are used by the various data extraction routines.

OPTIONAL OUTPUT KEYWORD:
   TJ - vector of WMAP-reduced Julian dates associated with each data
        point

EXAMPLE:
   After reading a TOD file the Pckt2Mnemonic procedure can be used to
   extract any of the mnemonics defined in Appendix B.

   Extract the raw science data for channel K113 and its time base:

   IDL> dk113_data = Pckt2Mnemonic(arch, 'dk113', tj=tj_sci)

   Extract the major frame average for the same channel:

   IDL> adk114_data = Pckt2Mnemonic(arch, 'adk114', tj=atj_sci)

   Extract the temperature measured by the sensor at the top of the
   A side primary (dtatopprit):

   IDL> trs = Pckt2Mnemonic(arch, 'dtatopprit', tj=tj_trs)
```

4.3   Mapping Procedures

4.3.1   REPROJ_HEALPIX

This procedure converts a HealPix image to a flat map projection without doing any intensity scaling, i.e., the pixel values are in their original units.

```
CALLING SEQUENCE:
   REPROJ_HEALPIX, T, Proj, Subs, [COORD=[1-9], PROJECT=[1,2],
                                   SIZE=[1-5], MASK= ]
INPUT ARGUMENT:
   T   - Vector giving input HEALPix pixel list, full sky.

OUTPUT ARGUMENT:
   Proj   - Output reprojected map, 2-d array
   Subs   - Subscripts that generate the projection from
            the HEALPix vector.
```

```
INPUT KEYWORDS
The following keywords are passed to GET_HEAL_LUT via _EXTRA:
User will be prompted for the following values if they are not
supplied as keywords:

COORD - Scalar Integer (1-9) giving the coordinate system transformation

                        Display
               Galactic   Celestial   Ecliptic
   Native:
   Galactic      1           2           3
   Celestial     4           5           6
   Ecliptic      7           8           9


PROJECT - Scalar integer (1 or 2) giving the type of projection:
           1 - Mollweide
           2 - Zenithal Equal Area

SIZE - Scalar integer giving the size of the output image described
       by the table:
           1 -- Small    (512 x 256)
           2 -- Medium   (1024 x 512)
           3 -- Large    (2048 x 1024)
           4 -- X large  (4096 x 2048)
           5 -- XX large (8192 x 4096, mollweide, native
                                    coordinates only)

OUTPUT KEYWORD:
   Mask  -  Mask outlining the data/nondata ellipse. Same size as
            the output proj parameter

EXAMPLE: Display the K band all-sky map in Galactic coordinates in a
         medium (1024 x 512) size Mollweide projection scaled between
         -0.2 and 1.3 mK.

   IDL> fits_read_map,'map_k_imap_yr1_v1.fits',t,n
   IDL> reproj_healpix,t,proj,coord=1,project=1,size=2
   IDL> tv,bytscl(proj,-.2,1.3)
```

4.3.2 HEALINFO

This procedure prints or returns values describing HEALPix formats of varying resolution.

```
INPUT ARGUMENTS:
   No positional arguments.

INPUT KEYWORDS:
   RES:        Resolution (0 - 10)
   NSIDE:      Number of divisions along edge of biggest
               HEALPix pixel (1, 2, ..., 1024)
   NPIX:       Total number of pixels in full sky
```

```
                   (12, 48, ..., 12582912)
   SPACING:      Approximate mean linear spacing between
                 pixel centers in degrees
   /HELP:        Flag to display short help message.

OUTPUT KEYWORDS:
These mean the same thing as the corresponding input
keywords, except they are used to return results.
   GET_RES
   GET_NSIDE
   GET_NPIX
```

4.3.3 HEALPIX_Nested_Vectors

Procedure to read Cartesian [X,Y,Z] direction vectors from (FITS) binary file for HEALPix pixel scheme, nested pixel order.

```
CALLING SEQUENCE:
   HEALPIX_Nested_Vectors, resolution, Px, Py, Pz
INPUTS:
   Resolution - Scalar integer (3-9) giving the HEALPix resolution
OUTPUTS:
   Px, Py, Pz, - vectors giving the  Cartesian direction vectors for the
                 specified resolution. The number of elements will be
                 768, 3072, 12288, 49152, 196608, 786432 or 3145728 as
                 the resolution is increased from 3 to 9.
```

4.3.4 GRID_OVERLAY

Plot coordinate grid lines on a map projection.

```
CALLING SEQUENCE:
   grid_overlay, [ PROJ={'M','Z'}, IMCOORD={'G','E','C'},
                   GRCOORD={'G','E','C", COLOR =, /PS, IMAGE=,
                   LON= , LAT=, /ZBUFF ]

INPUTS:
   none required, if defaults are satisfactory.

OUTPUTS:
   output consists of a plot, either to screen or postscript file.

OPTIONAL INPUT KEYWORDS:
   proj - char string - Single character specifying the projection type
                        of the plot.  Either 'M' (Mollweide) or
                        'Z' (Zenithal Equal Area) are allowed.  Case
                        insensitive.   Defaults to 'M'.

   imcoord - char string - Single character specifying the coordinate
                        system of the image projection. Three systems are
                        recognized: 'E' (Ecliptic J2000), 'G' (Galactic) or
```

```
                               'C' (Celestial J2000).  Case insensitive.
                               Defaults to 'G'.

   grcoord - char string - Single character specifying the coordinate
                           system of the grid overlay. Three systems are
                           recognized: 'E' (Ecliptic J2000), 'G' (Galactic) or
                           'C' (Celestial J2000).  Case insensitive.
                           Defaults to 'G'.

   color - byte -          The color (range 0-255) used to plot the
                           grid pattern. Defaults to 0.

   /ps - value=0 or 1 - Set this keyword to direct the plot to a postscript
                        file.  The output file is named 'grid_overlay.ps'.
                        If not set, plot will be directed to the screen
                        (windows device).

   image - bytarr -        A byte-scaled image over which the grid will
                           be plotted.  If not specified, the procedure will
                           plot within the current window (screen) or plot
                           a grid with no image to the postscript file (/ps).

   lon - fltarr -          lines of constant longitude, in degrees.
                           Default is every 15 degrees centered on 0.
                           Specifying lon=-1000. results in NO longitude lines.

   lat - fltarr -          lines of constant latitude, in degrees.
                           Default is every 10 degrees centered on 0.
                           Specifying lat=-1000. results in NO latitude lines.

   /zbuff - value=0 or 1 - Set this keyword if plotting to the z buffer
                           is desired.

EXAMPLE:
   Plot ecliptic coordinates grid over the current image
   IDL> grid_overlay, GRCOORD='E'

   Plot a default grid (Mollweide, Galactic) over an image (Kmoll)
   to a postscript file
   IDL> grid_overlay,image=bytscl(Kmoll,0,300),/ps

 COMMENTS:
   The routine scales the overlay to fill the screen window. If the
   user is trying to overlay an image on the screen which does not
   fill the window, then the overlay will be scaled incorrectly.
   The user need not worry about this when creating a postscript image,
   as the image and overlay are scaled together automatically when
   producing the .ps file.

   The Zenithal equal area plot has a hard time plotting the lat=0 edge
   border.  This can be remedied by plotting lat=[-0.00000001,0.0000000001]
   in its place (and this is what the code does by default).
```

4.3.5   CIRCOPLOT

Plots a circle of user-requested radius over an image projection. Circle is centered on the cursor position specified either by the user clicking the left mouse button (screen) or providing a coordinate list (postscript). Option also exists to indicate *WMAP*-visible portions of circle.

```
CALLING SEQUENCE:
   circoplot [,radius=radius] [,proj={'M','Z'} [,color=num]
             [ /visible] [,coord={'G','E','C'},
             [/ps [,image=image] [,ctable=num] [,coorlist=coorlist]

INPUTS:
   Screen mode:
     User positions cursor over image and clicks left mouse button to
     specify circle center.
     Routine remains active until the user clicks the right mouse button.
   Postscript mode:
     User provides a list of centers via coorlist keyword.

OUTPUTS:
   Screen mode:
     Output consists of a circle outline overlayed on an already existing
     image. A small cross is drawn at the requested the circle center
     position. Multiple circles may be drawn during the one call to
     circoplot. Click on right mouse button while the cursor is on the
     image to exit. If /visible is specified, triangles are plotted over
     the WMAP-visible segments of the circle.
   Postscript mode:
     Outputs similar to screen mode and written to file circoplot.ps.
     Plot symbols have been tailored for hardcopy.
     Postscript is written in portrait deliberately to allow user the option
     of using eps and preview options within ghostview.


KEYWORDS:
   radius - float     - Radius of the circle, in degrees.
                        Default value = 141 deg.

   proj - char string - Single character specifying the projection type
                        of the underlying image.  Either 'M' (Mollweide) or
                        'Z' (Zenithal Equal area) are allowed.  Case
                        insensitive.   Defaults to 'M'.

   color - byte -       The color (range 0-255) used to plot the
                        circle and plot symbols. Defaults to 0

   /visible -           Set this keyword to have circoplot indicate those
                        portions of the circle in which the spin axis
                        is within 22.5 deg of the ecliptic.
```

```
                        The result is coordinate system
                        dependent -- see the coord keyword.

   coord - char string -THIS KEYWORD IS MEANINGFUL ONLY IF /VISIBLE
                        IS SPECIFIED.
                        Single character specifying the coordinate
                        system of the projection. Three systems are
                        recognized: 'E' (Ecliptic J2000), 'G' (Galactic) or
                        'C' (Celestial J2000).  Case insensitive.
                        Defaults to 'G'.

   ps - value=0 or 1 -  Set this keyword to direct the plot to a postscript
                        file.  The output file is named 'circoplot.ps'.
                        If not set, plot will be directed to the screen
                        (windows device).

   coorlist - fltarr  - A list of circle center coordinates, in the
                        coordinate system OF THE UNDERLYING IMAGE.
                        Format is [2,N] where N is the number of centers.
                        Must be present when /ps is requested, and is only
                        implemented for ps at present.

   image - bytarr -     A byte-scaled image over which the circles will
                        be plotted.  At present, only implemented for
                        /ps, since user can already plot over an existing
                        image on the screen.

   ctable - long  -     A number specifying which standard IDL color table
                        to load.  Only implemented for /ps.

EXAMPLE:
   IDL> circoplot,radius=10,proj='Z',color=20
   IDL> circoplot,/vis,color=100,coord='e'
   IDL> circoplot,image=myimage,coorlist=[[120,50],[130,80]],/ps
```

4.3.6 PLANET_OVERLAY

Plot a cross at the position of the chosen planet over an existing image within a screen window.

```
CALLING SEQUENCE:
    planet_overlay,gmt=gmt,jd=jd [,planet=planet] [,coord={'G','E','C'}]
                                 [,proj={'M','Z'}] [,color=color]

INPUTS:
   At minimum, use must specify a time, using either the GMT or JD
   keywords (but not both).

OUTPUTS:
   output consists of a plot to screen.
```

```
KEYWORDS:
   gmt - char string - WMAP GMT time for which the planet position is
                       to be computed, e.g., '2000345000000'. Valid
                       GMTs lie between 1 Nov 2000 and 20 April 2003.
                       Do not specify GMT if you are already using the
                       JD keyword.

   jd - scalar or vector - Julian date for which the planet position is
                       to be computed.  Only JDs between 2451849.5 and
                       2452749.5 are accepted.  It is acceptable to
                       input a reduced Julian date with values
                       between 1849.4 and 2749.5.
                       Do not specify JD if you are already using the
                       GMT keyword.

   planet - char string - Name of the planet.  Only one planet may
                       be specified.  Valid planet names are
                       'mars', 'jupiter','saturn','uranus','neptune'.
                       Default planet = 'jupiter'.

   proj - char string - Single character specifying the projection type
                       of the plot.  Either 'M' (Mollweide) or
                       'Z' (Zenithal Equal Area) are allowed.  Case
                       insensitive.    Defaults to 'M'.

   coord - char string - Single character specifying the coordinate
                       system of the projection. Three systems are
                       recognized: 'E' (Ecliptic J2000), 'G' (Galactic)
                       or 'C' (Celestial J2000).  Case insensitive.
                       Defaults to 'G'.

   color - byte -       The color (range 0-255) used to plot the
                       scan pattern. Defaults to 0.

COMMON BLOCKS:
   None.

ROUTINES CALLED:
   is_ieee_big(), gmt2jul, coortrans, mollweide_xy, zea_xy

EXTERNAL FILES REFERENCED:
   The FITS file JPLEPH.405 $MAP_REF/planet_overlay/ provides the JPL
   DE405 ephemeris (as Chebyshev polynomials).

EXAMPLE:
   To overplot Jupiter's positions for 500 days on a Galactic Mollweide
   projection:
     IDL> jd0= 1850.0
     IDL> planet_overlay,jd=jd0+dindgen(500)

COMMENTS:
   The routine scales the overlay to fill the screen window. If the
```

    user is trying to overlay an image on the screen which does not
    fill the window, then the overlay will be scaled incorrectly.

4.4 Transformations

4.4.1 TIMETRANSFORM

Converts one time format into another.

```
CALLING SEQUENCE:
   TimeTransform, input [, output], TransKeyword
INPUTS:
   input  - The input time.  (See KEYWORDS for details.)
OUTPUTS:
   output - The converted time.  (See KEYWORDS for details.)
INPUT KEYWORDS:
   /Date2Jul  - Converts a Gregorian date into reduced Julian day.
                Input should be a 3-6 element array containing the date:
                [year, month, day, hour, minute, second].  Time of day
                elements are optional.
   /DayOfYear - Returns the day of the year for a given date.  Input
                should be a 3-5 element array containing the date:
                [year, month, day, hour, minute]
   /DispGMT   - Converts a GMT string into a more readable string.
   /DispTS    - Converts a WMAP timestamp into a more human readable format

   /DOY2Date  - Determines the date from day-of-year and year.  Input
                should be a 2 element array containing the day of year
                and year.  Output will be a 5 element array containing
                the date: [year, month, day, hour, minute]
   /DOY2Jul   - Determines the reduced Julian day from day-of-year and
                year.  Input should be a 2 element array containing the
                day of year and year.
   /GMT2Jul   - Converts a WMAP GMT date/time string into a Julian day.
   /GMT2TS    - Converts a WMAP GMT into a WMAP timestamp.
   /GMT2YMD   - Converts the YYYYDDD portion of a GMT string to the format
                YYYY:MM:DD.
   /Jul2Date  - Converts a reduced Julian day into a Gregorian date
                and time.  Output consists of a 6 element array containing
                the date: [year, month, day, hour, minute, second].
   /Jul2GMT   - Converts a reduced Julian day into a WMAP GMT date/time .
   /Jul2Tel   - Converts a reduced Julian day into a telemetry structure
                timestamp.  The telemetry structure must already exist!
   /Tel2Jul   - Converts a packet time stamp into a reduced Julian day.
   /TS2GMT    - Converts a WMAP timestamp into a WMAP GMT.
   /TS2Jul    - Converts an array of time stamps into reduced Julian days.

   Reference  - The timestamp reference time in GMT format.
   /Verbose   - If present and nonzero, the output value is written
                to the screen.
```

```
   _EXTRA      - IDL keyword inheritance.  Keywords required by the
                 conversion routines can be passed directly to them
                 simply by specifying them in the call to this routine.
COMMENTS:
  A conversion keyword indicating the type of conversion MUST be
  specified.

  Reduced Julian days referred to here are WMAP Reduced Julian days:
  Full Julian day - 2450000

EXAMPLE:
  Covert the WMAP reduced Julian day extracted using Pckt2mnemonic into
  a GMT string YYYYDDDhhmmsscccc000

    IDL> adk114_data = pckt2mnemonic(arch, 'adk114', tj=atj_sci)
    IDL> TimeTransform, atj_sci, GMT_string, /jul2gmt
    IDL> print, GTM_string[0]
    20013612359350260000
```

4.4.2 COORTRANS

Transforms between various J2000 coordinate systems. No precession is performed.

```
CALLING SEQUENCE:
    coortrans,coor_in,coor_out,code [, /lonlat ]

INPUTS:
  coor_in - fltarr OR dblarr - The input coordinates, specified either
                       as (lon,lat) pairs or unit vector arrays.
                       Unit vectors must be of dimension (N,3).
                       Lonlat pairs must be of dimension (N,2).

  code - char string - Character string specifying the desired
                       coordinate transformation.  Only ONE code
                       may be requested at a time.  Valid codes are:
                 'c2e' - in = celestial   out = ecliptic
                 'e2c' - in = ecliptic    out = celestial
                 'g2e' - in = galactic    out = ecliptic
                 'e2g' - in = ecliptic    out = galactic
                 'c2g' - in = celestial   out = galactic
                 'g2c' - in = galactic    out = celestial
                 'u2ll'- in = unit vector out = lon,lat
                 'll2u'- in = lon,lat     out = unit vector


OUTPUTS:
  coor_out - dblarr - The output coordinates, returned as unit
                       vectors unless /lonlat is set by the user.
                       Unit vectors are returned with dimension (N,3).
                       Lonlat pairs are returned with dimension (N,2).

OPTIONAL INPUT KEYWORDS:
```

```
   /lonlat  -  Set this keyword to get output coordinates
                       returned as longitude,latitude pairs.
                       (Superfluous if code = 'u2ll').

COMMON BLOCKS:
   None.

ROUTINES CALLED:
   get_rot_matrix()

EXAMPLE:
   Transform from celestial unit vectors (x,y,z) to Galactic (lon,lat):

   coortrans,[[x],[y],[z]],galcoor,'c2g',/lonlat

COMMENTS:
   The routine does some rudimentary checking to ensure the input
   and output formats agree with the requested transformation code.
   It also will bounce out if the unit vectors are not normalized.

   Rotation matrices are computed by the routine get_rot_matrix().
```

4.5   Widgets

4.5.1   MAP_DATE

This widget computes and displays dates and times in the various systems used internally by the *WMAP* project. The widget has two modes: continuous update, and calculator. The default mode is to update to the current time once per second. To enter your own data for computations, you need to stop the update, which you can do using the button `Press for Calculator Mode`.

Click on text fields to enter values in them. When you hit the `Enter` key on your keyboard, the changes will propagate through all the quantities in a reasonable way. Self-contradictory data will not mess up the computation, because the program will just use the last type of date and time that you altered. Because continuous update mode is based on system (local) time, the time zone needs to be selected with the droplist at the upper right.

4.5.2   MAPVIEW

This widget displays a HEALPix sky map, and lets the user zoom in on regions of the map on the fly.

```
IDL> mapview,file='map_w1_imap_yr1_v1.fits'
```

The widget displays two images on the right: the upper image is an all-sky map (a Mollweide projection in Galactic coordinates), with a circle drawn over the zoomed region. The lower

512 x 512 image displays the zoomed region. The images are manipulated using the mouse cursor and the control panels on the left.

The Control panel functions are (from top to bottom)

1. `Select Map` – Choose whether to display temperature or number of observations

2. `Cursor Info` – Informational panel giving the Galactic coordinates, Healpix pixel number and pixel value of the current cursor position in either the all-sky or zoomed image. (The panel is disabled if the cursor is not over either image.)

3. `Color Scaling` - lets the user choose linear, logarithmic or histogram equalization scaling, and a color lookup table. Note temperature maps may appear entirely black with a linear scaling.

4. `Zoom Region` - User can type in the Galactic coordinates of the region to be zoomed, and then press the draw button. Alternatively, if the zoom region is selected on the all-sky map with the cursor, then the chosen coordinates are displayed. A slider allows the user to choose the area of the zoomed region; the larger the region, the smaller the zoom factor. The actual pixel scale of the zoomed region is displayed at the terminal.

5. `Quit` button - exits the widget

The mouse cursor functions are as follows: move the cursor over either the all-sky or zoomed image to have values displayed in the `Cursor Info` panel. Press any mouse button on the all sky image to define a new center for the zoomed image. Press any mouse button on the zoomed image to move that position to the center of the zoomed image.

4.6   *WMAP* IDL Procedures

`AIHK_Arch2Mnemonic()`	Returns the physical value associated with an analog instrument housekeeping mnemonic, extracting the data from an AEU sweep from a time-ordered.
`AIHK_GetMnemonic()`	Returns a physical value associated with a mnemonic, extracting the data out of a sweep of analog instrument housekeeping telemetry data.
`AIHK_Pckt2Mnemonic()`	Return the physical value associated with an analog instrument housekeeping mnemonic, extracting the data from a DEU telemetry sweep.
`AIHK_Mnem2Serial`	Return the serial number of an analog instrument housekeeping (AIHK) PRT.

AIHK_Mnem2Serial_List	Returns an array of structures that associates mnemonics with serial numbers for sensor ids.
AIHK_MnemTime	Returns the time offset into a AIHK packet for the measurement of a given mnemonic.
AIHK_MnemTimeStamp	Returns an array of time stamps for a given mnemonic in an array of analog instrument housekeeping (AIHK) elements.
AIHK_Mnem_Coefs	Returns the conversion coefficients associated with an analog instrument housekeeping mnemonic.
AIHK_Mnemonic	Returns the array index of an analog instrument housekeeping mnemonic.
CircOplot	Overplots a circle of requested radius on a Mollweide or Zenithal equal area projection.
CoorTrans	Transforms input J2000 coordinates into the requested J2000 output coordinate system.
CW_ImageDraw()	Defines a compound widget containing a scrollable draw widget to be used to display images.
CW_ImageFull()	Define a compound widget containing a draw widget to be used to display entire images at reduced resolution.
CW_ImageBoth()	Define a compound widget to contain both a full resolution image in a scrollable draw widget and a compressed image.
Date2Jul()	Converts a Gregorian date and time into a reduced Julian date.
DayOfYear	Determines the day-of-year for a date.
DefTSRef()	Return the default *WMAP* timestamp reference GMT.
DIHK_GetMnemonic()	Returns a physical value associated with a mnemonic, extracting the data out of an array of digital instrument housekeeping telemetry data.
DIHK_Pckt2Mnemonic()	Returns the physical value associated with a digital instrument housekeeping mnemonic, extracting the data from a DEU telemetry packet.
DIHK_Mnemonic()	Returns the array index of a digital instrument housekeeping mnemonic.

DIHK_Mnem_Coefs	Returns the conversion coefficients associated with a digital instrument housekeeping (DIHK) mnemonic. Automatically written.
DispGMT()	Converts a time formatted as a *WMAP* GMT into a more human-readable form.
DispTS()	Converts a *WMAP* timestamp into a more human readable format.
DOY2Date	Converts a year and day-of-year into a five element date vector. This is the reverse of dayofyear.pro.
DOY2Jul	Converts a year and day-of-year into a *WMAP* Reduced Julian day.
extract_band_index	Extracts the frequency band and array index value from an input channel string. Supporting routine for sci_getmnemonic.
frame_avg()	Computes single or multiple frame averages of science data. Supporting routine for sci_getmnemonic.
frame_rms()	Computes single or multiple frame rms of science data. Supporting routine for sci_getmnemonic.
FITS_Read_TOD	Read time ordered archive data from a binary FITS table.
FITS_Read_Map	IDL procedure to read *WMAP* archive-format sky maps.
Get_DEU_Int_Temp	Converts DEU internal temperature from counts to degrees Centigrade via a lookup table.
Get_Heal_LUT	Procedure to read and return a user-selectable look-up table.
Get_Heal_RES()	Function to compute the resolution of a healpixelized sky map, given the number of map pixels.
Get_PRT_Temp	Converts PRT resistance in ohms to temperature in Kelvin, given the PRT serial number.
Get_Rot_Matrix()	Returns rotation matrix for conversion between the specified input and output coordinate systems.
GMT2Jul()	Converts a *WMAP* GMT datetime string into a reduced Julian date.
GMT2TS	Converts a *WMAP* GMT into a *WMAP* timestamp.

GMT2YMD	Converts the YYYYDDD portion of a *WMAP* GMT string into a string of format YYYYM-MDD.
Grid_Overlay	Overplots coordinate grid on a Mollweide or Stereographic projection.
HEALinfo	IDL procedure to return or print information on HEALPix resolutions.
HEALPIX_Nested_Vectors	IDL procedure to read Cartesian [X,Y,Z] direction vectors from binary file for HEALPix pixel scheme, nested pixel order.
Jul2Date	Converts a reduced Julian date into a Gregorian date and time. Unlike a classic reduced Julian date, the full Julian date is recovered by adding 2450000.
HealPix_to_Image	Convert a 1-d Healpix map into a 2-d byte-scaled image ready for display.
Jul2GMT()	Converts a *WMAP* GMT date/time string into a Julian date.
Jul2Tel	Converts a *WMAP* Reduced Julian day into a telemetry structure timestamp.
Jul2TS()	Converts a *WMAP* Reduced Julian day into a time stamp.
KeyArray()	Breaks a string containing a number of comma-delimited elements into an array of strings.
KeyFile	Reads a file containing keywordvalue pairs into an array of structures, each element of which contains a keywordvalue pair.
KeyParse	Breaks a string into a keywordvalue pair.
LoadCT_012	Load a standard IDL color table with the first three colors reserved as white, black and gray.
Load_MAP_Params	Reads the contents of the general *WMAP* program parameters file into an IDL structure.
MAP_Date	Widget to convert the various *WMAP* time and date formats.
MAPView	Interactive widget to display and zoom a HealPix map.
Mnem_Type()	Function to return the type of mnemonic associated with an input mnemonic, eg. AIHK, SCI, etc..
mollweide()	Computes Mollweide angle theta from input latitudes.

`mollweide_xy`	Converts longitude and latitude coordinates to x,y positions on a Mollweide projection.
`Now2Jul()`	Returns the current system time as a *WMAP* Reduced Julian day.
`Pckt2Mnemonic()`	Returns the physical value associated with a *WMAP* telemetry mnemonic. This is a wrapper routine that calls the appropriate specific routine depending on mnemonic type.
`Planet_Overlay`	Plots a planet's position on an existing skymap within a screen window.
`projxy2coord`	Converts (x,y) positions on a Mollweide or Zenithal Equal Area projection to longitude and latitude.
`rotx()`	Computes rotation matrix for rotation about x axis.
`rotz()`	Computes rotation matrix for rotation about z axis.
`Sci_GetMnemonic()`	Extracts a channel of radiometer data from an array of science packets. Depending on mnemonic prefix,the routine can also return a frame average or rms.
`Sci_Mnemonic()`	Tests whether or not a given science mnemonic is valid.
`ScrTV`	Displays an image in a scrollable draw widget. This allows the user to examine a full resolution portion of the image, using the scrollbars to navigate around.
`Tel2Jul()`	Converts a *WMAP* telemetry structure time stamp into a reduced Julian date.
`TimeTransform`	Converts one time format into another.
`TS2GMT`	Converts a *WMAP* timestamp into a *WMAP* GMT.
`TS2Jul()`	Converts a time stamp into a *WMAP* Reduced Julian day.
`Reproj_HealPix`	Convert a HealPix image to a flat map projection.
`spread_pckt_tjul()`	Propagate science packet times in reduced Julian format to each observation within a packet. Supporting routine for sci_getmnemonic.

`TextRead`	TextRead reads a non-empty recordline from an open text file. Lines are read until a nonzero length string is read.
`TimeStamp_AddTime`	Adds to a *WMAP* Omega time stamp.
`timestamp_diff()`	Determine the difference between two time stamps.
`tod_format()`	Defines the time-ordered data (TOD) structure format.
`Xcolors`	Interactively change color tables (from David Fanning's Library).
`zea_xy`	Converts longitude and latitude coordinates to x,y positions on a Zenithal equal area projection.

Routines to give the *WMAP* pointing direction at a given time (using the quaternions in the time-ordered data) are expected to be available in the next software release.

Bibliography

R. C. Adamo and J. R. Matarrese. Transient Pulse Monitor Data from P78-2 (SCATHA) Spacecraft. *J Spacecraft*, 20(5):432, 1983.

P. Astier, J. Guy, N. Regnault, R. Pain, E. Aubourg, D. Balam, S. Basa, R. G. Carlberg, S. Fabbro, D. Fouchez, I. M. Hook, D. A. Howell, H. Lafoux, J. D. Neill, N. Palanque-Delabrouille, K. Perrett, C. J. Pritchet, J. Rich, M. Sullivan, R. Taillet, G. Aldering, P. Antilogus, V. Arsenijevic, C. Balland, S. Baumont, J. Bronder, H. Courtois, R. S. Ellis, M. Filiol, A. C. Goncalves, A. Goobar, D. Guide, D. Hardin, V. Lusset, C. Lidman, R. McMahon, M. Mouchet, A. Mourao, S. Perlmutter, P. Ripoche, C. Tao, and N. Walton. The Supernova Legacy Survey: Measurement of Ω_M, Ω_Λ and w from the First Year Data Set. *ArXiv Astrophysics e-prints*, October 2005.

C. Barnes, M. Limon, L. Page, C. Bennett, S. Bradley, M. Halpern, G. Hinshaw, N. Jarosik, W. Jones, A. Kogut, S. Meyer, O. Motrunich, G. Tucker, D. Wilkinson, and E. Wollack. The MAP Satellite Feed Horns. *ApJS*, 143:567–576, December 2002.

C. Barnes, R. S. Hill, G. Hinshaw, L. Page, C. L. Bennett, M. Halpern, N. Jarosik, A. Kogut, M. Limon, S. S. Meyer, G. S. Tucker, E. Wollack, and E. L. Wright. First-Year Wilkinson Microwave Anisotropy Probe (WMAP) Observations: Galactic Signal Contamination from Sidelobe Pickup. *ApJS*, 148:51–62, September 2003.

C. L. Bennett, M. Bay, M. Halpern, G. Hinshaw, C. Jackson, N. Jarosik, A. Kogut, M. Limon, S. S. Meyer, L. Page, D. N. Spergel, G. S. Tucker, D. T. Wilkinson, E. Wollack, and E. L. Wright. The Microwave Anisotropy Probe Mission. *ApJ*, 583:1–23, January 2003a.

C. L. Bennett, M. Halpern, G. Hinshaw, N. Jarosik, A. Kogut, M. Limon, S. S. Meyer, L. Page, D. N. Spergel, G. S. Tucker, E. Wollack, E. L. Wright, C. Barnes, M. R. Greason, R. S. Hill, E. Komatsu, M. R. Nolta, N. Odegard, H. V. Peiris, L. Verde, and J. L. Weiland. First-Year Wilkinson Microwave Anisotropy Probe (WMAP) Observations: Preliminary Maps and Basic Results. *ApJS*, 148:1–27, September 2003b.

C. L. Bennett, R. S. Hill, G. Hinshaw, M. R. Nolta, N. Odegard, L. Page, D. N. Spergel, J. L. Weiland, E. L. Wright, M. Halpern, N. Jarosik, A. Kogut, M. Limon, S. S. Meyer, G. S. Tucker, and E. Wollack. First-Year Wilkinson Microwave Anisotropy Probe (WMAP) Observations: Foreground Emission. *ApJS*, 148:97–117, 2003c.

Y. C. Chen. Survivability of InP HEMT Devices and MMIC's Under High RF Input Drive. In *IEEE MTT-S International Microwave Symposium Digest*, volume 3, pages 1917–1920, 2000.

S. Cole, W. J. Percival, J. A. Peacock, P. Norberg, C. M. Baugh, C. S. Frenk, I. Baldry, J. Bland-Hawthorn, T. Bridges, R. Cannon, M. Colless, C. Collins, W. Couch, N. J. G. Cross, G. Dalton, V. R. Eke, R. De Propris, S. P. Driver, G. Efstathiou, R. S. Ellis, K. Glazebrook, C. Jackson, A. Jenkins, O. Lahav, I. Lewis, S. Lumsden, S. Maddox, D. Madgwick, B. A. Peterson, W. Sutherland, and K. Taylor. The 2dF Galaxy Redshift Survey: power-spectrum analysis of the final data set and cosmological implications. *MN-RAS*, 362:505–534, September 2005.

C. Dickinson, R. A. Battye, P. Carreira, K. Cleary, R. D. Davies, R. J. Davis, R. Genova-Santos, K. Grainge, C. M. Gutiérrez, Y. A. Hafez, M. P. Hobson, M. E. Jones, R. Kneissl, K. Lancaster, A. Lasenby, J. P. Leahy, K. Maisinger, C. Ödman, G. Pooley, N. Rajguru, R. Rebolo, J. Alberto Rubiño-Martin, R. D. E. Saunders, R. S. Savage, A. Scaife, P. F. Scott, A. Slosar, P. Sosa Molina, A. C. Taylor, D. Titterington, E. Waldram, R. A. Watson, and A. Wilkinson. High-sensitivity measurements of the cosmic microwave background power spectrum with the extended Very Small Array. *MNRAS*, 353:732–746, September 2004.

D. J. Eisenstein, I. Zehavi, D. W. Hogg, R. Scoccimarro, M. R. Blanton, R. C. Nichol, R. Scranton, H.-J. Seo, M. Tegmark, Z. Zheng, S. F. Anderson, J. Annis, N. Bahcall, J. Brinkmann, S. Burles, F. J. Castander, A. Connolly, I. Csabai, M. Doi, M. Fukugita, J. A. Frieman, K. Glazebrook, J. E. Gunn, J. S. Hendry, G. Hennessy, Z. Ivezić, S. Kent, G. R. Knapp, H. Lin, Y.-S. Loh, R. H. Lupton, B. Margon, T. A. McKay, A. Meiksin, J. A. Munn, A. Pope, M. W. Richmond, D. Schlegel, D. P. Schneider, K. Shimasaku, C. Stoughton, M. A. Strauss, M. SubbaRao, A. S. Szalay, I. Szapudi, D. L. Tucker, B. Yanny, and D. G. York. Detection of the Baryon Acoustic Peak in the Large-Scale Correlation Function of SDSS Luminous Red Galaxies. *ApJ*, 633:560–574, November 2005.

D. P. Finkbeiner. H-alpha Map. *ApJS*, 2003. accepted (astro-ph/0301558).

D. P. Finkbeiner, M. Davis, and D. J. Schlegel. Extrapolation of Galactic Dust Emission at 100 microns to CMBR Frequencies Using FIRAS. *ApJ*, 524:867, 1999.

A. R Frederickson. Upset Related Spacecraft Charging. *IEEE Transactions on Nuclear Science*, 43(2):426, 1996a.

A. R Frederickson. Correction to Upset Related Spacecraft Charging. *IEEE Transactions on Nuclear Science*, 43:2454, 1996b.

W. L. Freedman, B. F. Madore, B. K. Gibson, L. Ferrarese, D. D. Kelson, S. Sakai, J. R. Mould, R. C. Kennicutt, H. C. Ford, J. A. Graham, J. P. Huchra, S. M. G. Hughes, G. D. Illingworth, L. M. Macri, and P. B. Stetson. Final Results from the Hubble Space Telescope Key Project to Measure the Hubble Constant. *ApJ*, 553:47–72, May 2001.

D. G. Gilmore and M. Bello. *Satellite Thermal Control Handbook*. The Aerospace Corporation Press, El Segundo, CA, 1994.

R. Hadaway et al. Status and Application of Advanced Semiconductor Technologies. In *Gallium Arsenide Manufacturing Technology*, page 1316, 1995.

G. Hinshaw, C. Barnes, C. L. Bennett, M. R. Greason, M. Halpern, R. S. Hill, N. Jarosik, A. Kogut, M. Limon, S. S. Meyer, N. Odegard, L. Page, D. N. Spergel, G. S. Tucker, J. L. Weiland, E. Wollack, and E. L. Wright. First-Year Wilkinson Microwave Anisotropy Probe (WMAP) Observations: Data Processing Methods and Systematic Error Limits. *ApJS*, 148:63–95, September 2003a.

G. Hinshaw, D. N. Spergel, L. Verde, R. S. Hill, S. S. Meyer, C. Barnes, C. L. Bennett, M. Halpern, N. Jarosik, A. Kogut, E. Komatsu, M. Limon, L. Page, G. S. Tucker, J. L. Weiland, E. Wollack, and E. L. Wright. First-Year Wilkinson Microwave Anisotropy Probe (WMAP) Observations: The Angular Power Spectrum. *ApJS*, 148:135–159, September 2003b.

G. Hinshaw, M. R Nolta, C. L. Bennett, R. Bean, O. Doré, M. R. Greason, M. Halpern, R. S. Hill, N. Jarosik, A. Kogut, E. Komatsu, M. Limon, N. Odegard, S. S. Meyer, L. Page, H. V. Peiris, D. N. Spergel, G. S. Tucker, L. Verde, J. L. Weiland, E. Wollack, and E. L. Wright. Three-Year Wilkinson Microwave Anisotropy Probe (WMAP) Observations: Temperature Results. *ApJ, submitted*, 2006.

H. Hoekstra, Y. Mellier, L. van Waerbeke, E. Semboloni, L. Fu, M. J. Hudson, L. C. Parker, I. Tereno, and K. Benabed. First Cosmic Shear Results from the Canada-France-Hawaii Telescope Wide Synoptic Legacy Survey. *ArXiv Astrophysics e-prints*, November 2005.

C. Jackson. Microwave Anisotropy Probe (MAP) Observatory Launch & In-Orbit Checkout (L&IOC) Phase, Volume I: Summary Report. Technical report, NASA/GSFC, 2002.

N. Jarosik, C. Barnes, C. L. Bennett, M. Halpern, G. Hinshaw, A. Kogut, M. Limon, S. S. Meyer, L. Page, D. N. Spergel, G. S. Tucker, J. L. Weiland, E. Wollack, and E. L. Wright. First-Year Wilkinson Microwave Anisotropy Probe (WMAP) Observations: On-Orbit Radiometer Characterization. *ApJS*, 148:29–37, September 2003a.

N. Jarosik, C. L. Bennett, M. Halpern, G. Hinshaw, A. Kogut, M. Limon, S. S. Meyer, L. Page, M. Pospieszalski, D. N. Spergel, G. S. Tucker, D. T. Wilkinson, E. Wollack, E. L. Wright, and Z. Zhang. Design, Implementation, and Testing of the Microwave Anisotropy Probe Radiometers. *ApJS*, 145:413–436, April 2003b.

N. Jarosik, C. Barnes, M. R. Greason, R. S. Hill, M. R. Nolta, N. Odegard, J. L. Weiland, R. Bean, C. L. Bennett, O. Dore, M. Halpern, G. Hinshaw, A. Kogut, E. Komatsu, M. Limon, S. S. Meyer, L. Page, D. N. Spergel, G. S. Tucker, E. Wollack, and E. L. Wright.

Three-Year Wilkinson Microwave Anisotropy Probe (WMAP) Observations: Beam Profiles, Data Processing, Radiometer Characterization and Systematic Error Limits. *ApJ, submitted*, 2006.

R. D. Jimenez. Natural Environment Charged Particle Heating of Spacecraft Cryogenics Components. Technical Report TOR-088(3062)-3, The Aerospace Corporation, 1988.

A. Kogut, D. N. Spergel, C. Barnes, C. L. Bennett, M. Halpern, G. Hinshaw, N. Jarosik, M. Limon, S. S. Meyer, L. Page, G. S. Tucker, E. Wollack, and E. L. Wright. First-Year Wilkinson Microwave Anisotropy Probe (WMAP) Observations: Temperature-Polarization Correlation. *ApJS*, 148:161–173, September 2003.

E. Komatsu, A. Kogut, M. R. Nolta, C. L. Bennett, M. Halpern, G. Hinshaw, N. Jarosik, M. Limon, S. S. Meyer, L. Page, D. N. Spergel, G. S. Tucker, L. Verde, E. Wollack, and E. L. Wright. First-Year Wilkinson Microwave Anisotropy Probe (WMAP) Observations: Tests of Gaussianity. *ApJS*, 148:119–134, September 2003.

C. L. Kuo, P. A. R. Ade, J. J. Bock, C. Cantalupo, M. D. Daub, J. Goldstein, W. L. Holzapfel, A. E. Lange, M. Lueker, M. Newcomb, J. B. Peterson, J. Ruhl, M. C. Runyan, and E. Torbet. High-Resolution Observations of the Cosmic Microwave Background Power Spectrum with ACBAR. *ApJ*, 600:32–51, January 2004.

P. Leung and G. Plamp. Characteristics of RF Resulting from Dielectric Discharge. *IEEE Transactions on Nuclear Science*, 29(6):1610, 1982.

P. Leung, A. C. Whittlesey, H. B. Garrett, and P. A. Robinson. Environment-Induced Electrostatic Discharges as the Cause of Voyager 1 Power-On Resets. *Journal of Spacecraft and Rockets*, 23:323–+, 1986.

P. A. Lilie. X-Band HEMT Burnout Test. Technical report, NRAO/VLA, 1989.

P. F. Mizera. A Summary of Spacecraft Charging Results. *Journal of Spacecraft and Rockets*, 20:438–+, 1983.

T. E. Montroy, P. A. R. Ade, J. J. Bock, J. R. Bond, J. D. Borrill, A. Boscaleri, P. Cabella, C. R. Contaldi, B. P. Crill, P. de Bernardis, G. De Gasperis, A. de Oliveira-Costa, G. De Troia, G. Di Stefano, E. Hivon, A. H. Jaffe, T. S. Kisner, W. C. Jones, A. E. Lange, S. Masi, C. J. MacTavish, A. Melchiorri, P. Natoli, C. B. Netterfield, E. Pascale, F. Piacentini, D Pogosyan, G. Polenta, S. Prunet, S.. Ricciardi, G. Romeo, J. E. Ruhl, P. Santini, M. Tegmark, M. Veneziani, and N. Vittorio. A Measurement of the CMB EE Spectrum from the 2003 Flight of BOOMERANG. *ApJ*, 2005.

L. D. Nguyen et al. 50-nm Self-Aligned-Gate Pseudomorphic AlInAs/GaInAs High Electron Mobility Transistor. *IEEE Transactions on Electron Devices*, 39(9):2007–2014, 1992.

L. Page, C. Barnes, G. Hinshaw, D. N. Spergel, J. L. Weiland, E. Wollack, C. L. Bennett, M. Halpern, N. Jarosik, A. Kogut, M. Limon, S. S. Meyer, G. S. Tucker, and E. L. Wright. First-Year Wilkinson Microwave Anisotropy Probe (WMAP) Observations: Beam Profiles and Window Functions. *ApJS*, 148:39–50, September 2003a.

L. Page, C. Jackson, C. Barnes, C. Bennett, M. Halpern, G. Hinshaw, N. Jarosik, A. Kogut, M. Limon, S. S. Meyer, D. N. Spergel, G. S. Tucker, D. T. Wilkinson, E. Wollack, and E. L. Wright. The Optical Design and Characterization of the Microwave Anisotropy Probe. *ApJ*, 585:566–586, March 2003b.

L. Page, M. R. Nolta, C. Barnes, C. L. Bennett, M. Halpern, G. Hinshaw, N. Jarosik, A. Kogut, M. Limon, S. S. Meyer, H. V. Peiris, D. N. Spergel, G. S. Tucker, E. Wollack, and E. L. Wright. First-Year Wilkinson Microwave Anisotropy Probe (WMAP) Observations: Interpretation of the TT and TE Angular Power Spectrum Peaks. *ApJS*, 148:233–241, September 2003c.

L. Page, G. Hinshaw, E. Komatsu, M. R. Nolta, D. N. Spergel, C. L. Bennett, C. Barnes, R. Bean, O. Doré, M. Halpern, R. S. Hill, N. Jarosik, A. Kogut, M. Limon, S. S. Meyer, N. Odegard, H. V. Peiris, G. S. Tucker, L. Verde, J. L. Weiland, E. Wollack, and E. L. Wright. Three-Year Wilkinson Microwave Anisotropy Probe (WMAP) Observations: Polarization Analysis. *ApJ, submitted*, 2006.

H. V. Peiris, E. Komatsu, L. Verde, D. N. Spergel, C. L. Bennett, M. Halpern, G. Hinshaw, N. Jarosik, A. Kogut, M. Limon, S. S. Meyer, L. Page, G. S. Tucker, E. Wollack, and E. L. Wright. First-Year Wilkinson Microwave Anisotropy Probe (WMAP) Observations: Implications For Inflation. *ApJS*, 148:213–231, September 2003.

M. W Pospieszalski. Modeling of Noise Parameters of MESFET's and MODFET's and Their Frequency and Temperature Dependence. *IEEE Trans. Microwave Theory Tech.*, MTT-37: 1340–1350, 1989.

M. W. Pospieszalski, W. J. Lakatosh, L. D. Nguyen, M. Lui, T. Lui, M. Le, M. A. Thompson, and M. J. Delaney. Q- and E-Band Cryogenically-Coolable Amplifier Using AlInAs/GaInAs/InP HEMTs. In *IEEE MTT-S International Microwave Symposium Digest*, pages 1121–1125, 1995.

M. W. Pospieszalski, W. J. Lakatosh, L. D. Nguyen, M. Le, M. Lui, and T. Lui. Millimeter-Wave Waveguide-Bandwidth Cryogenically-Coolable InP HEMT Amplifiers. In *IEEE MTT-S International Microwave Symposium Digest*, pages 1285–1288, 1997.

M. W Pospieszalski, E. J. Wollack, N. Bailey, D. Thacker, J. Webber, L. D. Nguyen, M. Le, and M. Lui. Design and Performance of Wideband, Low-Noise, Millimeter-Wave Amplifiers for Microwave Anisotropy Probe Radiometers. In *IEEE MTT-S International Microwave Symposium Digest*, volume 1, pages 25–28, Boston, MA, 2000.

M. W Pospieszalski et al. Millimeter-Wave, Cryogenically-Coolable Amplifier Using AlInAs/GaInAs/InP HEMTs. In *IEEE MTT-S International Microwave Symposium Digest*, pages 515–518, 1993.

M. W. Pospieszalski et al. Very Low Noise and Low Power Operation of Cryogenic AlInAs/GaInAs/InP HFET'S. *IEEE MTT-S Digest*, page 1345, 1994.

A. C. S. Readhead, B. S. Mason, C. R. Contaldi, T. J. Pearson, J. R. Bond, S. T. Myers, S. Padin, J. L. Sievers, J. K. Cartwright, M. C. Shepherd, D. Pogosyan, S. Prunet, P. Altamirano, R. Bustos, L. Bronfman, S. Casassus, W. L. Holzapfel, J. May, U.-L. Pen, S. Torres, and P. S. Udomprasert. Extended Mosaic Observations with the Cosmic Background Imager. *ApJ*, 609:498–512, July 2004.

A. G. Riess, L. Strolger, J. Tonry, S. Casertano, H. C. Ferguson, B. Mobasher, P. Challis, A. V. Filippenko, S. Jha, W. Li, R. Chornock, R. P. Kirshner, B. Leibundgut, M. Dickinson, M. Livio, M. Giavalisco, C. C. Steidel, T. Benítez, and Z. Tsvetanov. Type Ia Supernova Discoveries at $z > 1$ from the Hubble Space Telescope: Evidence for Past Deceleration and Constraints on Dark Energy Evolution. *ApJ*, 607:665–687, June 2004.

E. Semboloni, Y. Mellier, L. van Waerbeke, H. Hoekstra, I. Tereno, K. Benabed, S. Gwyn, L. Fu, M. J. Hudson, R. Maoli, and L. Parker. Cosmic Shear Analysis with CFHTLS Deep data. *ArXiv Astrophysics e-prints*, November 2005.

D. N. Spergel, L. Verde, H. V. Peiris, E. Komatsu, M. R. Nolta, C. L. Bennett, M. Halpern, G. Hinshaw, N. Jarosik, A. Kogut, M. Limon, S. S. Meyer, L. Page, G. S. Tucker, J. L. Weiland, E. Wollack, and E. L. Wright. First-Year Wilkinson Microwave Anisotropy Probe (WMAP) Observations: Determination of Cosmological Parameters. *ApJS*, 148:175–194, September 2003.

D. N. Spergel, R. Bean, O. Doré, M. R. Nolta, C. L. Bennett, G. Hinshaw, N. Jarosik, E. Komatsu, L. Page, H. V. Peiris, L. Verde, C. Barnes, M. Halpern, R. S. Hill, A. Kogut, M. Limon, S. S. Meyer, N. Odegard, G. S. Tucker, J. L. Weiland, E. Wollack, and E. L. Wright. Three-Year Wilkinson Microwave Anisotropy Probe (WMAP) Observations: Cosmological Parameters. *ApJ, submitted*, 2006.

S. R. Starin, J R. O'Donnell, Jr., D. K Ward, E. J. Wollack, P. M. Bay, and D. R Fink. An Anomalous Force on the MAP Spacecraft. In *AIAA Symposium*, Monterey, CA, 2002.

M. Tegmark, M. R. Blanton, M. A. Strauss, F. Hoyle, D. Schlegel, R. Scoccimarro, M. S. Vogeley, D. H. Weinberg, I. Zehavi, A. Berlind, T. Budavari, A. Connolly, D. J. Eisenstein, D. Finkbeiner, J. A. Frieman, J. E. Gunn, A. J. S. Hamilton, L. Hui, B. Jain, D. Johnston, S. Kent, H. Lin, R. Nakajima, R. C. Nichol, J. P. Ostriker, A. Pope, R. Scranton, U. Seljak, R. K. Sheth, A. Stebbins, A. S. Szalay, I. Szapudi, L. Verde, Y. Xu, J. Annis, N. A. Bahcall, J. Brinkmann, S. Burles, F. J. Castander, I. Csabai, J. Loveday, M. Doi, M. Fukugita, J. R. I. Gott, G. Hennessy, D. W. Hogg, Ž. Ivezić, G. R. Knapp, D. Q. Lamb, B. C. Lee,

R. H. Lupton, T. A. McKay, P. Kunszt, J. A. Munn, L. O'Connell, J. Peoples, J. R. Pier, M. Richmond, C. Rockosi, D. P. Schneider, C. Stoughton, D. L. Tucker, D. E. Vanden Berk, B. Yanny, and D. G. York. The Three-Dimensional Power Spectrum of Galaxies from the Sloan Digital Sky Survey. *ApJ*, 606:702–740, May 2004.

J. J. Triolo, J. B Heaney, and G. Hass. Coating in Space Environment. In *Optics in Adverse Environments*, volume 121, page 46. SPIE, 1977.

A. L. Vampola, R. D. Jimenez, and J. E. Cox. Heat Loads Due to the Space Particle Environment. *Journal of Spacecraft and Rockets*, 26(6):474–+, 1989.

L. Verde, H. V. Peiris, D. N. Spergel, M. R. Nolta, C. L. Bennett, M. Halpern, G. Hinshaw, N. Jarosik, A. Kogut, M. Limon, S. S. Meyer, L. Page, G. S. Tucker, E. Wollack, and E. L. Wright. First-Year Wilkinson Microwave Anisotropy Probe (WMAP) Observations: Parameter Estimation Methodology. *ApJS*, 148:195–211, 2003.

E. J. Wollack. High-Electron-Mobility-Transistor Gain Stability and its Design Implications for Wide Band Millimeter Wave Receivers. *Rev. Sci. Instrum.*, 66:4305–4312, 1995.

E. J. Wollack and M. W Pospieszalski. Characteristics of Broad-Band InP Millimeter-Wave Amplifiers for Radiometry. In *IEEE MTT-S International Microwave Symposium Digest*, pages 669–772, 1998.

E. L. Wright, G. Hinshaw, and C. L. Bennett. Producing Megapixel Cosmic Microwave Background from Differential Radiometer Data. *ApJ*, 458:L53, February 1996.

Appendix A

Gain Model Parameters

DA	$T_\circ(113)$	$T_\circ(114)$	$T_\circ(123)$	$T_\circ(124)$
K	1.50657120E+01	1.50657120E+01	1.00000000E+04	1.00000000E+04
Ka	-3.79241333E+02	-3.79241333E+02	-8.07621078E+01	-8.07621078E+01
Q1	-3.41706085E+02	-3.41706085E+02	-1.22697762E+02	-1.22697762E+02
Q2	-3.14271832E+01	-3.14271832E+01	-1.91632187E+02	-1.91632187E+02
V1	-4.09649200E+02	-4.09649200E+02	-7.89658356E+01	-7.89658356E+01
V2	-1.20273399E+02	-1.20273399E+02	-2.58686104E+01	-2.58686104E+01
W1	-8.52605743E+01	-8.52605743E+01	-2.38465729E+02	-2.38465729E+02
W2	-3.25313034E+01	-3.25313034E+01	-5.79617882E+01	-5.79617882E+01
W3	-6.87301712E+01	-6.87301712E+01	-6.04023438E+01	-6.04023438E+01
W4	1.00000000E+04	1.00000000E+04	2.85262909E+01	2.85262909E+01

DA	$V_\circ(113)$	$V_\circ(114)$	$V_\circ(123)$	$V_\circ(124)$
K	-2.76059993E-02	-4.38700011E-03	5.55180013E-02	3.20050009E-02
Ka	3.42569984E-02	3.70509997E-02	1.22300005E-02	-5.26999997E-04
Q1	1.84557006E-01	1.53909996E-01	-3.64039987E-02	-3.71900015E-02
Q2	-2.50000012E-04	5.65499999E-03	-8.12800042E-03	-9.47799999E-03
V1	-4.99599986E-02	-4.67979982E-02	1.17710000E-02	1.59590002E-02
V2	-1.05419997E-02	-2.23420002E-02	-1.71949994E-02	-2.50519998E-02
W1	1.02403998E-01	1.44452006E-01	1.02021003E+00	1.73874006E-01
W2	8.46400019E-03	-7.43399980E-03	-1.72014996E-01	1.23387001E-01
W3	-1.60619006E-01	-1.53469995E-01	9.30387020E-01	5.71505010E-01
W4	-1.75584906E+05	-5.67690820E+03	1.03965104E+00	6.63219988E-01

DA	$\beta(113)$	$\beta(114)$	$\beta(123)$	$\beta(124)$
K	-1.83400000E-03	-3.23999993E-04	-1.69299997E-03	-2.62499996E-03
Ka	-5.43999998E-03	-5.27200010E-03	-5.67100011E-03	-5.20499982E-03
Q1	-1.04520004E-02	-1.00229997E-02	-5.14000002E-03	-5.76800015E-03
Q2	-3.13200010E-03	-3.77600011E-03	-5.38699981E-03	-5.17199980E-03
V1	-2.09999993E-03	-2.42500007E-03	-6.29599998E-03	-5.38699981E-03
V2	-4.22299979E-03	-4.39900020E-03	-3.97300022E-03	-3.28500010E-03
W1	-6.53199991E-03	-7.34699983E-03	-9.81500000E-03	-6.26999978E-03
W2	-6.47100015E-03	-7.13799987E-03	-5.73999994E-03	-5.76099986E-03
W3	-5.16600022E-03	-5.21600014E-03	-4.96800011E-03	-9.22700018E-03
W4	4.51618835E+02	1.72249088E+01	-1.31200003E-02	-9.71200038E-03

Table A.1: Gain Model Parameters. These are values for the $T_\circ$, $V_\circ$ and β as defined in Eq. 2 in Jarosik et al. [2006]. The overall amplitude of the gain solution, α, is determined during the map-making process described in Hinshaw et al. [2006].

Appendix B

Selected *WMAP* Log Entries

This appendix consists of selected entries from the events log that the members of the Science Working Group have kept throughout the mission. This particular subset of the log lists all major events from the beginning of the Pre-ship Functional Test (April 6, 2001) to the end of the three year in-flight operations.

```
-------------------------------------------------------------------------
Selected MAP Satellite Pre-Flight Preparations:
-------------------------------------------------------------------------
...
GMT 20010961125   GSFC: Pre-Ship Functional Test (GSFC)
GMT 20011161100   SAEF-2: Post-Ship Functional and CPT (KSC)
GMT 20011621058   SAEF-2: Instrument Contingency Tests (KSC)
GMT 20011721430   SLC17B: Pre-Fairing Pad Functional Test (KSC)
GMT 20011780851   SLC17B: Post-fairing Pad Functional Test (KSC)
GMT 20011791200   SLC17B: Load Vehicle Oxidizer
GMT 20011811013   SLC17B: Instrument Pre-Flight Burn-in
GMT 20011811803   SLC17B: Load Vehicle LOX
GMT 20011811925   SLC17B: Poll to go to Launch Decision Authority (KSC/GSFC)
GMT 20011811929   SLC17B: GSFC poll to Proceed with Terminal Count (GSFC)
GMT 20011811939   SLC17B: Proceed to internal power (KSC/GSFC)


-------------------------------------------------------------------------
Selected MAP Satellite Launch and In-Orbit Checkout (IOC):
-------------------------------------------------------------------------
GMT 20011811946   MAP Launch Time: 2001181194646.183
GMT 20011811951   Main engine cutoff/fairing separation...
GMT 20011812000   SECO-I cutoff -- trajectory is on course...
GMT 20011812100   MAP Transmitter detected by TDRS...
GMT 20011812103   Solar arrays deployed...
GMT 20011812138   Star trackers powered...
GMT 20011812143   MAP Instrument powered...
GMT 20011821515   Gyro calibration slews...
GMT 20011830744   MAP Thruster Tests...
GMT 20011831918   Enter observing mode for the first time:
                  CMB Dipole/galaxy visible in science data
```

```
                      Begin mapping sidelobes with Moon as source
GMT 20011842201   Top Radiator PRT (DTAMXTOPRADT) fails open.
GMT 20011890153   P1 - First Perigee Maneuver
GMT 20011890244   End mapping sidelobs with Moon as source
GMT 20011980143   P2 - Second Perigee Maneuver
GMT 20012021758   A3 - Second Apogee Maneuver (third apogee)
GMT 20012070832   PF - Final Perigee Maneuver
GMT 20012080330   PF'- Final Perigee Correction
GMT 20012080200   PF"- Final Perigee Correction
GMT 20012111639   Lunar Swing-by
GMT 20012181551   Mid-Course Correction #1
GMT 20012181819   W411 Bias Adjustment.
GMT 20012191300   Turn off the omni antenna and switch to the
                      medium gain antenna. FPA is observed to accelerate
                      its cooling. Leave transmitter power to allow ranging.
GMT 20012191807   W411 Returned to Nominal Bias Setting.
GMT 20012210306   W12 Science Output Jump: Sudden jump of W12 science
                      output, both channels W123 and W124 jumped of about
                      35-40 counts in opposite directions. When calibrated
                      the jump is about 100mK. The jump is essentially
                      instantaneous, it happens across just one sample and
                      the dipole is visible before and after the jump. No
                      changes in drain currents or RF bias are present at the
                      time of the output jump. No change noted in other science
                      channels. Observed radiometric signature is consistent
                      with relief of thermally induced stress in radiometer and
                      is anticipated in this phase of mission operations. This
                      and any other subsequent suspect data to be flagged in
                      time stream data mask.


-----------------------------------------------------------------------------
START:  MAP YEAR-ONE SCIENCE DATA
-----------------------------------------------------------------------------


-----------------------------------------------------------------------------
          Transmitter Make-Up Heater Tests
-----------------------------------------------------------------------------
GMT 20012212000   Turn off transmitter: Today we turn off the transmitter
                      for the first time in flight and will turn on the
                      transponder make-up heater when the transmitter is off.
GMT 20012410810   After flying with the transmitter make-up heater for
                      several days, we conclude that the daily thermal cycling
                      seen in the instrument boxes is probably worse than the
                      potential "RFI", and wear on tear on the transmitter. The
                      transmitter will now remain on for the duration of the
                      mission, effective with this pass. Continue the cruise to
                      L2 in this configuration.


-----------------------------------------------------------------------------
          Mid-Course Correction #2
-----------------------------------------------------------------------------
GMT 20012571620   Start Mid-course correction #2: This is a very small
```

```
                   maneuver of about 4.3 cm/sec Delta V. Thrusters #1&2 will
                   be fired for about 6.44sec.
                   The burn will occur at 16:37 GMT.
                   Exit observing mode. Command to spin down at the desired
                   precession angle. Sun angle remains at 22.5 degrees for
                   now. The S/C will shortly be commanded to the desired spin
                   angle.
GMT 20012571625    Command S/C to inertial - this sets up the command to the
                   correct spin angle and will result in a short excursion
                   from 22.5 degrees during the slew.
GMT 20012571627    Actual slew to the correct spin angle.
GMT 20012571635    Slew to 19 degrees in preparation for the burn.
GMT 20012571637    Burn starts and stops.  6.4 seconds.
GMT 20012571639    Return to inertial hold.
GMT 20012571640    Disable thrusters. Enable ACS rate checks.
GMT 20012571641    Slewing back to 22.5 degrees.
GMT 20012571644    Disable thrusters.  Restart TSMs.
GMT 20012571701    Send command to resume observing mode.
-------------------------------------------------------------------------------
          End Mid-Course Correction #2
-------------------------------------------------------------------------------


-------------------------------------------------------------------------------
          Solar Proton Storm
-------------------------------------------------------------------------------

GMT 20012671200    A severe solar storm has occurred with >10 MeV proton
                   fluxes reaching 10^5 times normal levels.  We are
                   observing a heating of the cold stage of several tens of
                   millikelvins with a heating slope that appears to be well
                   correlated with the proton flux. Since this thermal
                   perturbation is larger than the mid-course correction #2
                   we may want to cut a period of data about this time. The
                   storm itself will likely last for a few days.


-------------------------------------------------------------------------------
          ASTB Thermal Change
-------------------------------------------------------------------------------

GMT 200128900      Star tracker crosses internal thermal threshold of CCD
                   thermo-electric cooler. ASTB baseplate cools 4C from
                   30C to 26C. Change in thermal distribution causes RXB to
                   cool by ~10mK.


-------------------------------------------------------------------------------
          Solar Proton Storm
-------------------------------------------------------------------------------

GMT 20013100258    The second severe solar storm since MAP's launch has
                   occurred with >10 MeV proton fluxes reaching >10^5 times
                   normal levels. This is more severe than the previous storm
                   on 2001267.  This storm caused an apparent single event
                   upset (possibly on the power-up reset circuit in the MAC)
                   which caused a power-up cold restart of the Mongoose.
                   All recorded data was lost from the start of the previous
```

```
                   pass to the time of the reset.
                   Telemetry Lost: 20013100258 - 20013101635.
GMT 20013101430    The entry into safehold was noticed on the subsequent pass
                   which started at 20011430.  After spending some time
                   diagnosing the problem, we are preparing to exit safehold
                   and reenter observing mode ~20013101830. The telemetry
                   from the time of the reset until the clock was re-jammed
                   at 20013101542 has a time stamp in 1994.
GMT 20013101742    Command out of safehold to sun-acquisition mode.
GMT 20013101823    Command back to inertial mode.
GMT 20013101825    Slew to 22.5 degrees off the Sun line.
GMT 20013101834    Command to observing mode.
GMT 20013101838    Achieved observing mode.
GMT 20013101903    Adjust clock 1Hz deviation.
GMT 20013101913    Complete clock adjustment.
GMT 20013101943    Return to normal operations.


-------------------------------------------------------------------------------
           Solar Proton Storm
-------------------------------------------------------------------------------
GMT 200132800      A severe solar storm has occurred with >10 MeV proton
                   fluxes reaching 10^5 times normal levels.  We are
                   observing a heating of the cold stage of several tens of
                   millikelvins with a heating slope that appears to be well
                   correlated with the proton flux. Since this thermal
                   perturbation is larger than the mid-course correction #2
                   we may want to cut a period of data about this time. The
                   storm itself will likely last for a few days.


-------------------------------------------------------------------------------
           Station-Keeping Maneuver #1 (SK1)
-------------------------------------------------------------------------------
GMT 20020161620    This is a small maneuver of 42.8 cm/sec delta V that will
                   last for 72 sec.
                   Thrusters #3&4 will be fired at 16:50 GMT.
                   Turn on catbed heaters in preparation for the burn.
GMT 20020161624    Brief drop-out of telemetry.
GMT 20020161633    Exit observing mode. Command to spin down at the desired
                   precession angle. Sun angle remains at 22.5 degrees for
                   now. The S/C will shortly be commanded to the desired spin
                   angle.
GMT 20020161638    Command to go inertial - this sets up the command to the
                   correct spin angle and will result in a small excursion
                   from 22.5 degrees during the slew.
GMT 20020161639    Actual slew to the correct spin angle.
GMT 20020161648    Slew to 19 degrees in preparation for the burn.
GMT 2002016165055  Burn starts, lasts 72 seconds, as planned.
GMT 20020161652    Return to inertial hold.
GMT 20020161653    Disable thrusters. Enable ACS rate checks.
GMT 20020161656    Return to observing mode 5 minutes after burn.
-------------------------------------------------------------------------------
           End Station-Keeping Maneuver #1 (SK1)
```

```
-------------------------------------------------------------------------------

-------------------------------------------------------------------------------
            Reaction Wheel 3 Temperature Increase
-------------------------------------------------------------------------------
GMT 2002054      Reaction Wheel 3 bearing temperature increased by about
                 1.2K and the corresponding wheel's flange by about ~1K.
                 ACS attributes this behavior to movement of the bearings'
                 lubricant. Previous flight experience with this design
                 suggests that this behavior is anticipated.


-------------------------------------------------------------------------------
            Battery Anomaly
-------------------------------------------------------------------------------
GMT 2002054      Around this day the battery differential voltage started
                 to deviate from its nominal value. Evidence suggests that
                 effect is due to a partially shorted cell.
GMT 2002058      The S/C responds to the continuous raise of the
                 differential voltage by resetting the battery VT curve
                 to VT0 per design.


-------------------------------------------------------------------------------
            Reaction Wheel 1 Temperature Increase
-------------------------------------------------------------------------------
GMT 2002075      At ~20020750445 the drag torque level and the temperatures
                 of both bearing and flange of RWA stepped up by about
                 0.002 Nm 1 C respectively. Have seen similar changes in
                 the past and they are not considered an anomaly.


-------------------------------------------------------------------------------
            Station-Keeping Maneuver #2 (SK2)
-------------------------------------------------------------------------------
GMT 20021281533    This is a small maneuver of 34.8 cm/sec delta V that will
                   last for 49 sec.
                   Thrusters #1&2 will be fired at 16:03 GMT.
                   Turn on catbed heaters in preparation for the burn.
GMT 20021281546    Exit observing mode. Command to spin down at the desired
                   precession angle. Sun angle remains at 22.5 degrees for
                   now. The S/C will shortly be commanded to the desired spin
                   angle.
GMT 20021281551    Command to go inertial -- this sets up the command to the
                   correct spin angle and will result in a small excursion
                   from 22.5 degrees during the slew.
GMT 20021281552    Actual slew to the correct spin angle.
GMT 20021281601    Slew to 19 degrees in preparation for the burn.
GMT 2002128160327 Burn starts, lasts 49 seconds, as planned.
GMT 20021281604    Return to inertial hold.
GMT 20021281609    Disable thrusters. Enable ACS rate checks.
GMT 20021281610    Slew back to 22.5 degrees in preparation for observing
                   mode.
GMT 20021281612    Return to observing mode 5 minutes after burn.
```

```
--------------------------------------------------------------------------
          End Station-Keeping Maneuver #2 (SK2)
--------------------------------------------------------------------------


GMT 20021582120   Shift in nominal AEU/DEU temperature of ~28mK observed in
                  PRTs sensors. Source localized near DVA223_4AMPT PRT
                  sensor from spatial and temporal evolution of observed
                  event. Estimate change in card power dissipation of~+0.1%
                  Correlated response in science data is not detected.


--------------------------------------------------------------------------
          Station-Keeping Maneuver #3 (SK3)
--------------------------------------------------------------------------
GMT 20022111608   This is a small maneuver of 45.98 cm/sec delta V that will
                  last for 66 sec.
                  Thrusters #1&2 will be fired at 16:38:45 GMT.
                  Turn on catbed heaters in preparation for the burn.
GMT 20022111621   Exit observing mode. Command to spin down at the desired
                  precession angle. Sun angle remains at 22.5 degrees for
                  now. The S/C will shortly be commanded to the desired spin
                  angle.
GMT 20022111626   Command to go inertial - this sets up the command to the
                  correct spin angle and will result in a small excursion
                  from 22.5 degrees during the slew.
GMT 20022111627   Actual slew to the correct spin angle.
GMT 20022111635   Disable RTS 181, system rate checks.
GMT 20022111636   Slew to 19 degrees in preparation for the burn.
GMT 2002211163845 Burn starts, lasts 66 seconds, as planned.
GMT 20022111640   Return to inertial hold.
GMT 20022111642   Disable thrusters. Enable ACS rate checks.
GMT 20022111642   Disable catbed heaters.
GMT 2002211164245 Slew back to 22.5 degrees in preparation for observing
                  mode.
GMT 20022111646   Return to observing mode 4 minutes after burn, 26 minutes
                  after leaving observing mode.
--------------------------------------------------------------------------
          End Station-Keeping Maneuver #3 (SK3)
--------------------------------------------------------------------------


GMT 2002222       End of year-one data
--------------------------------------------------------------------------
END:  MAP YEAR-ONE DATA
--------------------------------------------------------------------------


--------------------------------------------------------------------------
Recorder Memory Mask Update
--------------------------------------------------------------------------
                  During this pass, modification to the solid state recorder
                  memory map to mask out 3 bits that have repeatedly shown
                  single bit errors will be uploaded.


GMT 20022951830   Perform a retransmit of the VR3 DS1 data set to minimize
```

                the amount of lost data.

GMT 20022951843   Modify data storage quota table #28.

GMT 20022951854   Commit Data Storage Segment Table #27 to mask the
                            offending bits in the recorder. This clears all
                            existing recorder memory.

GMT 20022951900   Modify Memory Scrub Segment Table #19. This will
                            cause the memory scrub routine to skip the offending
                            bits of recorder memory.

GMT 20022951910   Estimate that 16-18 VCDUs of data were lost
                            during operation (~9 seconds).

GMT 20022951937   The first cycle of the memory scrub skipped over
                            the first masked bit address, as planned.
```
-----------------------------------------------------------------------------
```
End Recorder Memory Mask Update
```
-----------------------------------------------------------------------------


-----------------------------------------------------------------------------
```
Station-Keeping Maneuver #4 (SK4)
```
-----------------------------------------------------------------------------
```
                This is a small maneuver of 56.4 cm/sec delta V that
                will last for 95.5 sec. Thrusters #3&4 will be fired
                at 19:20:43 GMT. Thruster scale factor (TSF) 0.951.

GMT 20023091850   Turn on catbed heaters in preparation for the burn.

GMT 20023091904   Exit observing mode. Command to spin down at the
                            desired precession angle. Sun angle remains at 22.5
                            degrees for now. The s/c will shortly be commanded
                            to the desired spin angle.

GMT 20023091908   Command to go inertial - this sets up the command to
                            the correct spin angle and will result in a small
                            excursion from 22.5 degrees during the slew.

GMT 20023091909   Actual slew to the correct spin angle.

GMT 20023091916   Disable RTS 181, system rate checks, enable thrusters.

GMT 20023091918   Slew to 19 degrees in preparation for the burn.

GMT 2002309192043 Burn starts, lasts 95.5 seconds, as planned.

GMT 20023091922   Back to inertial hold.

GMT 20023091923   Disable thrusters. Enabling ACS system rate checks.

GMT 20023091924   Disable catbed heaters.

```
GMT 20023091925   Slew back to 22.5 degrees in preparation for observing mode.

GMT 20023091926   Return to observing mode 6 minutes after burn, 22
                  minutes after leaving observing mode.

GMT 20023091936   Turn off iso-valve driver power.
-----------------------------------------------------------------------------
End Station-Keeping Maneuver #4 (SK4)
-----------------------------------------------------------------------------


-----------------------------------------------------------------------------
Update Solar Ephemeris
-----------------------------------------------------------------------------
GMT 20023092005   The solar ephemeris table used for on board navigation is
                  being updated with a new polynomial fit.  The new ephemeris
                  will cause a ~30 arcsec jump in the solar position. Such an
                  update is estimated to be required approximately annually.
-----------------------------------------------------------------------------
End Update Solar Ephemeris
-----------------------------------------------------------------------------


-----------------------------------------------------------------------------
Station-Keeping Maneuver #5 (SK5)
-----------------------------------------------------------------------------
                  This is a small maneuver of 32.07 cm/sec delta V that
                  will last for 50 sec. Thrusters #1&2 will be fired
                  at 13:50:13 GMT.  Thruster scale factor (TSF) 0.983.

GMT 20030711320   Turn on catbed heaters in preparation for the burn.

GMT 20030711332   Command to spin down.  Spin down completed ~13:39.

GMT 20030711341   Disable RTS 181, system rate checks, enable thrusters.

GMT 20030711350   Thrusters firing.  Burn duration nominal.

GMT 20030711352   Disable all thrusters. Turn catbed heaters off 13:52:45.

GMT 20030711353   Slew to 22.5 deg.

GMT 20030711355   Go to observing mode 13:54:48.
                  Primary temperature max increase by ~8 mK
                  at ~13:49:30 as result of maneuver.
-----------------------------------------------------------------------------
End Station-Keeping Maneuver #5 (SK5)
-----------------------------------------------------------------------------


GMT 2003222       End of year-two data


-----------------------------------------------------------------------------
END: MAP YEAR-TWO DATA
```

```
--------------------------------------------------------------------

--------------------------------------------------------------------
Safehold Event
--------------------------------------------------------------------
GMT 2003223       The Mongoose V apparently experienced a Power-On type of
                  restart similar to the event that occurred on November 6,
                  2001. The routine scheduled pass on Day 223 had a BOT of
                  1615 UT with station D43. At BOT the station had lock on
                  a carrier signal but there was no data lock.
                  The S/C's attitude control was verified as being in the
                  safehold mode and the apparent Mongoose V Power-On restart
                  identified.

  The elapsed time from the routine scheduled pass during
  which the anomaly was identified until Observing mode was
  re-established was 7 hours 23 minutes 50 seconds. The VR1
  (housekeeping) data loss covers the time from the last
  successful playback until the time the restart finished
      and was 20 hours 52 minutes 51 seconds. The VR3 (science)
      data loss covers the time from the last successful
  playback until Observing mode was re-established and was
  31 hours 5 minutes 36 seconds.

GMT 20032231942   Ready to try to go back to B-side
GMT 20032231950   Reconfigured DSN to get back to B-side, communicating with
                  MGA at 666 Kbps 1/4 rate, carrier locked at DSN Camberra.

GMT 20032235520   We are receiving data

GMT 20032232256   Completed uploading changes (patches, procs, limits, etc.),
                    leaving safehold
GMT 20032232259   Going to Sun aquisition

GMT 2003223232700 Going inertial

GMT 2003223232833 Slewing to 22.5 degs

GMT 2003223233350 Inertially holding at 22.5 degs

GMT 2003223233455 Going to Observing mode

GMT 2003223233515 Spinning up

GMT 20032232348   Switching to mission filter table

GMT 20032232340   Dumping data
--------------------------------------------------------------------
End of Safehold Event
--------------------------------------------------------------------

--------------------------------------------------------------------
```

```
Solar Flare Supplemental Passage
-------------------------------------------------------------------------------
GMT 200330202   This passage was scheduled because we undergoing a
      severe solar storm. High energy (>100 MeV) proton flux has
      reached 2e10 Pcm^-2s^-1sr^-1 comparable to the flux that
      put the Spacecraft in safehold on 20013100258

      Spacecraft is not in safehold but there are 19 bus errors
      on ASTA and the Tracker switched from AST A to B at
      00:03:03 GMT

      Dumped the recorders

GMT 2003302030357 Reset the AST to the A side and clear errors
                  Back on AST A tracker. System appears nominal.


-------------------------------------------------------------------------------
End Solar Flare Supplemental Passage
-------------------------------------------------------------------------------


-------------------------------------------------------------------------------
Station-keeping Maneuver #6 (SK6)
-------------------------------------------------------------------------------
                  This is a small maneuver of 25.06 cm/sec delta V that
                  will last for 42.22 sec. Thrusters #3&4 will be fired
                  at 15:10:56 GMT.  Thruster scale factor (TSF) 0.9502.

GMT 20033161440   Turn on catbed heaters in preparation for the burn.

GMT 20033161454   Command to spin down.  Spin down completed ~14:56.

GMT 20033161459   Go to intertial mode.

GMT 20033161500   Slew #1 to commanded quaternion @22.5 degree Sun angle.

GMT 20033161506   Disable RTS 181, system rate checks, enable thrusters.

GMT 20033161509   Slew #2 to commanded quaternion @19 degree Sun angle.

GMT 20033161510   Thrusters firing @15:10:56. Burn duration nominal.

GMT 20033161513   Disable all thrusters. Turn catbed htrs off 15:13:30.

GMT 20033161515   Slew #3 to commanded quaternion @22.5 degree Sun angle.

GMT 20033161519   Go to observing mode after delta-t = 25 min 7 sec.
      Primary temperatures increased by ~30 mK at ~15:12:32
      as result of maneuver.


-------------------------------------------------------------------------------
End Station-keeping Maneuver #6
-------------------------------------------------------------------------------
```

```
--------------------------------------------------------------------------
Station-keeping Maneuver #7 (SK7)
--------------------------------------------------------------------------
                  This is a small maneuver of 66.3 cm/sec delta V that
                  will last for 112 sec. Thrusters #3&4 will be fired
                  at 15:24:56 GMT.  Thruster scale factor (TSF) 0.95.

GMT 20040691525   Thrusters firing @15:24:56. Burn duration nominal.


--------------------------------------------------------------------------
End Station-keeping Maneuver #7 (SK7)
--------------------------------------------------------------------------


GMT 2004222       End of year-three data


--------------------------------------------------------------------------
END: MAP YEAR-THREE DATA
--------------------------------------------------------------------------
```

Appendix C

Mnemonics Lists

Signals in the *WMAP* telemetry are uniquely identified by a set of mnemonics. Identifying a specific signal using its mnemonic allows the user to extract it from a more complex data structure using software routines which are provided (see Chapter 4). The main signals of interest in the *WMAP* time-ordered data are described by the science and the housekeeping mnemonics, these are all listed in this appendix grouped by their functionalities. For the mnemonics associated with a temperature sensor the description field indicates the approximate position of that sensor on the observatory.

C.1 Science Mnemonics

Raw Data	Major Frame First Point	Major Frame Average	Major Frame RMS
DK113	QDK113	ADK113	RDK113
DK114	QDK114	ADK114	RDK114
DK123	QDK123	ADK123	RDK123
DK124	QDK124	ADK124	RDK124
DKA113	QDKA113	ADKA113	RDKR113
DKA114	QDKA114	ADKA114	RDKR114
DKA123	QDKA123	ADKA123	RDKR123
DKA124	QDKA124	ADKA124	RDKR124
DQ113	QDQ113	ADQ113	RDQ113
DQ114	QDQ114	ADQ114	RDQ114
DQ123	QDQ123	ADQ123	RDQ123
DQ124	QDQ124	ADQ124	RDQ124
DQ213	QDQ213	ADQ213	RDQ213
DQ214	QDQ214	ADQ214	RDQ214
DQ223	QDQ223	ADQ223	RDQ223
DQ224	QDQ224	ADQ224	RDQ224
DV113	QDV113	ADV113	RDV113
DV114	QDV114	ADV114	RDV114
DV123	QDV123	ADV123	RDV123
DV124	QDV124	ADV124	RDV124
DV213	QDV213	ADV213	RDV213
DV214	QDV214	ADV214	RDV214
DV223	QDV223	ADV223	RDV223
DV224	QDV224	ADV224	RDV224
DW113	QDW113	ADW113	RDW113
DW114	QDW114	ADW114	RDW114
DW123	QDW123	ADW123	RDW123
DW124	QDW124	ADW124	RDW124
DW213	QDW213	ADW213	RDW213
DW214	QDW214	ADW214	RDW214
DW223	QDW223	ADW223	RDW223
DW224	QDW224	ADW224	RDW224
DW313	QDW313	ADW313	RDW313
DW314	QDW314	ADW314	RDW314
DW323	QDW323	ADW323	RDW323
DW324	QDW324	ADW324	RDW324
DW413	QDW413	ADW413	RDW413
DW414	QDW414	ADW414	RDW414
DW423	QDW423	ADW423	RDW423
DW424	QDW424	ADW424	RDW424

C.2 Instrument Housekeeping Mnemonics

C.2.1 Amplifier Drain Currents

Mnemonic	Description	Mnemonic	Description
DFK111B8DNI	K111 FPA	DFV211B9DNI	V211 FPA
DFK112B8DNI	K112 FPA	DFV212B9DNI	V212 FPA
DFK121B8DNI	K121 FPA	DFV221B9DNI	V221 FPA
DFK122B8DNI	K122 FPA	DFV222B9DNI	V222 FPA
DRK111B8DNI	K111 RXB	DRV211B9DNI	V211 RXB
DRK112B8DNI	K112 RXB	DRV212B9DNI	V212 RXB
DRK121B8DNI	K121 RXB	DRV221B9DNI	V221 RXB
DRK122B8DNI	K122 RXB	DRV222B9DNI	V222 RXB
DFKA111B3DNI	Ka111 FPA	DFW111B4DNI	W111 FPA
DFKA112B3DNI	Ka112 FPA	DFW112B4DNI	W112 FPA
DFKA121B3DNI	Ka121 FPA	DFW121B4DNI	W121 FPA
DFKA122B3DNI	Ka122 FPA	DFW122B4DNI	W122 FPA
DRKA111B3DNI	Ka111 RXB	DRW111B4DNI	W111 RXB
DRKA112B3DNI	Ka112 RXB	DRW112B4DNI	W112 RXB
DRKA121B3DNI	Ka121 RXB	DRW121B4DNI	W121 RXB
DRKA122B3DNI	Ka122 RXB	DRW122B4DNI	W122 RXB
DFQ111B1DNI	Q111 FPA	DFW211B5DNI	W211 FPA
DFQ112B1DNI	Q112 FPA	DFW212B5DNI	W212 FPA
DFQ121B1DNI	Q121 FPA	DFW221B5DNI	W221 FPA
DFQ122B1DNI	Q122 FPA	DFW222B5DNI	W222 FPA
DRQ111B1DNI	Q111 RXB	DRW211B5DNI	W211 RXB
DRQ112B1DNI	Q112 RXB	DRW212B5DNI	W212 RXB
DRQ121B1DNI	Q121 RXB	DRW221B5DNI	W221 RXB
DRQ122B1DNI	Q122 RXB	DRW222B5DNI	W222 RXB
DFQ211B10DNI	Q211 FPA	DFW311B6DNI	W311 FPA
DFQ212B10DNI	Q212 FPA	DFW312B6DNI	W312 FPA
DFQ221B10DNI	Q221 FPA	DFW321B6DNI	W321 FPA
DFQ222B10DNI	Q222 FPA	DFW322B6DNI	W322 FPA
DRQ211B10DNI	Q211 RXB	DRW311B6DNI	W311 RXB
DRQ212B10DNI	Q212 RXB	DRW312B6DNI	W312 RXB
DRQ221B10DNI	Q221 RXB	DRW321B6DNI	W321 RXB
DRQ222B10DNI	Q222 RXB	DRW322B6DNI	W322 RXB
DFV111B2DNI	V111 FPA	DFW411B7DNI	W411 FPA
DFV112B2DNI	V112 FPA	DFW412B7DNI	W412 FPA
DFV121B2DNI	V121 FPA	DFW421B7DNI	W421 FPA
DFV122B2DNI	V122 FPA	DFW422B7DNI	W422 FPA
DRV111B2DNI	V111 RXB	DRW411B7DNI	W411 RXB
DRV112B2DNI	V112 RXB	DRW412B7DNI	W412 RXB
DRV121B2DNI	V121 RXB	DRW421B7DNI	W421 RXB
DRV122B2DNI	V122 RXB	DRW422B7DNI	W422 RXB

C.2.2 Radiometer RF Bias (Total Power)

Mnemonic	Description
DRK113RFBI0	K113 RF bias
DRK114RFBI1	K114 RF bias
DRK123RFBI2	K123 RF bias
DRK124RFBI3	K124 RF bias
DRKA113RFBI36	Ka113 RF bias
DRKA114RFBI37	Ka114 RF bias
DRKA123RFBI38	Ka123 RF bias
DRKA124RFBI39	Ka124 RF bias
DRQ113RFBI20	Q113 RF bias
DRQ114RFBI21	Q114 RF bias
DRQ123RFBI22	Q123 RF bias
DRQ124RFBI23	Q124 RF bias
DRQ213RFBI28	Q213 RF bias
DRQ214RFBI29	Q214 RF bias
DRQ223RFBI30	Q223 RF bias
DRQ224RFBI31	Q224 RF bias
DRV113RFBI32	V113 RF bias
DRV114RFBI33	V114 RF bias
DRV123RFBI34	V123 RF bias
DRV124RFBI35	V124 RF bias
DRV213RFBI12	V213 RF bias
DRV214RFBI13	V214 RF bias
DRV223RFBI14	V223 RF bias
DRV224RFBI15	V224 RF bias
DRW113RFBI4	W113 RF bias
DRW114RFBI5	W114 RF bias
DRW123RFBI2	W123 RF bias
DRW124RFBI3	W124 RF bias
DRW213RFBI24	W213 RF bias
DRW214RFBI25	W214 RF bias
DRW223RFBI26	W223 RF bias
DRW224RFBI27	W224 RF bias
DRW313RFBI16	W313 RF bias
DRW314RFBI17	W314 RF bias
DRW323RFBI18	W323 RF bias
DRW324RFBI19	W324 RF bias
DRW413RFBI8	W413 RF bias
DRW414RFBI9	W414 RF bias
DRW423RFBI10	W423 RF bias
DRW424RFBI11	W424 RF bias

C.2.3 TRS Temperatures

Mnemonic	Description
DTATOPPRIT	A side primary temp (top)
DTAMIDPRIT	A side primary temp (middle)
DTATOPSECT	A side secondary temp (top)
DTAMIDSECT	A side secondary temp (middle)
DTABOTSECT	A side secondary temp (bottom)
DTBTOPPRIT	B side primary temp (top)
DTBMIDPRIT	B side primary temp (middle)
DTBTOPSECT	B side secondary temp (top)
DTBMIDSECT	B side secondary temp (middle)
DTAPXMIDRADT	+X radiator, A side temp (middle)
DTBPXMIDRADT	+X radiator, B side temp (middle)
DTAMXTOPRADT	-X radiator, A side temp (top)
DTBMXBOTRADT	-X radiator, B side temp (bottom)

C.2.4 FPA Temperatures

Mnemonic	Description
DFK1AFEEDT	K1 A side feed temp (upper)
DFW3BFEEDT	W3 B side feed temp (middle)
DFQ1AFEEDT	Q1 A side feed temp (lower)
DFKA1BFEEDT	Ka1 B side feed temp (upper)
DFW3AFEEDT	W3 A side feed temp (middle)
DFQ2BFEEDT	Q2 B side feed temp (lower)
DFK1BOMTT	K1 B side OMT temp (upper)
DFW3AOMTT	W3 A side OMT temp (middle)
DFQ1BOMTT	Q1 B side OMT temp (lower)
DFKA1AOMTT	Ka1 A side OMT temp (upper)
DFW3BOMTT	W3 B side OMT temp (middle)
DFQ2AOMTT	Q2 A side OMT temp (lower)
DFV11FPATEET	V11 FPA magic tee temp
DFV22FPATEET	V22 FPA magic tee temp
DFW11FPATEET	W11 FPA magic tee temp
DFW22FPATEET	W22 FPA magic tee temp
DFW32FPATEET	W32 FPA magic tee temp

C.2.5 RXB Temperatures

Mnemonic	Description
DRV111RXBAMPT	V111 RXB amplifier temp
DRV222RXBAMPT	V222 RXB amplifier temp
DRW111RXBAMPT	W111 RXB amplifier temp
DRW221RXBAMPT	W221 RXB amplifier temp
DRW321RXBAMPT	W321 RXB amplifier temp
DRK12RXBRIBT	K12 RXB rib temp
DRKA12RXBRIBT	Ka12 RXB rib temp
DRQ1RXBRIBT	Q1 RXB rib temp
DRQ2RXBRIBT	Q2 RXB rib temp
DRW3RXBRIBT	W3 RXB rib temp
DRPYPSHPRTKT	+Y phase switch driver board temp
DRMYPSHPRTKT	-Y phase switch driver board temp

C.2.6 AEU Temperatures

Mnemonic	Description
DAW323_4AMPT	W3 board temp between 23/24 amps
DAW2_14_23AMP_ADT	W2 board temp between 14/23 amps & a/d
DAV113_4ADT	V1 board temp between 13/14 a/d's
WDAW113_4ADT	W1 board temp between 13/14 a/d's
DAV223_4AMPT	V2 board temp between 23/24 amps
DAQ113_4ADT	Q1 board temp between 13/14 a/d's
DAIHK1BDT	Housekeeping board 1 temp
DAIHK2BDT	Housekeeping board 2 temp
DACONVBDT	Power converter board temp

C.2.7 PDU Temperatures

Mnemonic	Description
DPPINTT1	PDU internal temperature #1
DPPINTT2	PDU internal temperature #2
DPPINTT3	PDU internal temperature #3
DPV111_2FPAT	V111/2 FPA regulator board temp
DPW221_2FPAT	W221/2 FPA regulator board temp
DPW321_2FPAT	W321/2 FPA regulator board temp
DPV221_2RXBT	V221/2 RXB regulator board temp
DPW111_2RXBT	W111/2 RXB regulator board temp
DPW321_2RXBT	W321/2 RXB regulator board temp

C.2.8   AEU Voltages and Reference Roads

Mnemonic	Description
DAP15VBD1	Housekeeping board 1 +15V converter
DAM15VBD1	Housekeeping board 1 -15V converter
DAP12VBD1	Housekeeping board 1 +12V converter
DAM12VBD1	Housekeeping board 1 -12V converter
DAP5VBD1	Housekeeping board 1 +5V converter
DAP15VBD2	Housekeeping board 2 +15V converter
DAM15VBD2	Housekeeping board 2 -15V converter
DAP12VBD2	Housekeeping board 2 +12V converter
DAM12VBD2	Housekeeping board 2 -12V converter
DAP5VBD2	Housekeeping board 2 +5V converter
DABD1V	Housekeeping board 1 ref. voltage
DARREF1BD1	Housekeeping board 1 ref. resistance #1
DARREF2BD1	Housekeeping board 1 ref. resistance #2
DABD2V	Housekeeping board 2 ref. voltage
DARREF1BD2	Housekeeping board 2 ref. resistance #1
DARREF2BD2	Housekeeping board 2 ref. resistance #2
DASPARE1	Spare

C.2.9   PDU Voltages

Mnemonic	Description
DPFP7_2V	FPA HEMT regulator +7.2V converter
DPFM7_2V	FPA HEMT regulator -7.2V converter
DPRP7_2V	RXB HEMT regulator +7.2V converter
DPRM7_2V	RXB HEMT regulator -7.2V converter
DPFLEDP10V	LED +10V converter voltage
DPPHSWCONVP9V	Phase switch driver +9V converter
DPPHSWCONVM9V	Phase switch driver -9V converter
DPFLDAP6_2V	Line driver A, DAs 1-5 +6.2V converter
DPFLDAM6_2V	Line driver A, DAs 1-5 -6.2V converter
DPFLDBP6_2V	Line driver B, DAs 6-10 +6.2V converter
DPFLDBM6_2V	Line driver B, DAs 6-10 -6.2V converter
DPHKP15V	Housekeeping +15 V converter
DPHKP5V	Housekeeping +5 V converter
DPHKM15V	Housekeeping -15 V converter

Appendix D

Acronym List

°C	[degree centigrade]
A	[amp]
A-hr	[amp hour]
A/D	Analog to Digital
A/C	Air Conditioning
AC	Alternating Current
ACE	Attitude Control Electronics
ACS	Attitude Control System
AEU	Analog Electronics Unit
ANSI	American National Standards Institute
AO	Announcement of Opportunity
AOS	Acquisition of Signal
APID	Application Process Identification
ASIC	Application Specific Integrated Circuit
ASIST	Advanced System for Integration and Spacecraft Testing
ASQC	American Society for Quality Control
AST	Autonomous Star Tracker
ATC	Active Thermal Control
ATS	Applications Technology Satellite
	Absolute Time Sequence
AWG	American Wire Gauge
AWS	Associate Work Station
BB	Breadboard
BER	Bit Error Rate
BIB	Bus Interface Box
BOA	Beginning of Activity
BOL	Beginning of Life
BOT	Beginning of Track
bps	[bits per sec]
BPT	Business Product Team
BSOC	Battery State of Charge
BTE	Bench Test Equipment
BWG	Beam Wave Guide
BW	Bandwidth
C&DH	Command & Data Handling

CADU	Channel Access Data Unit
CCAS	Cape Canaveral Air Station
CCB	Configuration Control Board
CCD	Charge Coupled Device
CCR	Configuration Change Request
CCSDS	Consultative Committee for Space Data & Systems
CCT	Close Circuit Television
CDR	Critical Design Review
CG	Center of Gravity
CGS	Combined Ground System
CIRS	Composite Infrared Spectrometer
CLA	Coupled Loads Analysis
CLK	Clock
CMB	Cosmic Microwave Background
CMD	Command
CM	Configuration Management
CMS	Command Management System
CNT	Count
COBE	Cosmic Background Explorer
COI	Composite Optics, Inc.
COP-1	Command Operations Procedure #1
COTS	Commercial Off-the-Shelf
CPT	Comprehensive Performance Test
CPV	Common Pressure Vessel
CQ	Command Quaternion Target
CQT	Command Quaternion Table
CRC	Cyclic Redundancy Check
CSLP	Cooperative Satellite Learning Project
CSS	Coarse Sun Sensor
CT1	Cold Test #1 (of CVC Test)
CT2	Cold Test #2 (of CVC Test)
CTE	Coefficient of Thermal Expansion
CTT	Compatibility Test Trailer
CUC	CCSDC Unsegmented Time Code
CVC	Cold-Vibe-Cold
CVCDU	Coded Virtual Channel Data Unit
CVCM	Collected Volatile Condensable Material
CVT	Current Value Table
CY	Calendar Year
D/A	Digital to Analog
D/NAR	Design/Non-Advocate Review
DA	Differencing Assembly
DAC	Digital/Analog Converter
DADRA	Diffraction Analysis of a Dual Reflector Antenna
dB	[decibel]
dBi	[decibel relative to an isotropic distribution]
DBS	DBS Microwave, Inc.
dBw	[decibel relative to one watt]
DC	Direct Current
DDD	DSN Data Delivery
DDTE	Design, Development, Test, and Evaluation
DEU	Digital Electronics Unit

DHDS	Digital History Data Storage
DMR	Differential Microwave Radiometer
	Detailed Mission Requirements
DoD	Depth of Discharge
DSCC	Deep Space Communications Complex
DSOC	DSN Space Operations Center
DSN	Deep Space Network
DSPT	Data Systems Product Team
DSSE	Digital Sun Sensor Electronics
DSS	Digital Sun Sensor
DFT-21	Development and Test Facility - 21
DTO	Detailed Test Objective
EDAC	Error Detection and Correction
EEE	Electrical, Electronics and Electromechanical
EEPROM	Electrically Erasable Programmable Read Only Memory
EIRP	Equivalent Isotropically Radiated Power
EMC	Electromagnetic Compatibility
EMI	Electromagnetic Interference
EOL	End Of Life
EOM	End of Mission
EO	Engineering Order
EO-1	Earth Observer-1
EOP	End of Pass
EOT	End of Track
EPT	Electrical Product Team
EPV	Extended Precision Vector
ESD	Electrostatic Discharge
ESN	Essential Services Node
ER	Established Reliability
ETF	Environmental Test Facility
ETR	Eastern Test Range
ET	Established Time
ETU	Engineering Test Unit
EU	Engineering Unit
EVD	Engine Valve Driver
FAM	Flight Assurance Manager
FAR	Federal Acquisition Regulations
FAST	Fast Auroral Snapshot Explorer
FDC	Fault Detection and Correction
FDF	Flight Dynamics Facility
FEDS	Front-End Data System
FEM	Finite Element Model
FET	Field Effect Transistor
FIRS	Far Infrared Survey
FlatSat	*WMAP* Spacecraft Simulator Facility (GSFC)
FMEA	Failure Modes and Effects Analysis
FORTRAN	FORmula TRANslation
FOT	Flight Operations Team
FPA	Focal Plane Assembly
FSDF	Flight Software Development Facility
FSW	Flight Software
FSWM	Flight Software Maintenance Team

FRR	Flight Readiness Review
FTP	File Transfer Protocol
FWHM	Full Width at Half Maximum
FY	Fiscal Year
G&A	General & Administrative
G/O	Gain Offset
GaAs	Gallium Arsenide
GAC	Gamma-Alumina Cylinder
Gbit	[gigabit]
GCI	Geocentric Inertial
GEMAC	GSFC ElectroMagnetic Anechoic Chamber
GEO	Geosynchronous Earth Orbit
GHe	Gaseous Helium
GHz	[gigahertz]
GMT	Greenwich Mean Time
GN	Ground Network
GN2	Gaseous Nitrogen
GND	Ground
GOS	Geomagnetic Observing System
GSE	Ground Support Equipment
GSFC	Goddard Space Flight Center
GTDS	Goddard Trajectory Determination System
GUI	Generic User Interface
H&S	Health and Safety
H/W	Hardware
HDF	Hierarchical Data Format
HEALPix	Hierarchical Equal Area isoLatitude Pixelisation
HEMT	High Electron Mobility Transistor
HFSS	High Frequency Structure Simulator
Hg	Mercury
HiFi	High Fidelity Simulation
HK	Housekeeping
HPBW	Half Power Beam Width
hr	[hour]
HVAC	Heating, Ventilating and Air Conditioning
Hz	[hertz]
I&T	Integration & Test
I&V	Integration & Verification
I/F	Interface
I/O	Input/Output
IC	Integrated Circuit
ICD	Interface Control Document
IDEAS	Information Development and Applications, Inc.
ID	Identification
IDL	Interactive Data Language
IDR	Instrument Design Review
IGSE	Instrument Ground Support Equipment
IHK	Instrument Housekeeping
IITA	Information Infrastructure Technology and Applications
IMAGE	Imager for Magnetopause-to-Aurora Global Exploration
IMAPS	Interstellar Medium Absorption Profile Spectrograph
in^3	[cubic inch]

in	[inch]
InP	Indium Phosphide
IOC	Initial Operational Capability
	Initial Orbiting Configuration
	In-Orbit Checkout
IPM	Instrument Project Manager
IP	Internet Protocol
IR	InfraRed
IRU	IVA Replacement Unit
	Inertial Reference Unit
ISE	Instrument Systems Engineer
Isp	Specific Impulse [s]
ITO	Indium-Tin-Oxide
IUE	International Ultraviolet Explorer
JPL	Jet Propulsion Laboratory
JURAP	Joint User Resource Allocation Panel (DSN)
kbps	[kilobits per second]
kg	[kilogram]
kHz	[kilohertz]
K	[kelvin]
KF	Kalman Filter
km	[kilometer]
KSC	Kennedy Space Center
kw	[kilowatt]
L&IOC	Launch & In-Orbit Checkout
L1	First Sun-Earth Libration (Lagrange) Point
L2	Second Sun-Earth Libration (Lagrange) Point
LAN	Local Area Network
lbf	[pounds, force]
lbm	[pounds, mass]
LED	Light-Emitting Diode
LEE	Lightweight Electronics Enclosure
LEISA	Linear Etalon Imaging Spectrometer Array
LEO	Low Earth Orbit
LET	Linear Energy Transfer
LF	Launch Facility
LHe	Liquid Helium
LLV	Lockheed Launch Vehicle
LMAC	Little MIDEX Attitude Control Electronics
LOS	Loss of Signal
	Line of Sight
LN2	Liquid Nitrogen
LOX	Liquid Oxygen
LRR	Launch Readiness Review
LVPC	Low Voltage Power Controller
LV	Launch Vehicle
m	[meter]
M_PDU	Multiplexing Protocol Data Unit
MAC	Maximum Allowable Concentration
	MIDEX Attitude Control (Electronics)
MATLAB®	Matrix Laboratory
MAP	Microwave Anisotropy Probe

MAR	MIDEX Assurance Requirements
MAX	Microwave Anisotropy Experiment
Mbps	[megabits per second]
MCC	Mid-Course Correction
MCM	Multi Chip Module
MDM	Multiplexer/Demultiplexer
Mdot	Mass Flow Rate
MECO	Main Engine Cut Off
MEOP	Maximum Expected Operating Pressure
MET	Mission Elapsed Time
MGA	Medium Gain Antenna
MHz	[megahertz]
MICM	Multi-variable Instrument Cost Model
MIDEX	Medium-Class Explorer
MIL-71	DSN Merritt Island Testing Facility
MILA	Merritt Island Station (GN)
MITOC	MAP Integration and Test Operations Center
MLI	Multi Layer Insulation
MMFD	Multi-Mission Flight Dynamics
MPPF	Multi-Payload Processing Facility
MO&DA	Mission Operations & Data Analysis
MOC	Mission Operations Center
MPI	Message Passing Interface
MPS	Multi-Program Support
MPT	Microwave Product Team
MRR	Mission Requirements Review
	Mission Readiness Review
MRT	Mission Readiness Test
MS	Microwave System
ms	[millisecond]
MSAM	Medium Scale Anisotropy Measurement
MSX	Mid-Course Space Experiment
MV	Mongoose 5; [megavolt]
N	[newton]
N2H4	Hydrazine
NASA	National Aeronautics and Space Administration
NASCAP	NASA Surface Charging Analysis Program
NAVGSE	Navigational Ground Support Equipment
Nch	Number of Channels
ND	Network Director
NHB	NASA Handbook
NISN	NASA Integrated Services Network
Nms	Newton Meter Seconds
NOCC	Network Operations Control Center (DSN)
NRAO	National Radio Astronomy Observatory
NRZ-L	Non-Return to Zero-Level
NSF	National Science Foundation
NSPAR	Non-Standard Parts Approval Request
NSSDC	National Space Science Data Center
OC	Operations Center
OD	Orbit Determination
OMEGA	Office of the MAP Experiment General Archive

OMNI	Omni-directional Antenna
OMT	Orthomode Transducer
OPM	Orbital Parameter Message
OS	Operating System
PAF	Payload Adapter Fitting
PB	Playback
Pc	Thrust Chamber Pressure
PC	Printed Circuit; Personal Computer
PCA	Proportional Counter Array
PCB	Printer Circuit Board
PCI	Programmed Composites, Inc.
PD	Proportional and Derivative
PDR	Preliminary Design Review
PDT	Product Development Team
PDU	Power Distribution Unit
PEB	Parts Evaluation Board
PER	Pre-Environmental Review
PERT	Program Evaluation and Review Technique
PFR	Problem/Failure Report
PFU	Proto-flight Unit
PHSF	Payload Hazardous Servicing Facility
PI	Principal Investigator
PIND	Particle Impact Noise Detection
pixel	picture-element
PM	Project Manager, Phase Modulation
PN	Pseudo-Random Noise Coding
POC	Point of Contact
POP	Program Operating Plan
PROM	Programmable Read Only Memory
PR	Problem Report
PRT	Platinum Resistance Thermometer
PSE	Power Supply Electronics
psia	[pounds per square inch, absolute]
psig	[pounds per square inch, gauge]
PSK	Phase Shift Keying
PSLA	Project Service Level Agreement
PSR	Pre-Ship Review
PS	Phase Switch
PTF	Pressure Transducer and Filter
	Portable Telemetry Formatter
PU	Princeton University
PWM	Pulse Width Modulator
PWS	Primary Work Station
QA	Quality Assurance
QTM	Qualification Test Model
R/D	Reed-Solomon
RAAN	Right Ascension of the Ascending Node
RAM	Random Access Memory
RAO	Resources Analysis Office
RCS	Reaction Control System
RCVR	Receiver
RDL	Record Definition Language

RE	Earth Radius
REU	Reflector Evaluation Unit
RF	Radio Frequency
RFI	Radio Frequency Interference
RFP	Request for Proposal
RFSOC	Radio Frequency Simulations Operations Center
RID	Review Item Discrepancy
RISC	Reduced Instruction Set Computing
RM	Resources Manager
RMS	Root Mean Square
ROM	Read Only Memory
REV	Revolutions
ROSAT	Roentgen Satellite
rpm	[revolutions per minute]
RR	Requirements Review
RSI	Research Systems, Inc.
RSN	Remote Services Node
RS	Solar Radii
	Radiated Susceptibility
RSS	Root-Sum-Square
RTS	Relative Time Sequence
	Range Tracking Station
RT	Real Time
RWE	Reaction Wheel Electronics
RW	Reaction Wheel
RWA	Reaction Wheel Assembly
RXB	Receiver Box
s	[second]
S&MA	Safety & Mission Assurance
S/C	Spacecraft
SA	Solar Array
SAA	South Atlantic Anomaly
SADEB	Solar Array Deployment Electronics Box
SAEF-2	Spacecraft Assembly and Encapsulation Facility #2
SAM	Solar Array Module
SAMPEX	Solar Anomalous and Magnetospheric Particle Explorer
SAS	Solar Array Simulator
SCAPE	Self Contained Atmospheric Personnel Ensemble
SCC	Standard Cubic Centimeter
SCOPR	Systems Concept & Operating Plan Review
SCR	Spacecraft Concepts Review
	System Concept Review
SCT	Spacecraft Controller Team
SDSS	Sloan Digital Sky Survey
SDT	Spacecraft Development Team
SECO	Second-Stage Engine Cutoff
SEE	Single Event Effect
SEIT	Systems Engineering & Integration Team
SERS	Spacecraft Emergency Response System
SERTS	Solar Extreme-UV Rocket Telescope Spectrograph
SEU	Single Event Upset
SFDU	Standard Formatted Data Unit

SGI	Silicon Graphics, Inc.
SGSE	Spacecraft GSE
SH	Safe Hold
SHOOT	Superfluid Helium On-Orbit Transfer
SICM	Scientific Instrument Cost Model
SiO	Silicon Oxide
SK	Station Keeping
SLC	Space Launch Complex
SMEX	Small Explorer Program
SMM	Solar Maximum Mission
SMOC	Science and Mission Operations Center
SN	Space Network
SOH	State of Health
SOHO	Solar and Heliospheric Observatory
SPS	Small Purchase System
SPSS	Science Planning and Scheduling System
SRM	Solid Rocket Motor
SSR	Solid State Recorder
SS	Subsystem; Steady States; Stainless Steel
SSTI	Small Spacecraft Technology Initiative
STK	Satellite Tool Kit
STM	Structural/Thermal Model
STOL	Spacecraft Test and Operations Language
STOP	Structural/Thermal Optical
STPT	Structural/Thermal Product Team
STScI	Space Telescope Science Institute
ST	Star Tracker
SWAS	Submillimeter Wave Astronomy Satellite
SWG	Science Working Group
TARA	Two Axis Rate Assembly
TBD	To Be Determined
TBR	To Be Resolved; To Be Required; To Be Refined
TBS	To Be Specified; To Be Supplied
TCP/IP	Transmission Control Protocol/Internet Protocol
TCS	Thermal Control System
TDI	Time Delay Integration
TDRS	Tracking and Data Relay Satellite
TEC	Thermo-Electric Cooler
Ti	Titanium
TID	Total Ionizing Dose
TIF	Timing & Interference
TLM	Telemetry
TML	Total Mass Loss
TOD	Time of Day; True of Date
TOMS-EP	Total Ozone Mapping Spectrometer-Earth Probe
TOTS	Transportable Orbital Tracking Station
TOT	Table of Tables
Transistor	TRANsfer-reSISTOR
TRMM	Tropical Rainfall Measuring Mission
TRS	Thermal Reflector System
TSM	Telemetry and Statistics Monitor
Tsys	System Noise Temperature

TTI	Transfer Trajectory Insertion
TURFTS	TDRS User RF Test Set
UBC	University of British Columbia
UCLA	University of California Los Angeles
UPR	User Problem Report
UTMC	United Technologies Microprocessor Chip
V	Velocity; [volt]
V/F	Voltage-to-Frequency
V/T	Voltage/Temperature
	Voltage/Taper
VC	Virtual Channel
VCDU	Virtual Channel Data Unit
VDA	Vapor-Deposited Aluminum
VDC	[volt, direct current]
VDS	Voice Distribution System
VLSI	Very Large Scale Integration
VPF	Vertical Processing Facility
VRAIL	Voltage Regulator and In-Rush Limiter
VR	Virtual Recorder
W	[watt]
WBS	Work Breakdown Structure
WIND	Solar Wind Mission
WMAP	Wilkinson Microwave Anisotropy Probe
WSC	White Sands Complex
WS	Workstation
WTR	Western Test Range
XCAL	External Calibrator
XDS	XRS Detector System
XPDR	Transponder
XRSN	Transponder RSN
XRS	X-ray Spectrometer
XTE	X-ray Timing Explorer
YRS	[year]
ΔH	Change in Angular Momentum [Nms]
ΔV	Delta-V, Change in Velocity [m/s]
Ω	[ohm]